1-31-2013

# Spectroscopic exploration of conformal heterogeneity in an amorphous polyphenylene-vinylene derivative

Adam Wise

## Recommended Citation

Wise, Adam. "Spectroscopic exploration of conformal heterogeneity in an amorphous polyphenylene-vinylene derivative." (2013). https://digitalrepository.unm.edu/nsms_etds/4

Adam Wise

*Candidate*

Department of Nanoscience & Microsystems

*Department*

This dissertation is approved, and it is acceptable in quality and form for publication:

*Approved by the Dissertation Committee:*

Dr. John Grey , Chairperson

Dr. David Dunlap

Dr. Kevin Malloy

Dr. Yang Qin

# SPECTROSCOPIC EXPLORATION OF CONFORMATIONAL HETEROGENEITY IN AN AMORPHOUS POLYPHENYLENE-VINYLENE DERIVATIVE

**by**

**ADAM WISE**

B.S., Physics, Rensselaer Polytechnic Instute, 2007

DISSERTATION

Submitted in Partial Fulfillment of the
Requirements for the Degree of

**Doctor of Philosophy**
**Nanoscience & Microsystems**

The University of New Mexico
Albuquerque, New Mexico

**December, 2012**

# ACKNOWLEDGEMENTS

First, I want to thank my advisor Dr. John Grey for his support and guidance during these last five years. My education didn’t truly begin until I came to this lab, and I am indebted for what he has taught me. I will miss the stimulating discussion, and hope to be able to live up to the high standards he has set for himself and his students.

My thanks also go to Yongqian Gao, who built the lab over many late nights, endlessly good-humored and thoughtful. Tom Martin, the wunderkind perennial intern who suffered in the basement lab with me as valiantly as any grad student. Eric Martin, Tray Niles, and Alan Thomas the newest graduate students; I will miss the stimulating conversation of Friday Journal Club. And of course Jian Gao, valued labmate and friend. It has also been a pleasure to work with our interns, principally: Gavin Novotny, Jon Rabinowitz, Mimi Precit, Kori Vandergeest, Jeff Parrish, and Tassie Anderson. I will follow all their careers with interest, and hope to see them often.

I would also like to acknowledge my committee: Dr. Yang Qin, Dr. Kevin Malloy, and Dr. Dave Dunlap, who took time out of their busy schedules and have always been available for my dumb questions and selfish demands.

Last, but not least, I would like to thank Heather Armstrong for her advice, advocacy and emotional support; without her I would have hit the wall long ago.

# SPECTROSCOPIC EXPLORATION OF CONFORMATIONAL HETEROGENEITY IN AN AMORPHOUS POLYPHENYLENE-VINYLENE DERIVATIVE

**BY**

**Adam Wise**

**B.S, APPLIED PHYSICS**

**RENSSELAER POLYTECHNIC INSTITUTE, 2007**

**PHD, NANOSCIENCE & MICROSYSTEMS**

**UNIVERSITY OF NEW MEXICO, 2012**

## ABSTRACT

Photoluminescence and Resonant Raman spectroscopy were performed on the conjugated polymer MDMO-PPV (Poly[2-methoxy-5-(3′,7′-dimethyloctyloxy)-1,4-

phenylenevinylene]), both in its pure form and in blends with electron acceptors, in order to understand how conformations are affected by interactions with neighboring polymer chains and small molecules. Thermal and solvent annealing are used to tune these interactions, and the resulting changes in the electronic structure and processes of the polymer are inferred through interpretation of spectroscopic signatures.

Optical absorption and emission spectra were measured for MDMO-PPV in several solvents, in thin films processed under various conditions, and in nanoparticle form. These different environments and processing conditions can encourage the polymer to coil (bad solvent), extend (good solvent), strongly interact with neighboring molecules (nanoparticles), or interact weakly (dilute solution), and feature the polymer in a more glassy (spin-cast) or more ordered (thermally annealed) state. We can then interrogate a defined conformation of the polymer, and correlate the spectroscopic and structural changes. Analysis of the lineshape parameters of emission and absorption spectra reveal a relationship between the intensity and spacing of vibronic sidebands, and planarity of the conjugated backbone. Planarity is extremely important in conjugated polymers, as it defines the extent of electron delocalization and has serious consequences on every electronic process in the polymer. As well, solvatochromic shifts in the emission spectrum reveal information about the relative polarities of the ground and excited states.

Resonant Raman spectroscopy was used to identify the vibrational modes coupled to electronic excitation, and mode-specific displacements were estimated by modeling the photoluminescence spectra using a time-dependent quantum mechanical simulation to reproduce experimental observations. Coupling of electronic processes to vibrational modes in organic photovoltaics both helps and hinders function. It broadens absorption and emission spectra, increasing the ability to absorb light and transport energy, but can provide a structural barrier to some electronic processes. However, here we use it to investigate changes in the planarity of a conjugated polymer. Spectra of polymer/$C_{60}$ blend films show increased displacement of a symmetry-forbidden out-of-plane vibrational mode with increasing fullerene doping, indicating a loss of planarity. We also use photoluminescence spectroscopy to confirm this, as the electronic origin of emission blue-shifts with fullerene loading which indicates decreased conjugation length and thus molecular planarity.

Ground state charge transfer complexes of MDMO-PPV and several electron acceptors were studied using linear absorption and Resonant Raman spectroscopy to better understand the nuclear rearrangements that the polymer undergoes upon loss of an electron. Any bonds displaced upon the movement of charge will make it more difficult to move and separate charge in the material, processes essential for the function of a solar cell. Thin films of blended MDMO-PPV:DDQ, MDMO-PPV:TCNQ, and MDMO-PPV:PCBM blends show several orders of Raman overtones. We use the intensity of these Resonant Raman overtones and the framework of time-dependant spectroscopic theory, to estimate vibrational-mode displacements and the reorganizational barriers to charge transfer and transport.

# TABLE OF CONTENTS

# LIST OF ABBREVIATIONS

CT - Charge Transfer

CTC - Charge Transfer Complex

DDQ - 2,3-Dichloro-5,6-dicyano-1,4-benzoquinone

DFT - Density Functional Theory

DNF - 2,7-Dinitro-9-fluorenone

$E_{00}$ – Electronic Origin

HOMO - Highest occupied molecular orbital

LUMO - Lowest unoccupied molecular orbital

MDMO-PPV - Poly[2-methoxy-5-(3′,7′-dimethyloctyloxy)-1,4-phenylenevinylene]

MEH-PPH - Poly[2-methoxy-5-(2’-ethylhexyloxy)-p-phenylenevinylene]

P3HT - Poly-3-Hexylthiophene

PBTTT - Poly-(2,5-bis(3-tetradecyllthiophen-2-yl)thieno[3,2-b]thiophene)

PCBM - Phenyl-C61-butyric acid methyl ester

PL - Photoluminescence

PPV – Poly-phenylenevinylene

TCNQ -Tetracyanoquinodimethane

TCSPSC - Time Correlated Single Photon Counting

TNF - 2,4,7-Trinitro-9-Fluorenone

UV-VIS - Ultraviolet-Visible

W/W - Weight\Weight

---

# Chapter 1.

# Introduction

---

Conjugated polymers have been recognized as a potentially important material for use as the active layer in photovoltaic cells[1,2,3] and light-emitting diodes.[4,5] However, variation in polymer packing and device morphology caused by stochastic solution processing conditions and interactions between materials can have significant effects on performance.[6,7,6c] One of the key factors influencing device performance is the coupling of vibrational and electronic degrees of freedom. Electronic processes in these materials (e.g., absorption/emission of photons, transfer\transport of charge and energy) involve significant rearrangement of nuclei due to changes in electronic structure. Large rearrangements serve as an energetic barrier, and will hinder the associated electronic process.[8,9] The identity and displacement of particular vibrational modes can be determined spectroscopically if the initial and final states are directly connected by absorption emission of a photon.

Absorption and photoluminescence can in theory reveal this information, but chemical and structural heterogeneity may prevent distinct vibronic progressions from being resolved, forcing the use of effective-frequency models.[10] Attempts have been made to avoid this loss of resolution by measuring single conjugated polymer molecules[11], and freezing materials to liquid helium temperatures.[12] However, if low-frequency vibrational modes (e.g., torsional) are displaced during these processes, low-frequency vibronic progressions will inescapably ‘blur’ these spectra.[13]

An effective-frequency vibronic progression can be made more physically relevant if it can be modelled as the coalescence of several known progressions, a phenomenon known as the “Missing Mode Effect”, or MiME. This effect as been identified in transition metal complexes[14], small molecules[15] and conjugated oligomers[13]. However, the first report of the MiME in a conjugated polymer[16] is discussed below. We use this model in conjunction with Raman spectroscopy to gain structural information about a conjugated polymer from poorly resolved photoluminescence spectra despite the loss of individually-resolvable vibronic progressions.

Resonant Raman spectroscopy can overcome the obstacle of poor resolution and yield information about the vibrational modes coupled to photovoltaic-relevant electronic processes in these materials. Raman scattering is an intrinsically fast process, and avoids the relaxation inherent in photoluminescence.[17] Resonant Raman scattering yields vibrational-mode specific nuclear displacements due to specific electronic transitions[18], and allows selective interrogation of different components of a complex chemical blend by tuning of excitation energy. We use a time-dependent model of resonant Raman scattering developed by Heller[19], Tannor[20], and Zink[21], which has been used successfully for several decades to investigate similar phenomenon in related systems. This time-dependent model avoids the computational complexity of traditional sum-over-states approaches to Raman scattering, and reduces (through the judicious use of approximations, discussed below) a daunting problem to one that can be approached intuitively, and with relatively simple mathematical methods.

Furthermore, Raman spectroscopy can be used to characterize the conformation of the materials within an organic photovoltaic blend, by investigating changes in electron-phonon coupling as a result of altered processing and doping. Relaxation of selection rules for Raman activity can be used to monitor symmetry[22], reflecting changes in molecular planarity. Molecular planarity in conjugated polymers is extremely important, as it affects conjugation length and the mobility of charge carriers.[23] Below, we extend a model explored previously[24] to quantify disordering of the conjugated polymer MDMO-PPV upon addition of the electron acceptor PCBM by tracking the frequency and displacement of a symmetry-forbidden Raman-active vibrational mode.[25]

In addition to yielding information about excited-state structure, Raman scattering on resonance with a charge-transfer absorption band can reveal the vibrational modes coupled to the injection of charge onto the molecules in the complex.[9,26] Previous investigation of polymer/small-molecule charge transfer complexes have shown that the introduction of electron acceptors can planarize the polymer[24], reduce recombination of charge carriers[27], and improve overall photovoltaic performance.[28]

Below, we explore the interaction of MDMO-PPV and several small-molecule electron acceptors, and use the appearance of resonant Raman overtones to estimate the displacement of vibrational modes coupled to charge injection onto the polymer backbone[18], using a proven approach already proven in metal complexes[29]. Investigation of the extent and identity of vibrational modes displaced upon charge transfer has important consequences on charge transport and separation within solar cells[30], and has been simulated extensively[31] as a substitute for direct experimental measurements. PCBM (a chemically modified fullerene, discussed below) is the most common electron acceptor used in bulk-heterojunction solar cells, and does not form a strong charge transfer complex with most conjugated polymers. However, it may be possible to use other electron acceptors that do form ground state complexes as model systems for better understanding the nature of charge transfer interactions in high-efficiency solar cells.

## 1.1 Optoelectronic Materials

The vast majority of all electronic and optoelectronic devices - integrated circuits, light emitting diodes, solar cells, etc - are made from inorganic semiconductors, primarily silicon. Silicon is excellent for these applications due to its high charge mobility ($>10^3$ $cm^2\ V^{-1}s^{-1}$), widespread availability, and the ease with which it can be chemically doped. However, not all of the properties of inorganic semiconductors are desirable. They are extremely energy-intensive to refine into a usable form, and once refined they are expensive to process into devices - especially if deposition of thin films is required. Finally, they are limited by their mechanical properties to flat and inflexible structures.

## 1.2 Organic Solar Cell Materials

There is an alternative that is lighter, cheaper, more flexible and less energy intensive: organic materials. It is estimated that the energy input to build an organic photovoltaic is one quarter of its inorganic equivalent[32]. In the same way that polymers have displaced metals and ceramics in many structural applications, it is thought that organic electronic materials may someday replace silicon as the dominant photovoltaic technology. The performance of the best organic solar cells (~12%) is still nowhere near that of silicon (~25%), and it is also far from the 33.7% theoretical maximum established by Shockley and Queisser[33]. The main performance-limiting factors are still unclear, although beginning to identify them requires a brief detour into the history of organic photovoltaics.

What gives these organic molecules interesting electronic properties? The key is conjugation, where neighboring carbon p-orbitals overlap to create delocalized molecular π-orbitals. π-conjugated organics can be engineered with band gaps in the visible, or chemically doped into conductivity. Organic electronic materials can be further broken down into small molecule and conjugated polymers. Small molecules generally weigh less than 800 Daltons, while conjugated polymers may go from thousands to millions of Daltons in weight. An archetypal small molecule conjugated organic is shown below.

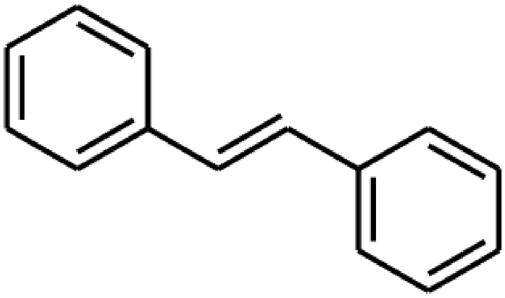

**Figure 1.2.1**: Trans-stilbene, a conjugated organic molecule used to 'whiten' laundry by fluorescing blue after absorbing ultraviolet light.

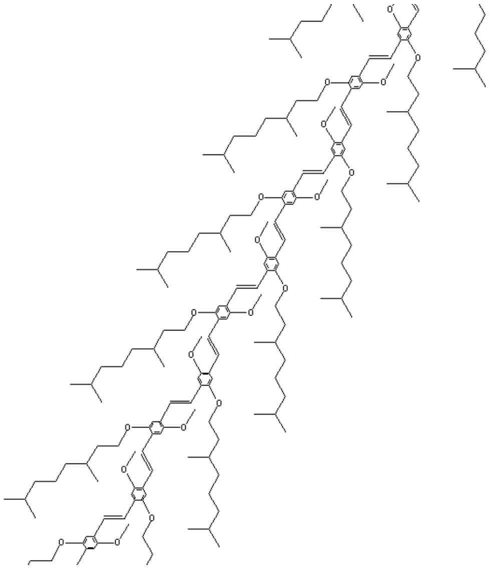

**Figure 1.2.2** A small segment of an MDMO-PPV molecule. The conjugated backbone is chemically identical to the stilbene shown above, but repeated thousands of times with the addition of solubility-enhancing alkoxy side groups. Conjugation does not extend through the entire molecule - it is disrupted by kinks, twists and chemical defects.

Thin layers of small molecules are generally made by sublimation under high vacuum, while conjugated polymers can be processed using any of the techniques developed for traditional plastics. Conjugated polymers can also be engineered with side groups that provide compatibility with any desired solvent. Once dissolved, thin films of electronically active material can be formed by spin coating, offset printing, or silk-screening on a wide variety of surfaces. Although these films appear macroscopically homogenous, depending on processing they may have many microscopic features with very different electronic properties.[6a]

This processability does come at a cost; small molecules can be grown into large crystals with few defects, whereas polymers are amorphous or semi-crystalline, which is detrimental to efficient charge transport. Also, polymerization generates a range of molecular weight products which are difficult to isolate. This chemical and structural heterogeneity leads to optoelectronic properties that can vary substantially over microscopic distances, and the lack of crystallinity and low density makes these materials virtually impossible to characterize with x-ray diffraction and electron microscopy techniques developed for inorganic crystals. Furthermore, the standard fabrication technique for the majority of organic polymer photovoltaics is to mix both the donor and acceptor materials in the same solvent, deposit them together as a film, and then allow spontaneous phase segregation to form the heterojunction. This means that the overall structure of the active layer is the result of a process which is notoriously sensitive to temperature, pressure, humidity, choice of solvent, and the nature of the surface to be coated.

## 1.3 A Short History of Solid State Organic Photovoltaics

The optoelectronic properties of organic materials have been studied since the beginning of the 20th century. The photoconductivity of anthracene was reported by Volmer in 1913[34] , and the photovoltaic effect was observed in magnesium phthalocyanines by Kearns and Calvin in 1958[35]. However, the miniscule efficiencies

(>>0.1%) of early organic photovoltaics paled in comparison to the 6% efficiency of the first silicon solar cell[36], limiting their interest due to a distinct lack of practical applications.

Early organic photovoltaics were made from a single dye sandwiched between two electrodes. The P-N heterojunction of silicon solar cells provides a Fermi level mismatch that drives electrons and holes in opposite direction towards the appropriate electrode, and defines the essential asymmetry of the device. The first organic heterojunction photovoltaic was reported in 1986 by Tang[37], which consisted of a small-molecule organic dyes bilayer. Hall[38] and Yu[39] independently reported the first conjugated polymer-based heterojunction devices in the early and mid-1990s. The history of organic photovoltaics runs parallel to that of organic light emitting diodes, as many of the materials and techniques are common to both. Light emitting diodes represent a lower-hanging technological fruit, as many of the factors that cripple organic PVs increase the efficiency of organic LEDs (e.g., recombination of charge carriers, see below) and the high color saturation inherent to organic phosphors makes them desirable compared to the wide-band electroluminescence of common inorganics.

Polymer/polymer and polymer/fullerene systems have remained the dominant system for promising high-efficiency organic photovoltaic technologies. The only current commercially available solid-state organic photovoltaic, Konarka's "Power Plastic", is based on a polymer/fullerene blend. Although the availability and variety of materials has increased, the general approach to organic solar cells has remained constant: mix a polymer and fullerene, cast them from solution onto a transparent conductive substrate, and then hope for the best. A semi-Edisonian approach has resulted in steadily-increasing performance, a better understanding of the factors that limit performance will be required to supplement the low cost of organics with an efficiency that can make them competitive with established technology. New ways of measuring elusive properties at the micro and nano-scale will be required to better understand these materials

### 1.4 Modern Photovoltaic Materials

Modern photovoltaic materials are the result of decades of effort to enhance the photovoltaic performance of the earliest semiconducting polymers. Much work has gone into the tuning the band gap of the polymer to match the sun's emission spectrum.[40,41] In general, lowering the band gap improves the collection efficiency of the cell at the cost of open circuit voltage,[33] although the use of different materials in tandem junctions[42] may surpass this one-material limitation.

Improvement of the electrical characteristics of these materials has also been an important goal. Charge carrier mobility can be increased by engineering more rigid, ladder-type polymers,[43] in-situ crosslinking[44] to increase nano-scale robustness, and slow solvent annealing[45] to encourage the growth of large crystalline domains where charge can move easily[46]. As well, harvesting excited states before vibrational relaxation to the band edge[47] (hot electron transfer) may represent a way to avoid the tradeoffs between open high circuit voltage and high photocurrent.

The use of dopants may also play an important part in the future of high efficiency (>10%) organic photovoltaics. These can be roughly divided into two categories. First, the addition of dopants like diiodooctane[48] to the solvent mixture used to cast thin films seems to improve heterojunction performance by altering solvent/solute interactions, although the dopant itself is most likely electronically inert. Other dopants, like tetracyanoquinodimethane (TNCQ) improve device efficiency by forming charge transfer complexes with the polymer component[28] and actively changing the electronic structure, potentially increases molecular planarity and reducing recombination at the donor-acceptor heterojunction.[27]

Polyphenylenevinelyenes are one class of material that have crossed over from organic light emitting diodes (OLEDs) to organic photovoltaics (OPVs). Karg[49] first investigated PPV OLEDs in the form of ITO/PPV/Al cells, and later the same structures as OPVs. Unsubstituted PPV is itself difficult to work with, at is insoluble under normal conditions, and must generally be polymerized in-situ, like oil paint. The synthesis of alkoxy substituted PPVs (shown in the previous section) in the early 1990s by Moses[50] greatly increased the interest in PPVs due to the combination of excellent electrical properties with solution processability. MEH-PPV and MDMO-PPV, both alkoxy-substituted PPVs, are representative of an entire class of materials – amorphous polymers which cannot crystallize due to the influence of waxy side groups. Structural characterization of these materials is especially difficult, as their low atomic weight and lack of crystallinity makes them unsuitable for diffraction-based techniques. Even the most crystalline forms of the more ordered polymers are difficult, although possible, to study with x-ray diffraction[51], and spectroscopic investigation of the electronic structure is an important complement.[52]

.

## 1.5 Photophysics of Organic Solar Cells

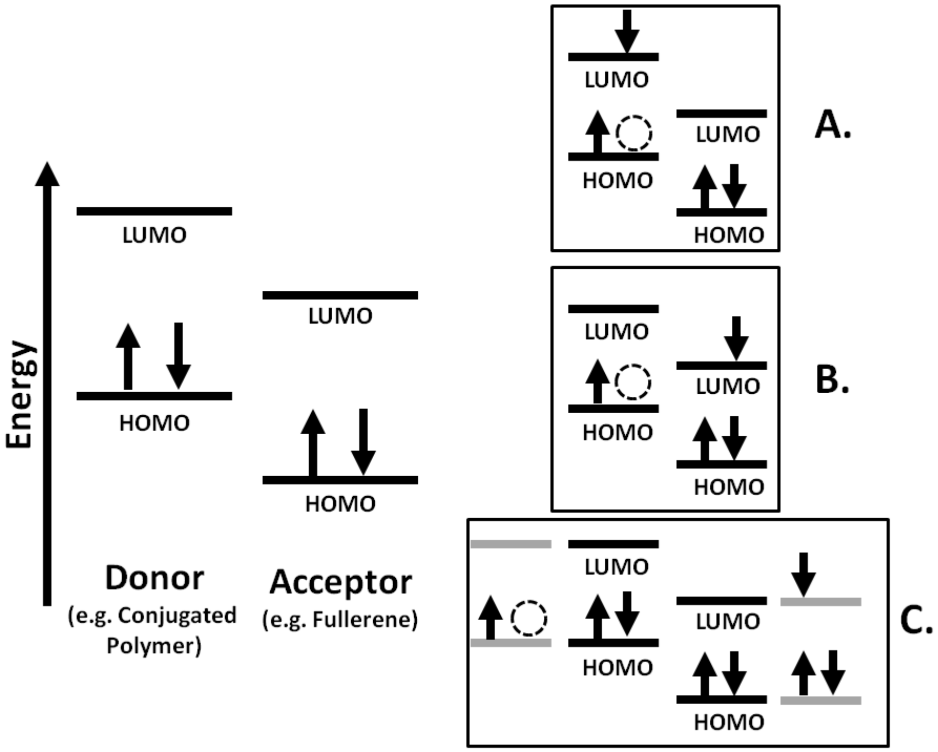

**Figure 1.5.1** Schematic of the energy levels at an organic photovoltaic heterojunction, and the processes associated with the generation of charge carriers. A) Absorption of a photon to create an excited electron/hole pair on the donor. B) Transfer of the excited electron to the acceptor, forming a charge transfer state. C) Transfer of the electron and hole to neighbouring donor and acceptor molecules.

A simplified schematic of a type-II organic semiconductor heterojunction is shown above. Absorption of a photon in the donor material excites an electron from the donor

HOMO into the donor LUMO. From the donor LUMO, the electron can transfer into the acceptor LUMO, which is at a slightly lower energy in order to drive the electron transfer. This leaves a hole in the donor HOMO, and an electron in the acceptor LUMO. These charge carriers can then hop from molecule to molecule towards the electrodes. A more detailed schematic is shown below, highlighting several potential bottlenecks in the extraction of useful charges.

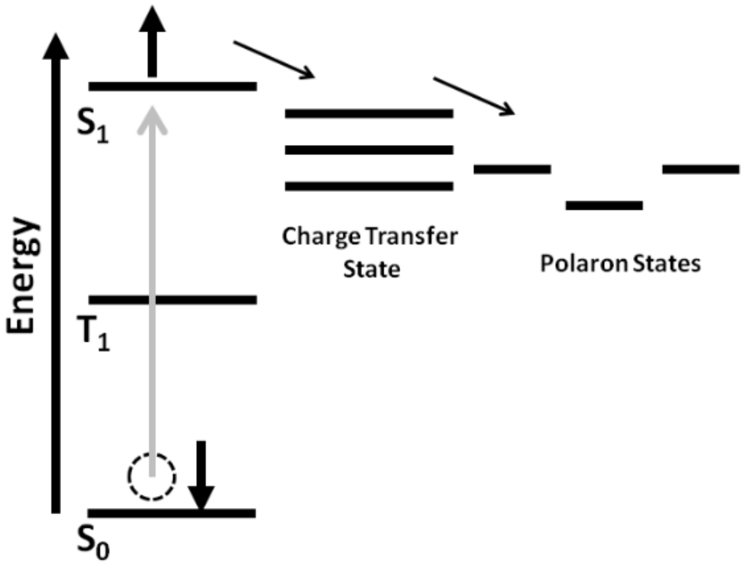

**Figure 1.5.2** A less-simplified schematic of photophysical processes in donor/acceptor solar cells.

Again, the process begins with the absorption of a photon, represented by the arrow connecting $S_0$, the singlet electronic ground state with $S_1$, the singlet electronic excited state. In organic materials, low dielectric constants and lack of a highly-delocalized band structure results in an excited electron that is strongly bound (relative to thermal energy at room temperature) to the hole it leaves behind. This bound electron/hole pair must migrate to a donor/acceptor interface in order to dissociate, and it must do so quickly or it will decay to the ground state, either by emission of light or heat. The bound electron/hole pair is referred to as an exciton, following the convention of naming a particle or quasi-particle by adding the '–on' suffix to another word, e.g. electron, photon, soliton, etc. As the excited state is thought to move from molecule to molecule, and cannot under normal circumstances diffuse or split, it is sometimes helpful to think about it as a particle.

At the donor/acceptor interface, the excited electron can transfer to the acceptor, forming a charge transfer (CT) state. The charge transfer states are drawn as a broad manifold due to vibrational interactions and variable donor/acceptor orientations. Quantifying the density of charge transfer states, essential to understanding electron transfer rates, is extremely difficult. The CT state may then dissociate into a charge separated state if the hole and electron can be moved away from the interface via self-exchange. Self exchange refers to seemingly trivial reactions like $D^*+D= D+D^*$, and $D^++D= D+D^+$, where a charge or excited state is passed between two equivalent molecules. Through this process, a charge or excited state can move down a chain of molecules like a wave through water, travelling while the medium remains overall stationary.

It is also possible for a photon absorbed in the acceptor to create an exciton, which can migrate to the heterojunction and transfer a hole to the donor. For conjugated polymer/$C_{60}$ systems, the absorption of the polymer at visible wavelengths is generally much greater, making the hole back-transfer process irrelevant. Investigation of the charge transfer state is difficult, as it is generally not radiatively coupled to other states, and is therefore spectroscopically silent. However, the CT state can be indirectly probed using transient absorption spectroscopy[53], or investigated by forming ground-state charge transfer complexes (discussed further in chapter 6 of this dissertation) with stronger electron acceptors.

The CS state corresponds to charge carriers that can be extracted at the electrodes. However, the charge transfer state can also lead wastefully back to the ground state, or to a triplet state ($T_1$) on the donor. Once a charge-separated state is achieved, the charge carriers travel by hopping from molecule to molecule, as weak intermolecular forces prevent the delocalized band-type charge transport found in inorganic crystalline semiconductors. The CS states are drawn as a staggered set of steps because in amorphous (or otherwise disordered) materials such as conjugated polymer films, charge transport is impeded by a broad density of states, i.e. the many possible conformations and conjugation lengths of polymer segments are not at a single energy, but instead span a comparatively wide range. A low-energy site for a hole can 'trap' a charge, forming a barrier to further movement.

If no clear pathway to the electrode is available, the charge carriers may diffuse back to the interface and combine back into a charge transfer complex, lowering the efficiency of the solar cell. However, if a clear path to the electrodes is available, the charge carriers may be extracted. There are considerably more pitfalls and bottlenecks in the function of organic solar cells as compared to inorganic devices, where absorption of a photon produces free charge carriers directly.

### 1.6 Spectroscopy Concepts

All of the measurements described in this dissertation are spectroscopic in nature, and are restricted to wavelengths in the near-ultraviolet, visible, and near-infrared regions of the electromagnetic spectrum, i.e. roughly 350 to 850 nanometers ($h\nu \approx 3.5$ to 1.5eV). In each measurement described below, a beam of light is used as a probe, and the scattering or absorption of this probe by a sample is used to infer something about its electronic and/or physical structure.  Figure 1.4.1 depicts a simplified version of the relevant processes.

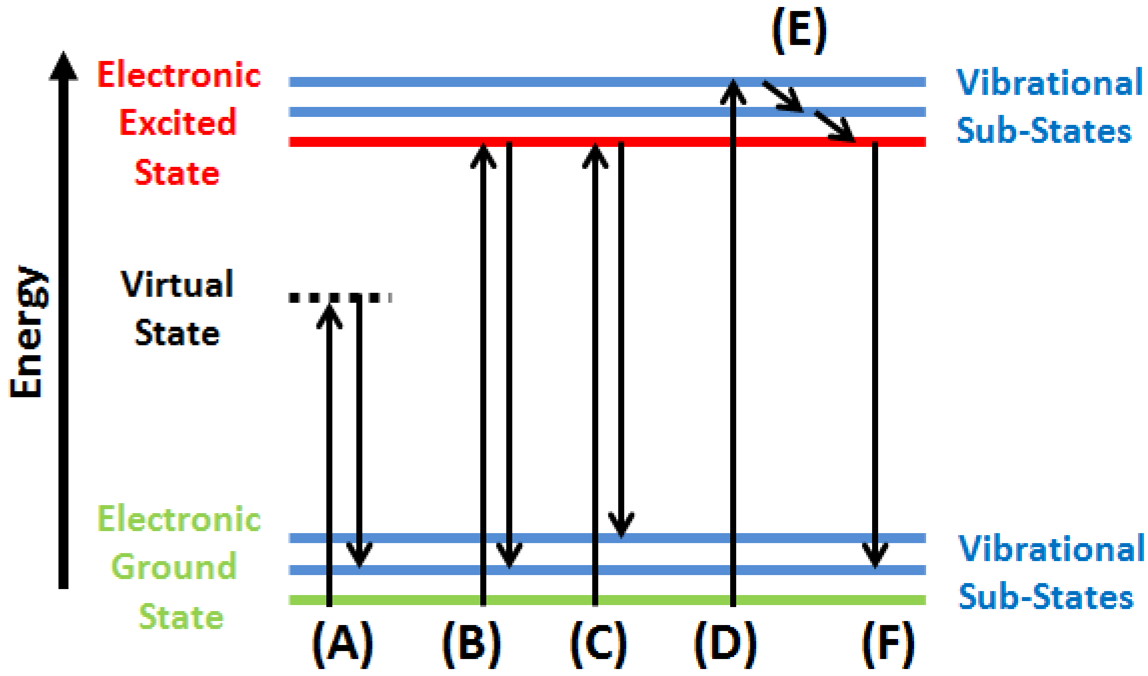

**Figure 1.6.1**:  Schematic of the different spectroscopic processes discussed in this dissertation.  A) non-resonant Raman scattering, B) resonant Raman Scattering, C) overtone resonant Raman scattering, D) electronic absorption, E) relaxation of a vibrationally ‘hot’ electronic excited state, and F) fluorescence.

Electronic absorption is, in brief, when an electron in a molecule (or ion, crystal, etc.) is promoted to a higher energy state by the absorption of a photon. This higher-energy state may also have a vibrational component if the equilibrium positions of nuclei are disturbed during the transition. As a result, in materials with strong coupling between vibrational and electronic degrees of freedom, the absorption spectrum will consist of several bands corresponding to transitions from the ground state to vibrational sub-states of the electronic excited state. In general all of the observed absorption bands will correspond to a transition originating from the ground vibrational state if the frequency of the vibrational mode is large (i.e., >500cm$^{-1}$). As the frequency increases, the chance of populating vibrationally excited states drops exponentially according to Boltzmann statistics.

Once excited, the molecule will quickly equilibrate - a very fast process due to the relatively small energy gaps between the vibrational sub-states of the excited electronic manifold. This relaxation, marked as E in the schematic, will dissipate any absorbed energy above the optical band gap, although there is currently much interest in the ability to harness these so-called “hot” electrons[47]. After relaxation to the band edge, the excited state may decay by emission of a photon (E), or through a non-radiative thermal mechanism (not pictured).

Raman scattering (marked A,B,C) is a two-photon process, which is to say that the molecule is brought up to an excited state and then immediately back down to a vibrationally-excited ground electronic state. In short, it is the inelastic scattering of a photon by a molecule, with the loss or gain of one vibrational quanta worth of energy. As it is a near-instantaneous process, there is little time for relaxation, and rather than emit from the band edge the emission is relative to the exciting light. In resonant Raman scattering, the probability of this process is greatly enhanced by an electronic state in near-resonance with the exciting light. Finally, “overtones” in the resonant Raman spectrum may sometimes be observed, which corresponds to a change in energy of two or more vibrational quanta. Their intensities can be used to characterize the mode-specific displacement of vibrational modes[29], and their frequencies can be used to quantify departures from the assumption of a harmonic potential. Much is made of their presence in further chapters.

## 1.7 Time Dependent Theory of Spectroscopy

We use the time-dependent theory of spectroscopy developed by Heller and co-workers to simulate electronic absorption/emission[54] and resonant Raman scattering[20]. The ground and excited electronic states of a molecule are assumed to be quadratic potential energy surfaces representing a particular vibrational coordinate, offset to represent displacement of nuclei during an electronic transition (see figure below). Absorption and spontaneous emission are modeled by a projecting a Gaussian wavepacket ($\varphi$) vertically from the lowest vibrational level of the initial state to the final state. As electronic transitions are coupled to vibrational degrees of freedom in these materials, the ground and excited state potential surfaces will be offset relative to each other in the coordinate of a vibration (Q). Since the initial wave-function is not an eigenfunction of the final state potential, it will evolve according to the time-dependent Schrödinger equation.

$$i\hbar\frac{\partial\Psi}{\partial t} = \frac{-\hbar^2}{2m}\nabla^2\Psi + V\Psi \qquad (1)$$

This process of projection and propagation is shown schematically below.

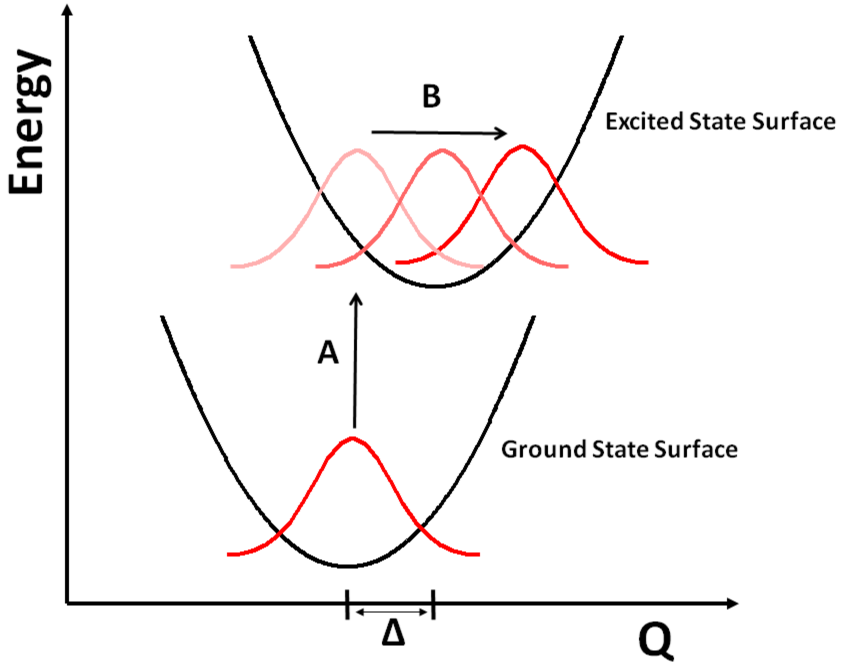

**Figure 1.7.1** Schematic describing the projection (A) of the ground-state vibrational wave function on to the excited state surface, and its subsequent propagation on the excited state surface (B).

Propagation of a wave packet on a potential surface is not a trivial calculation, but several assumptions provide dramatic simplification. If the surface is assumed to be harmonic, this will guarantee that the wave packet remains Gaussian for all times. If the propagation is only carried out for short times (e.g., a few vibrational periods), we can ignore dispersion and assume the wave packet shape remains constant. As well, if we assume that the vibrational frequencies of the ground and excited states are the same, we can reduce the complexity to the point where the propagation can be handled analytically.

### 1.7.1 Absorption and Photoluminescence

In general, emission (or absorption, which will change the $\omega^3$ prefactor below to $\omega^1$) intensity as a function of photon frequency can then be calculated using the following expression:[21]

$$I(\omega) = \omega^3 \int_{-\infty}^{\infty} e^{i\omega t} \langle \varphi | \varphi(t) \rangle dt \qquad (2)$$

where $\omega$ is the frequency of the scattered photon, $\phi$ is the initial wavepacket, and $\phi(t)$ is the time-dependant propagating wavepacket. The form of the time-dependant auto-correlation function[21], $\langle \phi | \phi(t) \rangle$, is shown below.

$$\langle \varphi | \varphi(t) \rangle = \exp\left\{ -\sum_k \left[ \tfrac{1}{2} \Delta_k^2 (1 - e^{-i\omega_k t}) - \tfrac{i\omega_k t}{2} \right] - \tfrac{iE_{00}t}{\hbar} - \Gamma^2 t^2 \right\} \qquad (3)$$

$\Delta_k$ is the dimensionless extent of displacement (vibrational coordinate) for the kth vibrational mode, $E_{00}$ is the energy of the electronic origin, and $\Gamma$ is a damping factor that accounts for time-dependant attenuation of the propagating wavepacket. As we assume a vertical projection of the wavepacket from the ground to excited state, $\langle \phi | \phi(t) \rangle$ starts at global maximum and drops with time, although it may recur at multiples of the vibrational period of the kth mode if the damping factor is not too high. However, if the damping factor is high compared to the frequency of the vibrational mode, the wavepacket will not return to the starting region and no vibronic structure will be seen in the spectrum. If there are no recurrences in time-domain autocorrelation function, then there will be little or no intensity at the corresponding frequency in the spectrum, i.e. no vibrational sidebands.

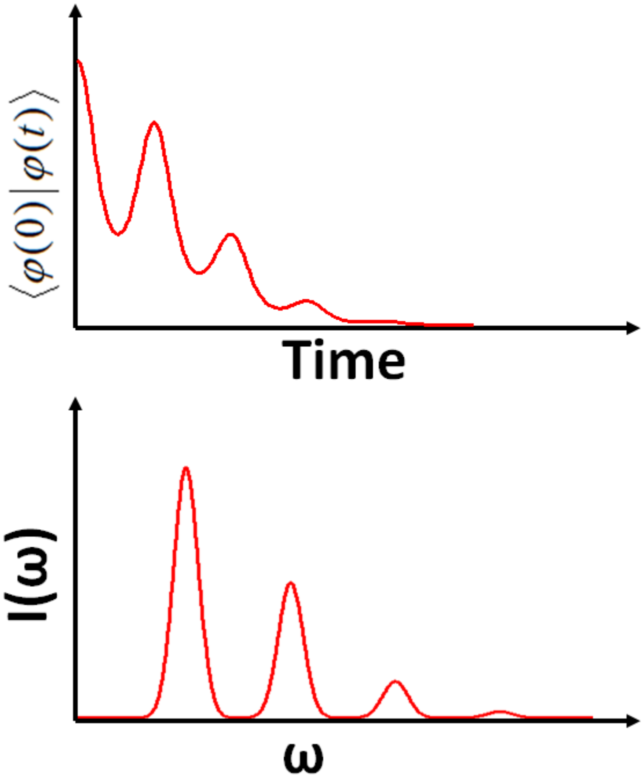

**Figure 1.7.1.1** Schematic representing the general form of the autocorrelation function (top) and its Fourier transform, the absorption spectrum (bottom). As the transition is vertical, the overlap of ϕ(0) and ϕ(t) is initially at a maximum. As the wavepacket moves away from the Franck-Condon region, the value of the autocorrelation function drops, although it rises to local maxima at the multiples of the vibrational period. Damping lowers the value of the autocorrelation at subsequent returns to the starting point.

The terms ‘Franck-Condon region’ and ‘Franck-Condon transition’ refer to the assumption that the wavepacket is projected vertically onto the new potential energy surface, and dates back to the early 20th century work of Franck[55] and Condon[56]. This assumption stems in part from the fact that nuclei have much greater masses than electrons (by a factor of ~$10^4$ for an electron compared a carbon nucleus), meaning that electrons can quickly re-organize while nuclei barely shift at all. Thus the electronic transition is assumed to occur 'vertically' between potential surfaces, without nuclear repositioning.

### 1.7.2 Resonant Raman Scattering

We can also use the time-dependent model to calculate Raman intensities, $I_{\text{i-f}}$, for each frequency, $\omega_S$, using equation 4:

$$I_{i-f} \propto \omega_I \omega_s^3 [\alpha_{fi}]^* [\alpha_{fi}] \qquad (4)$$

where

$$[\alpha_{fi}] = \frac{i}{\hbar} \int_0^\infty \langle \phi_f | \phi(t) \rangle \times \exp\{[i(\omega_k + \omega_I - E_{0-0}) - \Gamma]t\} dt \qquad (5)$$

$\Gamma$ is a damping factor, $\omega_k$ is the frequency of the $k$ th mode and $\omega_I$ is the frequency of the incident photon. The auto-correlation function, $\langle \phi | \phi(\mathrm{t}) \rangle$ can be calculated analytically under the assumptions discussed above. However, in Raman scattering the final state is an excited vibrational state. In the previous section, I have only shown a schematic for Stokes-type Raman scattering, which involves scattering with loss by the scattered photon of one vibrational quanta of energy. It is also possible to have anti-Stokes-type scattering, in which the scattered photon gains one vibrational quanta worth of energy from the material. This would require that vibrational excited states have a significant population, which is unlikely at room temperature as the vibrational frequencies are a few hundred to thousands of cm$^{-1}$, corresponding to many hundreds of degrees Celsius.

If overtones (corresponding to a change in energy of multiple vibrational quanta) and combination bands (multiple quanta from different modes) are considered, the autocorrelation function becomes:

$$\left\langle \phi_f \middle| \phi(t) \right\rangle = \prod_k \left\{ \exp\left[ -\frac{\Delta_k^2}{2}(1-\exp(-i\omega_k t)) - \frac{i\omega_k t}{2} \right] \times (1-\exp(-i\omega_k t))^{n_k} \times \frac{(-1)^{n_k}\, \Delta_k{}^{n_k}}{(2^{n_k}\, n_k)^{1/2}} \right\} \quad (6)$$

Where $\omega_k$, $n_k$ and $\Delta_k$ represent the vibrational frequency (cm$^{-1}$), order and displacement (dimensionless) of the k$^{th}$ normal coordinate. Raman overtone spectroscopy is discussed further in chapter 6.

# Chapter 2.

# Instrumentation and Experimental Technique

*Experimental details have been taken in part*

*from the publications referenced in the introductions to chapters 3,4, and 5.*

## 2.1 Confocal Microscope for Photoluminescence and Resonant Raman Spectroscopy

Photoluminescence and resonant Raman spectra were measured using a setup shown below in schematic form. Collimated light from an Argon/Krypton laser is bounced off of a dichroic mirror into the back of a microscope objective, which focuses the light onto a sample mounted on a two-dimensional translation stage. Light scattered from the sample is collected by the same objective, and passes back through the dichroic mirror into the entrance port of a CCD-equipped spectrometer. An optical low-pass filter (referred to as an ‘edge’ filter due to its sharp transmission cut-off) is used to remove residual excitation light that passes through the dichroic mirror.

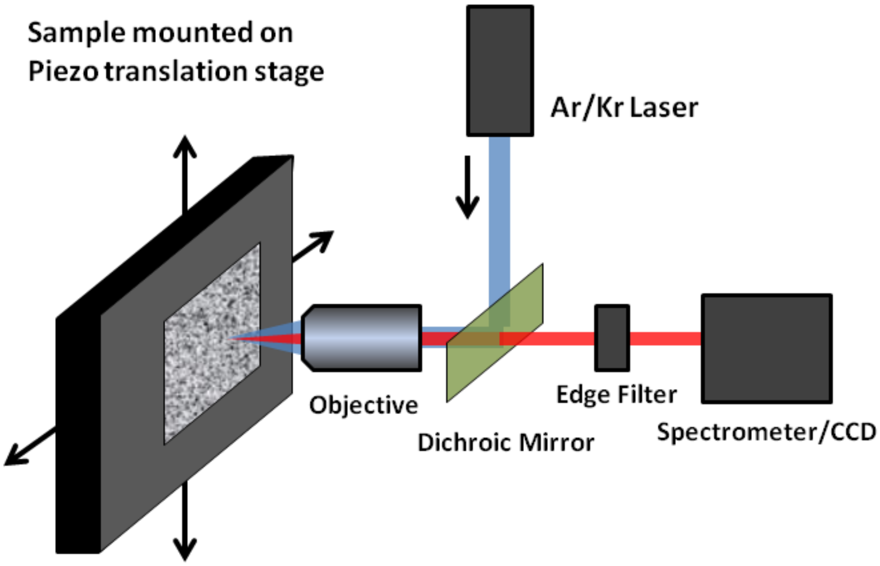

**Figure 2.1.1** Schematic of the instrument used to record photoluminescence and resonant Raman spectra of thin films.

### 2.2 Solution Fluorimetry

The instrument used for collecting solution PL spectra (Varian Eclipse) functions in a similar fashion to the instrument described in section 2.1, but the thin-film sample is replaced with a cuvette, the excitation source is a lamp rather than a laser, and the detector is a photomultiplier tube scanned with a grating rather than a CCD.

### 2.3 Time-Correlated Single Photon Counting

In the past, emission transients were recorded by taking a photograph of an oscilloscope trace of the signal from a photomultiplier tube. Fortunately, now we can record the dynamics of photoluminescence by using more genteel methods. Time-

Correlated Single Photon Counting measurements use a sensitive single-channel detector (photomultiplier tube or avalanche photodiode)  attached to a timing board that records the arrival time of individual photons relative to the reference signal from a pulsed laser. By counting tens of thousands of photon arrivals over many millions of laser pulse cycles, a histogram can be built up which is an approximation of the true PL decay transient.  The experimental geometry is similar to the microscope discussed in section 2.1, with the ion laser replaced with a pulsed diode laser, and the CCD replaced with an avalanche photodiode detector.

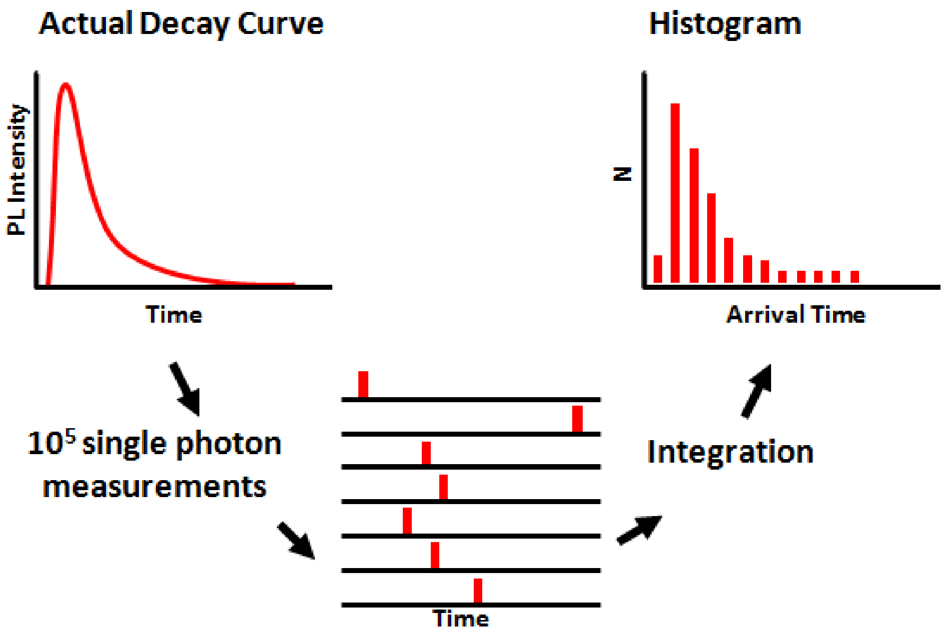

**Figure 2.3.1** The concept behind TCSPC measurements.  The actual decay transient (top) is measured indirectly by detecting the arrival time of single photons from an ultra-low brightness source (middle).  After millions of cycles of detection, a histogram of photon arrival time is built (bottom) which approximates the true signal.

The data can then be fit to an exponential decay of the form $I(t)=I_o e^{-t/\tau}$ , where I is the intensity of emission, t is time, and $\tau$ is the lifetime of the excited state. The form of this decay is a classic example of zero-order kinetics, i.e. where rates are independent of the concentration of the reactants. Excited state lifetimes and the possible presence of multiple emitting species can be thus be determined.

### 2.4 Solution Absorption and Photoluminescence Spectra

ilute solutions of MDMO-PPV in acetone, chlorobenzene, toluene, tetrahydrofuran, and chloroform were prepared under nitrogen at an initial concentration of 5mg/ml. The resulting solutions were filtered to remove residual solids, and then serially diluted to a concentration of $<10^{-6}$ M. The diluted solutions were transferred to sealed cuvettes photoluminescence, excitation, and absorbtion spectra were measured. Care was taken to avoid the formation of nanoparticles, which emit a lower wavelength than the well-dissolved polymer and boost the apparent intensity of vibronic sidebands (see the figure below).

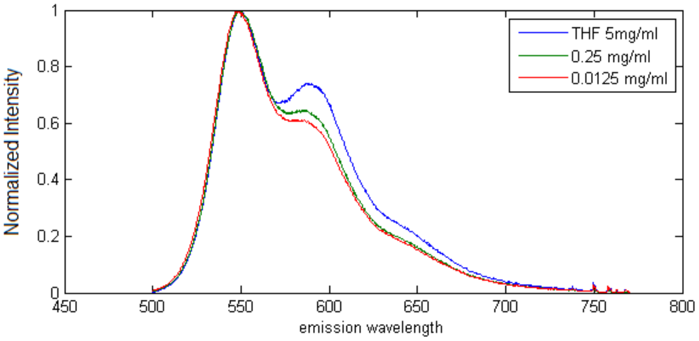

**Figure 2.4.1** Emission spectra of MDMO-PPV dissolved in THF at various concentrations. Too high of a concentration of polymer causes the formation of transient nanoparticles which emit at a lower frequency, boosting the apparent sideband intensity.

## 2.5 Thin Film and Nanoparticle Emission Spectra

MDMO-PPV and PCBM were dissolved separately in anhydrous chlorobenzene at a concentration of 5 mg/ml, and magnetically stirred in 2ml bottles overnight under dry nitrogen. The resulting solutions were filtered through 200 nm PTFE syringe filters to remove any residual solids. The MDMO-PPV and PCBM were mixed in various ratios while still in solution, and thin films were prepared by spin-casting the blended solution onto cleaned glass cover slips under dry nitrogen. Thermal annealing was performed on a hotplate at a nominal temperature of 130 °C for 0 to 300 seconds, again under a dry nitrogen atmosphere to avoid oxidation.

Nanoparticles were prepared by re-precipitation of the polymer in an incompatible solvent (water). MDMO-PPV dissolved in THF was injected into a 20ml vial of de-ionized water under sonication, and the formation of nanoparticles was confirmed by an immediate orange-to-red color change. The resulting suspension of nanoparticles was mixed with an aqueous solution of polyvinyl alcohol and spin-cast onto cleaned glass cover slips. Confocal scanning miscroscopy, using an experimental geometry as described in the previous section, was used to measure the emission spectra of individual nanoparticles. Excitation power density was approximately 100 W/cm$^2$. Photoluminescence transients were recorded to confirm that no significant change in emission intensity (indicating photobleaching) would occur over the time period needed to acquire spectra.

Resonant Raman measurements of MDMO-PPV/PCBM blend films were recorded using the instrumental geometry described above. Excitation was provided by the 568nm and 488nm lines of a Melles-Griot Argon/Krypton gas laser. Excitation power density was limited to 1KW/cm2, and all measurements were preformed with the samples in a nitrogen flow cell to limit contact with atmospheric water and oxygen. Corrections for wavelength-dependant detector response were calculated by recording the emission spectrum of a tungsten filament, and comparing to the expected black-body emission spectrum.

## 2.6 Excited State Lifetime Measurements

Photoluminescence transients of thin films were recorded using a Becker and Hickl SPC-130 Time-correlated single photon counting module. An Edinborough Instruments pulsed diode laser emitting at 445nm was used for excitation. Care was taken to ensure that the probability of a photon arrival during a single measurement period was less than $10^{-3}$, and that the measured transients were unaffected by changing measurements parameters. The instrument response function was taken to be the measured transient of the laser pulse scattered from a clean glass cover slip.

Wavelength-dependant lifetime measurements were recorded using narrow band pass filters before an id Quantique avalanche photodiode detector.  Iterative fitting of the resulting transients was performed to extract excited state lifetimes..  Matlab code for fitting and analysis is described in the appendix.

## 2.7 Preparation and Measurement of Charge Transfer Complexes

Solutions of MDMO-PPV, DNF and DDQ were dissolved in chlorobenzene and filtered through 200 nm PTFE syringe filters to remove residual solids. The solutions were then blended in 1:1 volume:volume ratios, and thin films made by spin or drop casting onto cleaned glass cover slips. The presence of charge-transfer interactions was confirmed with UV-VIS absorption spectroscopy.

Resonant Raman scattering measurements of thin films were made in a nitrogen flow cell to avoid degradation, and no significant change in the spectra were measured over the course of the experiments.  The experimental geometry is as was described earlier in this chapter.

The 488nm, 568nm, and 647nm lines of a Melles Griot Argon/Krypton laser were used for excitation, and power densities were kept at approximately 1kW/cm$^2$.  An Andor Newton thermoelectrically cooled EMCCD was used to record spectra. Cprrections for wavelength-dependant sensitivity were determined by measuring the emission spectrum of a tungsten filament, and applied where necessary.

# Chapter 3.

# Observation of the Missing Mode Effect in a Poly-Phenylenevinylene Derivative: Effect of Solvent, Chain Packing, and Composition

Reproduced with permission from

*Journal of Chemical Physics* **2010**, 133, 174901-174910

## 3.1 Introduction

Excited state structural displacements in molecular optoelectronic materials play a very important role in determining the outcomes of competing physical processes that affect the overall material performance. Of all molecular candidate systems, conjugated

---

*This article has been edited re-formatted for this dissertation, and some supplemental information has been added..

polymers have attracted the most interest as active materials for optoelectronic applications owing to their low cost and solution processability.[1, 3, 59] This versatility in processing is also complemented by the tunability of optical and electronic properties of polymers by careful choice of solvent,[60] additives[61] and molecular[62] or nanocrystal[63] dopants that induce small changes in structural properties (chain conformation, packing and morphology) in addition to facilitating charge and energy transfer.[6d, 64] Because device performance is strongly dependent on these factors, accurate descriptions of excited state potential energy landscapes are needed that also account for the effects of morphological heterogeneity that modulate displacements and ultimately material performance.

Vibronic signatures from optical spectra provide a straightforward means of quantifying excited state displacements in conjugated organic systems. Unfortunately, optical spectra of polymers measured in solution and the condensed phase at room temperature, or even at cryogenic temperatures, often lack sufficient resolution for observing vibronic progressions in all displaced modes such as low frequency bending deformations. This feature arises primarily from conformational/morphological heterogeneity intrinsic to polymers that can be circumvented by low temperature single molecule spectroscopy[11, 65] and site selective spectroscopy[66]. However, these techniques are often difficult to implement in device structures to establish relationships between ground and excited state structure and material performance. When vibronic structure is absent or weakly resolved, effective coordinate models must often be used to quantify displacements where the dominant progression frequency interval is usually treated as an ad-hoc adjustable parameter.[10, 67] This situation is common for conjugated polymer emission lineshapes and it is generally assumed that the dominant vibrational displacement is along the totally symmetric C=C stretching mode of the polymer backbone (~1400-1600 $cm^{-1}$). Realistically, multiple vibrational coordinates can be significantly displaced but their contributions are effectively masked in experimental spectra. This situation causes a coalescence and can give rise to progression intervals that do not match any vibrational mode frequency and often substantially less than C=C modes.[10, 68] This phenomenon is known as the "missing mode effect" (MIME)[69] and has been documented mostly in emission spectroscopic studies of transition metal complexes.[70] While observations of the MIME in conjugated organics are less frequent, several studies of oligomer systems showing multiple mode excited state displacements have been analyzed using both time- and frequency-dependent approaches.[13, 15, 71] Detailed studies of the MIME in polymer thin films can be more difficult due to the high sensitivity of the types and magnitudes of excited state vibrational displacements on the polymer conformation, packing and morphology. Furthermore, polymers are multi-chromophoric systems and emission generally occurs from minority trap sites that are populated chiefly by energy transfer from higher energy sites. This feature implies that fluorescence emission lineshapes only report excited state displacements from a small fraction of chromophore species and, therefore, estimates of individual mode displacements may not reflect the true structures of these emitters. On the other hand, it is possible to selectively access different emitters by controlling specific conformation and interchain interactions that governs energy funneling to emissive sites. A major goal is to characterize the excited state geometries of accessible emissive species in a prototypical conjugated polymer system using different functional forms to induce changes in interchain packing interactions and morphology.

Below, we show that multiple vibrational distortions in emission transitions of the conjugated polymer, poly[2-methoxy-5-[3',7'-dimethyloctyloxy)-1,4-phenylenevinylene] (MDMO-PPV) (Figure 4.1.1), result in a MIME progression interval that can be tuned depending on the functional form of the system.

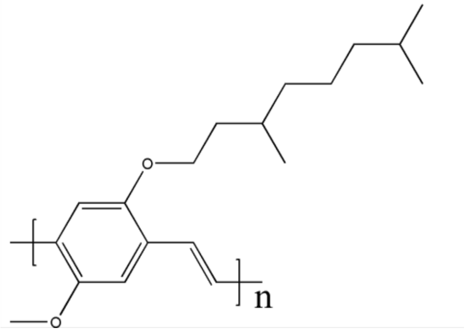

**Figure 3.1.1** Molecular structure of MDMO-PPV.

We use the time-dependent theory of spectroscopy developed by Heller and co-workers to calculate lineshapes and quantify important changes in the polymer structure that have large implications on material performance.[54, 72] Estimates of mode-specific vibrational displacements are obtained independently from pre-resonance Raman spectra that circumvents issues of poorly resolved vibronic structure as well as difficulties of traditional computational approaches. The time-dependent approach also provides an intuitive explanation for the appearance of the MIME that can be extended in more complex material forms where structural heterogeneity modifies the vibrational displacements causing variations in the observed MIME frequencies and lineshape profiles. To this end, we study different forms of MDMO-PPV to control interchain packing and conformational properties that induces minor structural changes of the polymer chains that are readily observed in the lineshape profiles and MIME frequency. For example, in dilute solutions polymer chains are well isolated which allows for detailed characterization of the role of polymer conformation on energy funneling characteristics. Structural complexity is then introduced to understand the role of chain packing on small size scales (<100 nm) using a simple repricipitation approach to assemble MDMO-PPV nanoparticles ~10 to 80 nm in diameter (~10 to 100 polymer chains). Emission spectra from nanoparticles can then be compared to those of thin films to understand the effect of the number of interchain interactions on excited state geometries.

## 3.2 Results and Discussion

### 3.2.1 The Missing Mode Effect in Emission Spectra of MDMO-PPV Dilute Solutions

In order to reliably quantify mode-specific vibrational displacements in different functional forms of MDMO-PPV a lineshape analysis procedure must be used that can accommodate multiple displaced modes and be extended to more complex material forms without requiring increased computational time. Due to the large number of states ($>10^{10}$) required in a traditional sum-over-states vibronic analysis, a time-dependent wavepacket approach is much simpler and straightforward for simulating spectra. Wu et al. used such an approach to study emission lineshapes of distyrylbenzene single crystals that involved eleven displaced modes.[15] Furthermore, since mode-specific vibrational displacements are difficult to determine from polymer emission spectra, estimates of relative displacements can be generated from pre-resonance Raman intensities using the short time approximation. We use a similar time-dependent approach as Wu et al. to quantify the MIME in different forms of MDMO-PPV that have varying degrees of interchain interactions.

In the time-dependent picture, the MIME arises when overlap recurrences from multiple displaced modes coalesce into a new recurrence time that, when Fourier transformed to generate the spectrum using equation 2, results in a MIME progression interval. The relative contribution of each mode to the MIME frequency is not a simple average but instead determined largely by the magnitude of its displacement.

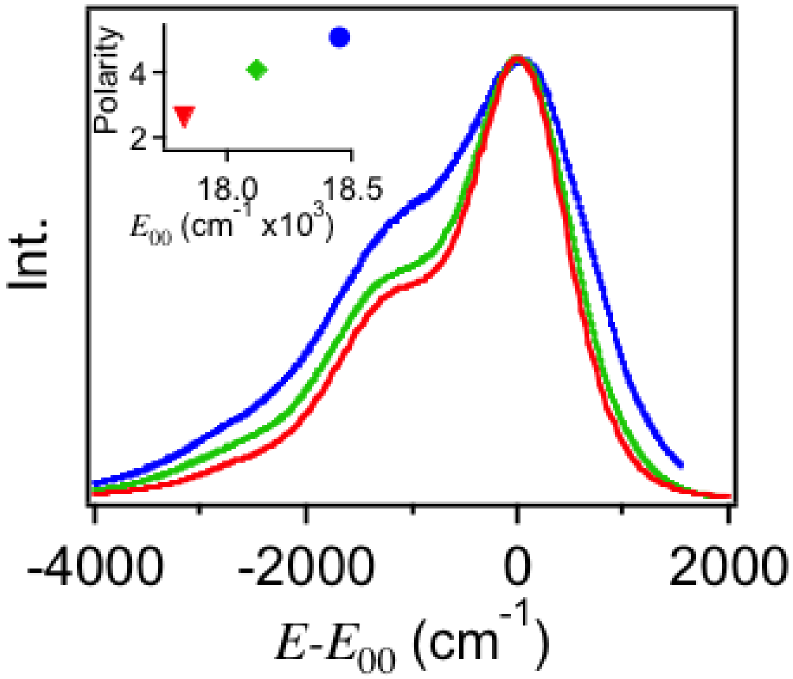

**Figure 4.2.1.1** Solution fluorescence emission spectra of MDMO-PPV in chlorobenzene (red); chloroform (green); acetone (blue). Spectra are shifted by subtracting their peak energy to compare linewidths and envelopes. Inset: solvent polarity index versus peak energy ($E_{00}$).

In order to better illustrate the effect of solvent on vibronic lineshape patterns, spectra maxima are shifted to zero energy by subtracting their peak energy ($E_{00}$). Solvatochromic effects are displayed by plotting the solvent polarity index[73] as a function of $E_{00}$ (Figure 4.2.1.1 inset). It is immediately apparent that increased solvent polarity not only results in increased peak emission energy but also vibronic linewidths and intensities of the sidebands. The negative solvatochromism indicates a polar ground state and non-polar emitting state whereas increased linewidths suggest a broader distributions of conjugation lengths.

We now focus on solution emission lineshapes showing significant differences with choice of solvent. A cursory analysis of dilute solution spectra in the above figure, using a single effective vibrational mode with an adjustable frequency yielded dominant progression intervals of 1215±7 cm$^{-1}$ (chlorobenzene), 1220±10 cm$^{-1}$ (chloroform), and 1225±15 cm$^{-1}$ (acetone) were obtained with $\Delta_{\mathrm{eff}}$ values of 1.00, 1.05, and 1.2, respectively. None of these frequency intervals, however, matched any ground state vibrational mode. This vibronic spacing is instead attributed to the MIME involving nonzero displacements of several vibrational modes in the range of 800-1600 cm$^{-1}$. A possible alternative explanation for the irregular progression frequency interval could arise from mixing of vibrational coordinates in the excited state that would also invalidate the harmonic approximation. However, comparison of experimental data and calculated lineshapes from the effective mode fits did not show significant deviations from a Poissonian envelope indicating no deviations from the idealized harmonic model.

Within the time-dependent picture, overlap recurrences from several displaced vibrational modes coalesce into the MIME recurrence. However, the contribution of each mode can be difficult to determine from both theory and experiment. This difficulty can be alleviated by obtaining estimates of the relative displacements, $\Delta_k$, for each displaced modes from pre-resonance Raman intensities, $I_k$, using the following relation from the short-time approximation.[74]

$$\frac{I_k}{I_{k'}} = \frac{\omega_k^2 \Delta_k^2}{\omega_{k'}^2 \Delta_{k'}^2} \qquad (7)$$

Where does this formula come from? As discussed in the previous section, in Raman scattering we are looking at the time-dependent overlap of a ground-state vibrational wavefunction with the first vibrationally excited wavefunction, i.e. $\langle \phi_1 | \phi_0(t) \rangle$. As these wavefunctions are orthogonal (assuming the potential is quadratic) the wave function must move away quickly to push this integral above zero and generate any Raman intensity. If we only concern ourselves with short times, the most important contribution should be from the slope of the potential in the Franck-Condon region. This slope should be proportional to displacement, and also to frequency, so the greater the displacement and frequency of the mode, the faster the wave packet moves away from its initial position and the greater the value of $\langle \phi_1 | \phi_0(t) \rangle$.

Five principle Raman bands were identified in pre-resonance dilute solution Raman spectra corresponding to polymer backbone vibrations that are included in the vibronic analysis routine: [1] out-of-plane C-H bend (vinyl) (961 cm$^{-1}$), [2] C-C stretch/C-H bend (phenyl) (1111 cm$^{-1}$), [3] C-C inter ring stretch (1280 cm$^{-1}$), [4] C=C stretch/C-H bend (vinylene) (1305 cm$^{-1}$), and [5] C=C (phenyl) symmetric stretch (1582 cm$^{-1}$). Several lower frequency modes (<700 cm$^{-1}$) were also observed, but were not included in the analysis due to low signal-to-noise or the fact that their overlap recurrences will be damped out if these frequencies are smaller than the damping factor, Γ used in the fitting procedure described below. Intensities were compared in a pairwise fashion and the table below shows the pre-resonance Raman intensity ratios along with relative displacements for modes [1-5] determined from equation 7.

**Table 3.2.1.1.** Pre-resonance Raman intensity ratios and relative emitting displacements for MDMO-PPV dilute solutions.

| | | | CB$^a$ | CF$^b$ | AC$^c$ |
|---|---|---|---|---|---|
| mode | $I_k/I_{[1]}$ | $\Delta_k/\Delta_{[1]}$ | $\Delta_{calc.}$ | $\Delta_{calc.}$ | $\Delta_{calc.}$ |
| [1] | 0.38 | 1.01 | 0.52 | 0.54 | 0.61 |
| [2] | 0.34 | 0.83 | 0.42 | 0.44 | 0.50 |
| [3] | 0.57 | 0.93 | 0.47 | 0.49 | 0.56 |
| [4] | 0.64 | 0.97 | 0.49 | 0.51 | 0.58 |

| | | | | | |
|---|---|---|---|---|---|
| [5] | 1.00 | 1.00 | 0.51 | 0.54 | 0.60 |

Values of fit parameters used in eq. 2 for $E_{00}$ (cm$^{-1}$) and Γ (cm$^{-1}$) were: [a] 17811, 335; [b] 18100, 350; [c] 18360, 385.

Overall, the relative Raman intensities changed little with solvent, pre-resonance excitation energy as well as the inclusion of fullerenes that is consistent with the observation that the emission MIME frequency did not vary appreciably with solvent. Figures 4.2.1.2a-c shows experimental dilute solution fluorescence emission spectra and fit spectra generated from the time-dependent approach with the former offset along the ordinate for clarity.

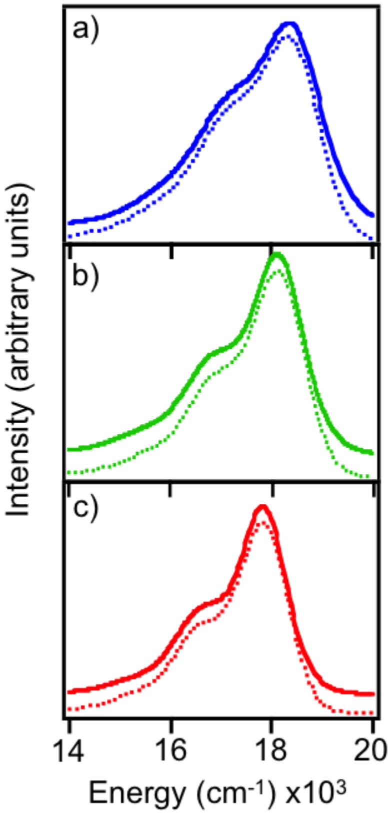

**Figure 3.2.1.2** Experimental (solid) and calculated (dotted) traces for MDMO-PPV dilute solutions; a) acetone , b) chloroform, c) chlorobenzene. The former are offset along the ordinate for clarity.

Relative emitting state displacement values from pre-resonance Raman intensities were scaled to reproduce observed vibronic intensity distributions using estimates from dilute solution excitation spectra linewidths. However, these preliminary estimates for the absolute displacements slightly overestimated intensities of sidebands for all solvents most likely due to inhomogeneous broadening effects from a distribution of absorbers. The best-fit emitting state displacements had to be decreased by ~10% to obtain good agreement with experiment and are shown in the table above. Other key fit parameters, namely $E_{00}$ and Γ, were determined solely from experimental lineshapes.

Overall, fit spectra reproduce the experimental MIME frequency very well and only minor deviations are observed near the emission onsets possibly due to scattering effects and emission from minority short chain segments. Changes in the intensity distributions and peak emission energies for different solvents noted above likely arise from chain conformation effects whereby well-solvated chains tend to be in a more elongated structure and less-solvated chains will exist in collapsed conformations.[75] In the latter, rapid energy transfer to minority low energy sites dominates and emission can occur from as little as one site per chain.[76] In addition to conformation-dependent energy funneling, the solvent polarity can also modulate inductive effects of the alkoxy side chain groups causing shifts in peak energy maxima.

By arbitrarily decreasing the linewidth parameter, Γ, to generate high resolution spectra we examine the contributions of each mode to the observed MIME interval in all dilute solution spectra. Figure 4.2.1.3a (below) shows a high resolution spectrum obtained from the chlorobenzene fit parameters that uses a small value of Γ (10 $cm^{-1}$) and larger total time and time steps to highlight the intensity distributions of individual displaced modes.

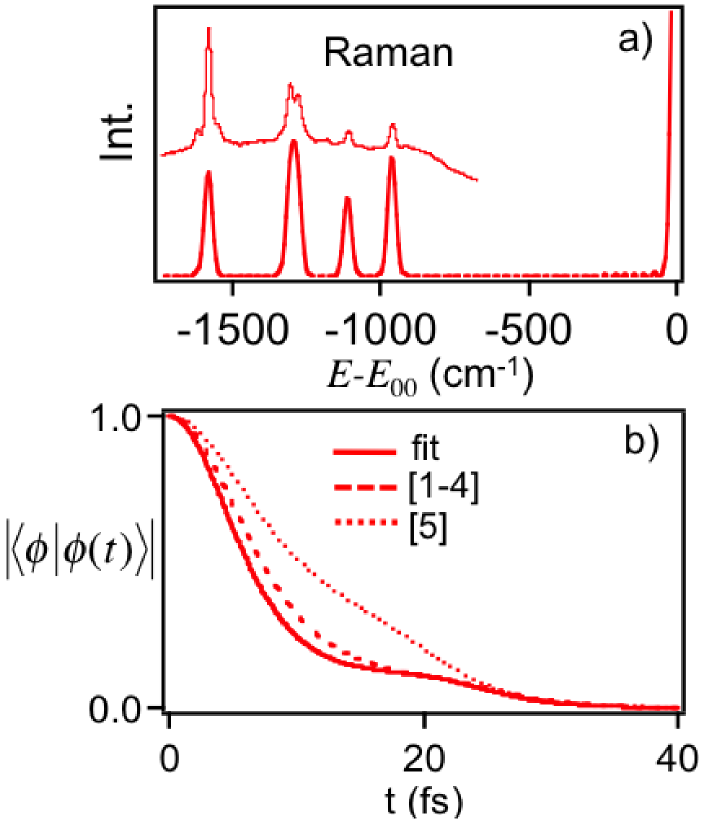

**Figure 3.2.1.3** a) High resolution fit spectrum with the peak energy shifted to zero; a representative pre-resonance Raman spectrum (offset for clarity) is included for comparison. b) Autocorrelation overlaps for a best-fit spectrum (red solid trace), modes [1-4] and mode [5] using the relative displacements estimated from pre-resonance Raman intensities.

The peak energy is shifted to zero by subtracting the $E_{00}$ and only the 0-1 region is shown. For comparison, a representative pre-resonance Raman spectrum is displayed (offset for clarity) to highlight the contributing modes. It is important to note that since the difference in frequencies of modes [4] and [3] were similar to $\Gamma$, these transitions coalesce into one peak in the fits. A small beating effect is also noted for >1-0 sidebands (not shown) but has only a minor effect on the MIME due to the overall displacements. The vibronic intensity pattern is quite similar to those of previous multi-mode analyses of related polymers[68a].

Another key advantage of the wavepacket approach is insight into time-domain aspects of the MIME. Figure 4.2.1.3b shows overlaps for the chlorobenzene fit spectrum shown in Fig. 4.2.1.2c along with overlaps fits using only mode [5] and modes [1-4] using the calculated displacements in the table above. First, the overlap from [5] shows a partial recurrence at ~18 fs whereas that of modes [1-4] have a partial recurrence at ~23 fs. Comparison with the CB best-fit overlap shows a partial recurrence at ~22 fs that is consistent with observations from previous work that the MIME frequency tends toward the largest displaced mode[70a] ([1] in this case). From these plots, it is important to note that the falloff of the overlap plays a key role in determining the MIME frequency since it directly related to the displacement. For example, a small displacement between emitting and ground state potential energy surfaces leads to a smaller falloff since the wavepacket does not move far away from the Franck-Condon region. In most circumstances, it is usually sufficient to only consider the high frequency C=C symmetric stretches in a vibronic analysis of conjugated polymer lineshapes owing to fast recurrences that survive damping effects. However, because MDMO-PPV exhibits significant displacements in lower frequency vibrations (i.e., [1-4]), these modes can exert a strong influence on the wavepacket dynamics affecting the observed MIME frequency.

Overall, the time-dependent picture provides a meaningful and intuitive approach to understand complex excited state geometries that are not otherwise possible from conventional time-independent, effective coordinate models. Because of the current interest in polymers as active materials in device applications, it is now informative to track changes in the excited state vibrational displacements through the MIME interval in condensed functional forms encountered in device environments where chain packing can significantly modulate photophysical processes preceding emission transitions.

### 3.2.2 The Missing Mode Effect (MiME) in the Condensed Phase

Polymer molecules are generally cast into thin films from solution to form active layers in various optoelectronic applications, such as solar cells. The extreme structural heterogeneity intrinsic to polymers can lead to significant changes in optical and electrical properties depending on the processing conditions used. We explore several condensed forms and composites of MDMO-PPV and use the time-dependent emission lineshape analysis procedure to determine the role of chain packing interactions as well as morphology and composition on the excited state potential energy landscape and MIME frequency.

Nanoparticles of MDMO-PPV are first used as a testbed to understand potential size-dependent properties of this system, specifically, the amounts of interchain contacts. These systems also have the advantage of enhanced photostability, unlike single molecules, primarily due to the tightly packed nature of polymer chains within the particle that reduce photodegradation even in oxygen-rich environments. Single nanoparticle emission in PVA films is identified by scanning the sample using the confocal microscope using 488 nm (20492 $cm^{-1}$) and Figure 4.2.2.1a shows a typical fluorescence emission image of dispersed nanoparticles in PVA.

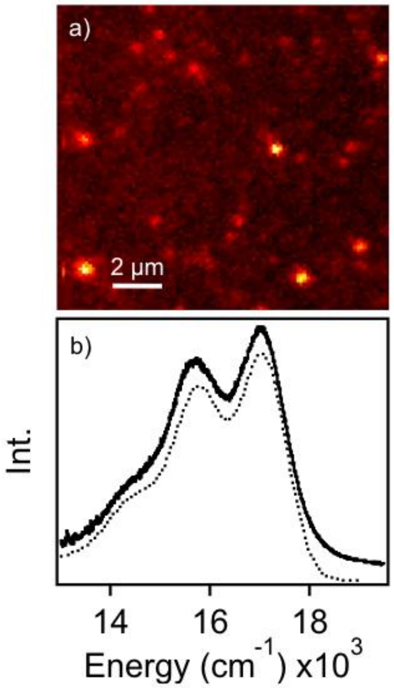

**Figure 3.2.2.1.** a) Fluorescence emission image of MDMO-PPV nanoparticles. b) Ensemble emission nanoparticle emission spectrum (solid trace) constructed by summing individual spectra. The fit spectrum (dotted trace) appears beneath the experimental spectrum.

Image linescan analyses showed that the spot sizes are diffraction-limited (~300 nm) and the number of spots increased linearly with increased concentration. Single particle emission spectra showed very little change from nanoparticle to nanoparticle which is consistent with previous findings in related polymer nanoparticles. Figure 4.2.2.1b shows an averaged single nanoparticle emission spectrum with a clearly resolved vibronic progression that was obtained by summing together single nanoparticle spectra. This ensemble spectrum also closely resembles spectra generated from dilute aqueous solution dispersions suggesting no further packing relaxation effects occur upon spin casting. Single nanoparticle spectra show a MIME interval of ~1340 cm$^{-1}$ that is noticeably higher than that of MDMO-PPV molecules in dilute solutions.

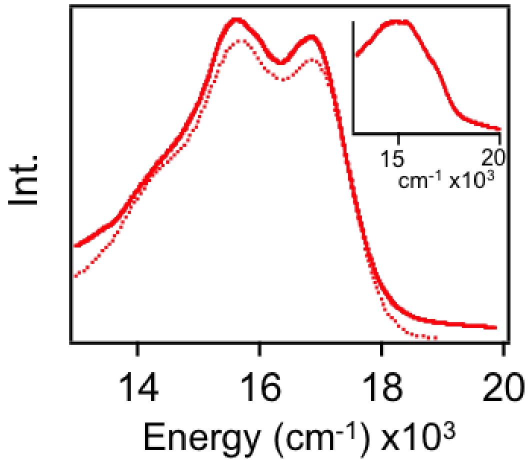

**Figure 3.2.2.2** Fluorescence emission spectra of MDMO-PPV thin films (solid trace) and fit (dotted trace). Inset: annealed MDMO-PPV thin film emission spectrum.

Based on the MIME model this indicates a larger contribution from higher frequency modes but the specific structural change is not clear from these intervals. We apply the time-dependent approach described previously to understand the change in MIME frequency and quantitatively estimate the change in the mode-specific excited state displacements.

Because of large fluorescence and scattering backgrounds present in pre-resonance Raman spectra of these systems, small amounts of PCBM were added (~1 wt. %) to sufficiently quench emission to levels that permitted the measurement of Raman spectra. No significant changes in the overall emission envelope profile or MIME progression interval were observed with the small addition of fullerenes. Raman intensities and relative displacements collected from pristine films are shown in Table 3.2.2.1 and used for the simulation of both pristine nanoparticles and thin films.

**Table 3.2.2.1** Pre-resonance Raman intensity ratios and relative emitting displacements for MDMO-PPV nanoparticles, thin films, and fullerene composite films (1:1 w/w).

| | NP,[a] film[b] | | | 1:1 MDMO-PPV/PCBM[c] | | |
|---|---|---|---|---|---|---|
| Mode | $I_k/I_{[1]}$ | $\Delta_k/\Delta_{[1]}$ | $\Delta_{\text{calc.}}$ | $I_k/I_{[1]}$ | $\Delta_k/\Delta_{[1]}$ | $\Delta_{\text{calc.}}$ |
| [1] | 0.17 | 0.68 | 0.58, 0.64 | 0.089 | 0.49 | 0.55 |
| [2] | 0.19 | 0.62 | 0.53, 0.59 | 0.10 | 0.45 | 0.50 |
| [3] | 0.41 | 0.79 | 0.67, 0.75 | 0.30 | 0.67 | 0.76 |
| [4] | 0.53 | 0.88 | 0.75, 0.84 | 0.43 | 0.79 | 0.89 |
| [5] | 1.00 | 1.00 | 0.86, 0.95 | 1.00 | 1.00 | 1.12 |
| [6] | | | | 0.22 | 0.46 | 0.51 |

Values of fit parameters used in eq. 2 for $E_{00}$ ($\text{cm}^{-1}$) and $\Gamma$ ($\text{cm}^{-1}$) were: [a] 17045, 325; [b] 16980, 370; [c] 16810, 385.

Fit spectra are shown as dotted traces with the experimental spectra offset for clarity that show excellent agreement. Because a large number of interchain contacts exist between polymer molecules it is possible that the increase of the MIME frequency results from changes in the conformational characteristics of the polymer. Comparison of relative displacements of modes [1] and [5] reveal substantial reductions in the former, which was assigned to an out-of-plane C-H bend. This decrease suggests a change in chain planarity since this mode is formally forbidden in a planar structure. Large red-shifts, broadening and reductions in intensity are noted that are similar to features reported previously in related PPV systems.[77] These trends are consistent with the formation of excimer-type or interchain species that result from strong interactions amongst chain segments. We further consider the roles of interchain interactions on polymer structure using the MIME model to extract mode-specific structural changes.

A major advantage of polymer as optoelectronic materials is the facile tunability of their properties by adding other materials that induce small structural and electronic perturbations. It is now interesting to study the polymer emission lineshape in the presence of an additive. This type of blend composite structure is frequently encountered in solar cells where fullerenes are added to polymers to split neutral excitons into free charge carriers. These so-called bulk heterojunction systems often achieve high charge generation yields but are plagued by short lifetimes[78] and poor charge transport characteristics resulting in wasteful recombination processes.[79] The addition of fullerenes can also disrupt packing interactions between polymer chains and cause significant changes in the polymer structure.

McGehee and co-workers recently proposed that intercalation of the fullerene molecules between the MDMO-PPV substituent groups causes a planarization of the polymer chain resulting in large increases of charge mobilities.[80] This possibility is discussed at length in the next chapter.

## 3.3 Conclusions

In summary, the implications of multiple excited state vibrational displacements in MDMO-PPV are quite significant for optoelectronic applications since electronic length scales are affected by the specific geometry of the molecule.[64b] The increase of the MIME frequency in MDMO-PPV thin films is the result of a change in planarity of the polymer chains. These changes are quantified from pre-resonance Raman intensities that are used to estimate mode-specific displacements used in emission spectra simulations. In dilute solutions, polymer chains take on more twisted conformation causing increases in the out-of-plane C-H bend displacement and a lower MIME frequency. Upon deposition into thin films or precipitation of nanoparticles, polymer chains are packed tightly together and become more planar presumably due to interactions between alkoxy side chains. Most importantly, the MIME can be used as a measure of polymer chain planarity that should be highly sensitive to morphological heterogeneity effects.

# Chapter 4

# Effect of Fullerene Intercalation on the Conformation and Packing of Poly(2-methoxy-5-(3'-7'-dimethyloctyloxy)-1,4-phenylenevinylene)

Reproduced with permission from

*ACS Appl. Mater. Interfaces* **2011**, 3, 3011-3019

## 4.1 Introduction

### 4.1.1 Conformation and Packing of Conjugated Polymers

The conformational and packing characteristics of conjugated polymer chains in polymer/fullerene solar cell blends plays a vital role in determining overall material

---

[*] This article has been edited slightly and re-formatted to better fit into the dissertation, and some supplemental information has been added, but is largely unchanged.

performance.[6c, 64a, 81] Recent structural studies using X-ray techniques have shed light on the nature of interaction between polymers and fullerene additives[82] and new insights into the structural factors influencing optimal polymer/fullerene loadings and morphology are beginning to emerge.[6a, 83] In particular, it was proposed that fullerene molecules can intercalate into the polymer structure when there is sufficient volume between solubilizing side groups (>1 nm).[80, 82]

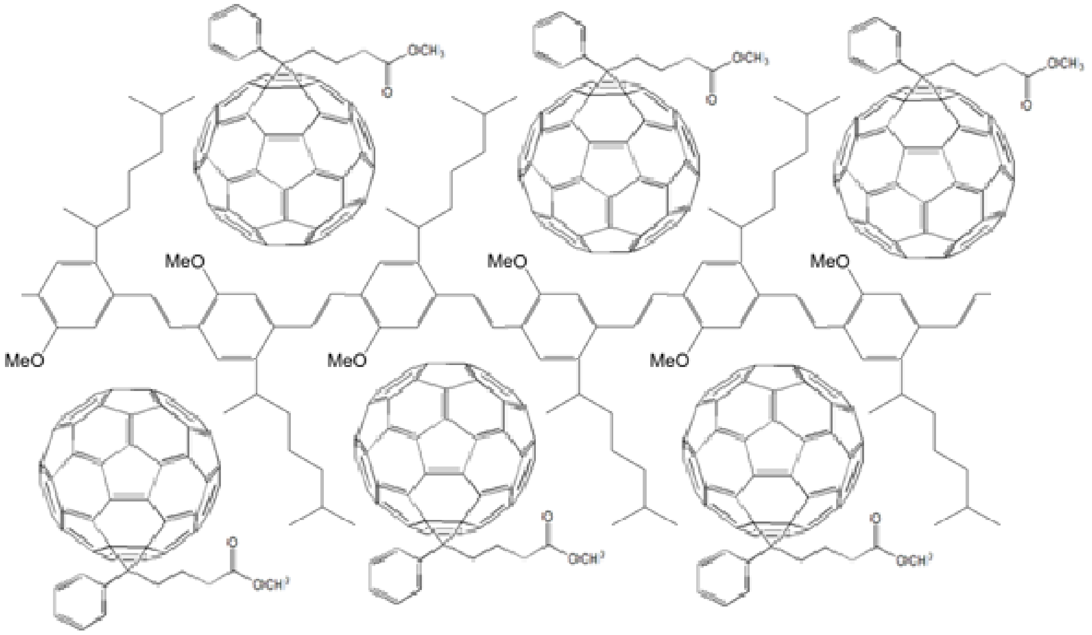

**Figure 4.1.1** A cartoon showing a possible arrangement of PCBM occupying sites between the side chains of MDMO-PPV.

The most compelling evidence for this phenomenon occurs in the semi-crystalline polymer poly-(2,5-bis(3-tetradecyllthiophen-2-yl)thieno[3,2-b]thiophene) (PBTTT) where d-spacings between polymer chains appear to increase upon addition of a fullerene derivative.[82a] This feature also explains why some non-intercalating polymers (i.e., poly-3-hexylthiophene) exhibit optimal polymer/fullerene loading ratios of ~1:1 weight:weight whereas potentially intercalating systems show optimal loadings as high as 1:4 weight:weight polymer:fullerene.

Unfortunately, not all polymers are amenable to X-ray techniques due to their lack of extended order (crystallinity), and intercalation must be inferred indirectly from optimal loading characteristics used in solar cell devices, changes in charge mobilities, and PL quenching. MDMO-PPV, an amorphous polymer, requires high fullerene loadings (1:4 weight:weight) to achieve reasonable solar cell power conversion efficiencies (~3%). Interestingly, charge mobility measurements of MDMO-PPV/fullerene thin films showed large increases (about two orders of magnitude) compared to pristine MDMO-PPV films.[84] The longstanding explanation for these increases of hole mobility is that MDMO-PPV chains uncoil and elongate with addition of PCBM resulting in higher intra-chain order (i.e., increased conjugation length and planarity between segments) and increased inter-chain interactions.[84]

More recently, McGehee and co-workers proposed that intercalation of acceptor molecules is responsible for enhancement of charge mobility in MDMO-PPV blends which was inferred from space-charge limited current (SCLC) studies of various MDMO-PPV/acceptor blends.[80] Only intercalating acceptors (i.e., $C_{60}$ and $C_{70}$ derivatives) showed increased hole mobilities whereas addition of other small molecules showed little change in measured charge mobilities suggesting little or no intercalation into MDMO-PPV chains.[80] In addition, the nearly quantitative quenching of MDMO-PPV PL has also been taken as direct evidence of fullerene intercalation due to efficient photoinduced charge transfer between the intimately mixed components.

Thermal annealing MDMO-PPV/fullerene blend films causes components to phase separate, and SCLC mobility values return to approximately the original pristine-polymer value, presumably due to removal of intercalated fullerenes from the polymer structure.[80] However, the annealing conditions (130°C for one hour) can cause extreme phase segregation on a >1μm scale, complicating SCLC measurements.

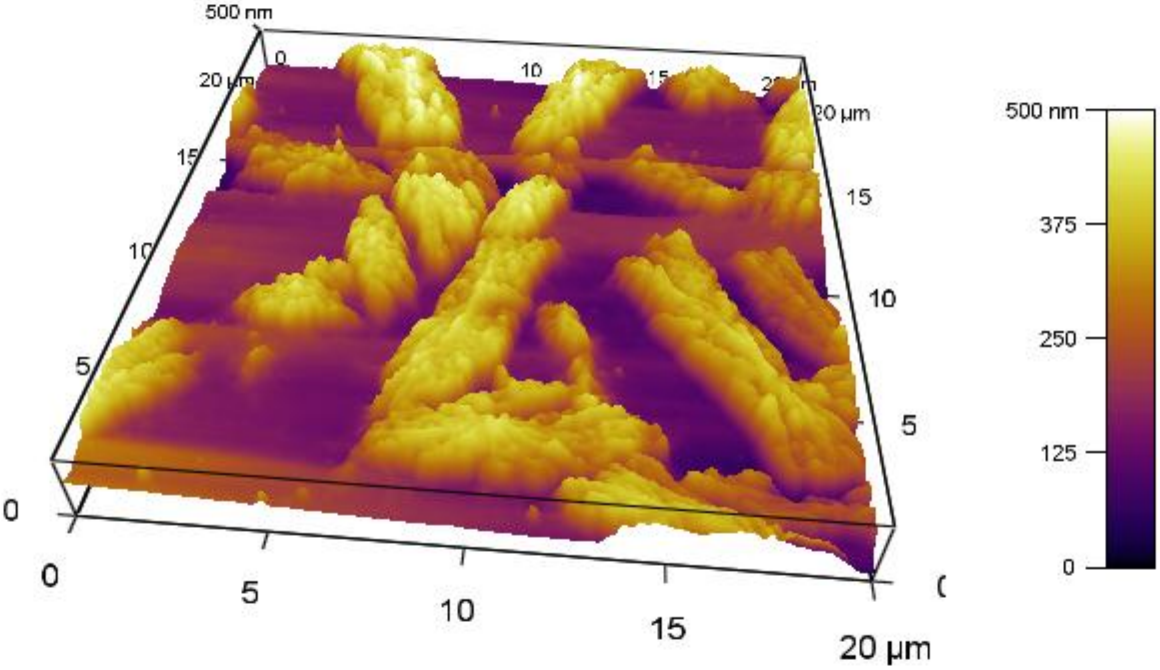

**Figure 4.1.2** Atomic force microscopy height image of a thermally annealed 1:4 MDMO-PPV:PCBM thin film on glass. The light-colored features are areas of extreme phase segregation, most likely dendritic PCBM crystals covered with a thin layer of pure

MDMO-PPV. Film roughness increases after thermal annealing, perhaps interfering with electrical measurements.

Because of the inability of PL quenching and X-ray techniques to directly report on the polymer chain conformation and packing changes in MDMO-PPV blends with high acceptor loadings (>1:1 w/w), it is necessary to seek alternative methods to understand the role of fullerene intercalation on polymer conformations.

### 4.1.2 Resonant Raman Spectroscopy of MDMO-PPV:PCBM Blend Films

Raman spectroscopy is a technique that can uncover the structural attributes of polymer chains and how they change with the addition of fullerene acceptors. Raman spectroscopy allows for sensitive and non-destructive investigations of chemical structure and changes with material processing conditions and additives. By careful choice of excitation wavelengths (energies) it is also possible to selectively excite a single component in complex systems (i.e., polymer/fullerene blends) by tuning the laser to a particular optical transition. This resonance excitation scheme typically results in large enhancements of Raman scattering cross-sections for certain vibrational modes (i.e., Franck-Condon active vibrational modes) that also greatly simplifies the Raman spectrum.[85] For this reason, resonance Raman spectroscopy is especially useful for investigating polymer/fullerene blends since polymer PL backgrounds are strongly suppressed which often overwhelm weaker Raman transitions. Furthermore, polymer backbone vibrations that report on the $\pi$ electronic structure are sensitive to minor changes in the local environment and the presence of dopants.

This feature in particular makes Raman spectroscopy an excellent tool for understanding chain conformation and packing effects on electronic properties such as conjugation lengths and polaron formation.[86] Raman techniques are also amenable to imaging studies which can reveal the spatial variation of chemical structure and packing on sub-micron size scales in a highly selective manner.[6b, 81a, 87]

Bruevich et al. have used resonance Raman spectroscopy to study the degree of charge transfer and changes of polymer chain conformations in a poly-phenylenevinylene derivative similar in structure to the title polymer (i.e., MEH-PPV) blended with tri-nitrofluorenone (TNF) acceptor molecules.[24, 88] Raman spectra of MEH-PPV/TNF blend thin films of varying loadings (up to 1:1 w/w) showed substantial frequency and intensity shifts in the dominant C-C symmetric stretch of the phenyl ring (~1580 $cm^{-1}$) and the out-of-plane vinylene C-H wag mode (~966 $cm^{-1}$), respectively. Red-shifts of up to 5 $cm^{-1}$ were observed for the ~1580 $cm^{-1}$ mode with increasing TNF concentration. These trends were believed to be evidence of cofacial packing of MEH-PPV segments and TNF molecules that also result in the formation of a ground state charge transfer complex. Concomitant large blue-shifts of up to 7 $cm^{-1}$ and decreasing intensities were also demonstrated for the ~966 $cm^{-1}$ mode with increasing TNF concentration that confirmed increases of planarity between chain segments because of the forbiddeness of this mode in planarized conformations.[22]

Why should this mode be forbidden when the molecule is planar? In the idealized $C_{2h}$ symmetry group, complete planarity means that the probability distribution of every electronic state should be symmetrical across the plane of the molecule. The transition between two states that have the molecular plane as a mirror plane shouldn’t be able to "push" any nuclei into vibrational modes normal to that plane, as the electron density should always be the same below and above it. Only distortions of the planarity will allow vibrations normal to the plane to sneak into the Raman or PL spectra.

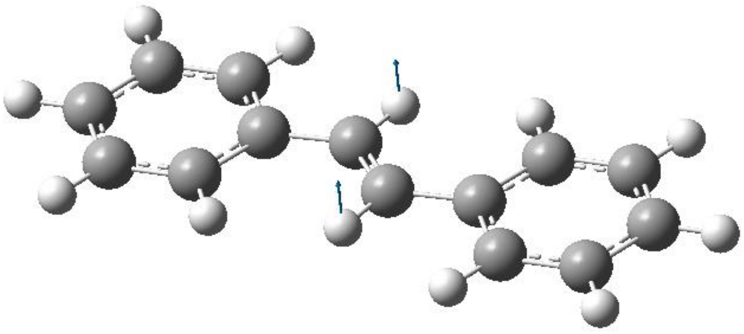

**Figure 4.1.2.1** Illustration of an analogous out-of-plane vinyl C-H vibrational mode in the small molecule trans-stilbene. The small blue arrows are vectors showing the displacement of the vinyl hydrogen atoms.

In addition to blend thin films commonly used in solar cell applications, polymer chain conformational and packing effects have been extensively studied for homo-polymer systems with different processing conditions.[89] For example, there has been a great deal of interest and controversy surrounding the existence and physical origin of so-called aggregate or inter-chain excitons in related PPV systems. Aggregate species have been studied in great detail using various frequency- and time-resolved spectroscopic and scanned probe techniques and the general consensus resulting from this body of work is that slow solvent evaporation and/or annealing of films leads to a greater number of inter-chain aggregate species.[64a] Schwartz and co-workers proposed that PPV chains with asymmetric side group substitution uncoil upon annealing permitting greater inter-chain interactions.

On the other hand, Janssen and co-workers have shown that MDMO-PPV chains tend to self-aggregate and adopt coiled conformations due to the unsymmetric backbone substution pattern that do not change upon annealing.[90] Regardless of the type of aggregate, both inter- and intra-chain aggregates show similar red-shifted PL maxima, diminished yields and sometimes non-Poissonian lineshapes.[91] Application of hydrostatic pressures have also revealed similar trends in PL spectra to those generated from most annealed films where pressure causes polymer chain segements to planarize and close-pack.[92] While shifting PL energies and changes in PL lifetimes are effective diagnostics of the chain packing characteristics, the vibronic lineshape parameters (i.e., Huang-Rhys factors and linewidths) also provide valuable insight into the polymer structure and changes in molecular geometry between ground and excited states.

In the previous chapter, it was shown that the experimental vibronic intervals in MDMO-PPV PL spectra do not match any ground state vibrational frequency, which is known as the missing mode effect (MIME).[93] The MIME arises from the coalescence of transitions from several displaced modes that results in an effective PL vibronic interval. The values of MIME intervals are determined primarily by the relative contribution of each displaced mode (Huang-Rhys factor) as well as the frequency. In MDMO-PPV PL spectra, the MIME interval changes from ~1225 $\text{cm}^{-1}$ (solution) to ~1350 $\text{cm}^{-1}$ (films) which reflects varying contributions (i.e., displacements) of at least five backbone modes depending on chain conformation and packing characteristics in each sample form.[16] Importantly, the out-of-plane vinylene C-H wag mode of MDMO-PPV showed the greatest sensitivity to processing-dependent chain conformation and packing with large (>50%) decreases from solution to condensed forms which is consistent with earlier Raman and IR spectroscopic studies of unsubstituted PPV derivatives.[22]

Analysis of PL lineshapes are fundmentally limited in their capability to resolve specific structural changes in conjugated polymers mainly owing to efficient quenching, especially for larger fullerene loadings (>1:1 w/w) commonly used in solar cells. Here we use a combination of resonance Raman and PL spectroscopy to investigate the effect of MDMO-PPV structure upon addition of PCBM over a wide range of loadings. Chain conformation and packing interactions and their impact on excited state relaxation to low energy inter-chain sites are first studied in the absence of PCBM to identify and understand the spectroscopic markers of conformational and packing arrangements of these molecules. Both frequency- and time-resolved PL spectra reveal changes in lineshape, energy and dynamics upon thermal annealing that are indicative of increased inter-chain site formation. Addition of PCBM inhibits inter-chain interactions and PL lineshapes bear increasing resemblance to those of dilute solution samples, i.e., blue-shifted 0-0 transition energies and lower apparent Huang-Rhys factors. However, the strong quenching of MDMO-PPV PL with high PCBM loadings (>1:1 w/w) makes the use of PL spectroscopy difficult to reliably understand chain conformation and packing characteristics.

Resonance Raman spectroscopy is employed to selectively study MDMO-PPV conformational and packing characteristics with various PCBM loadings across the inhomogeneously broadened ground state optical absorption envelope. Short (488 nm) and long (568 nm) excitation wavelengths are used to excite into high and low energy regions, respectively, of MDMO-PPV optical absorption transitions. As PCBM content increases, the out-of-plane vinylene C-H band of MDMO-PPV (~964 $cm^{-1}$) showed substantial increases in intensity and linewidth as well as red-shifts for both excitation wavelengths. Because this mode is formally forbidden in planar conformations, these trends indicate that intra-chain order decreases, namely, a loss of coplanarity between polymer chain segments resulting in a reduction in average conjugation lengths and blue-shifts in PL energies.

The C=C symmetric stretching mode of the MDMO-PPV vinylene group (~1625 $cm^{-1}$) also shows similar intensity increases and red-shifts as the ~964 $cm^{-1}$ mode for 488 nm excitation only. Overall, the sensitivity of the MDMO-PPV vinylene linkage indicates that PCBM interacts preferentially with this group. MDMO-PPV chains blended with PCBM become more distorted with the loss of planarity between chain segments and shorter conjugation lengths that suggests conformations similar to dilute solutions. The implications of these structural changes in MDMO-PPV chains on the origins of charge mobility enhancements in PCBM blends are discussed.

## 4.2 Results and Discussion

We first study MDMO-PPV thin films prepared under different conditions (i.e., annealing) in the absence of PCBM with PL spectroscopy. Figure 5.2.1.1 shows PL spectra of MDMO-PPV thin films with variable annealing times (0s, 30s, and 300s at 130 °C). As-cast films show a vibronic lineshape pattern similar to that of the solvated polymer (not shown) albeit lower energy. Upon annealing, several lineshape parameters change noticeably: i) an apparent increase in the Huang-Rhys factor, or suppression of the 0-0 vibronic component intensity, ii) red shifting of the electronic origin by ~300 $cm^{-1}$, iii) linewidth broadening of vibronic transitions. PL decays for variable annealing MDMO-PPV thin films are shown in Figure 5.2.1.2 measured at two distinct emission wavelengths, namely at the PL onset and tail that are indicated by arrows.

### 4.2.1 Time Correlated Single Photon Counting Measurements

Time-correlated single photon counting measurements of as-cast (pristine) films and films with short annealing times show non-exponential decays with an instrument-limited component ($\tau_1$ ~100 ps) and a longer-lived component ($\tau_2$ ~350 ps) for both blue and red extremes of the spectral envelope. Longer annealing times (300s) result in nearly mono-expontial decays of $\tau$ ~ 900 ps and 1.1 ns measured at both blue and red regions, respectively.

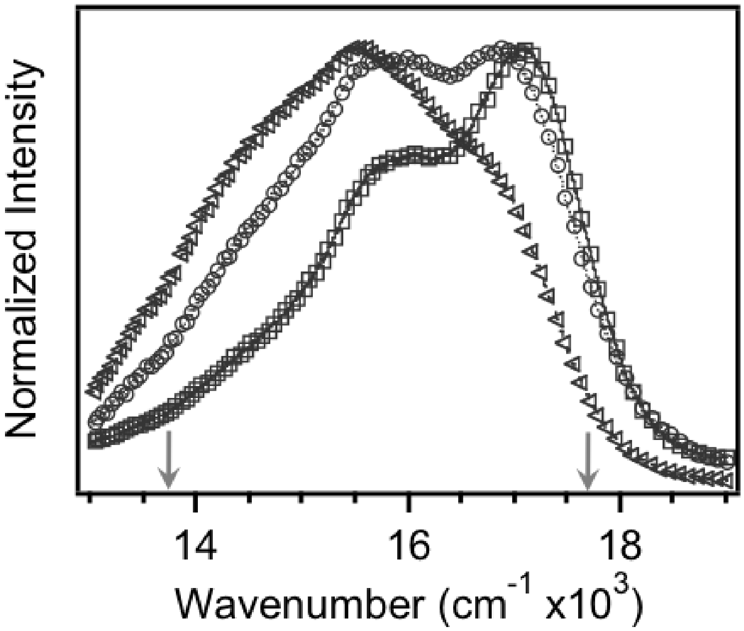

**Figure 5.2.1.1** Photoluminescence (PL) spectra of pristine MDMO-PPV thin films with variable annealing times: 0s, as-cast (□); 30s (O); 300s (◁). Arrows indicate emission energies used to measure PL lifetimes changes with annealing.

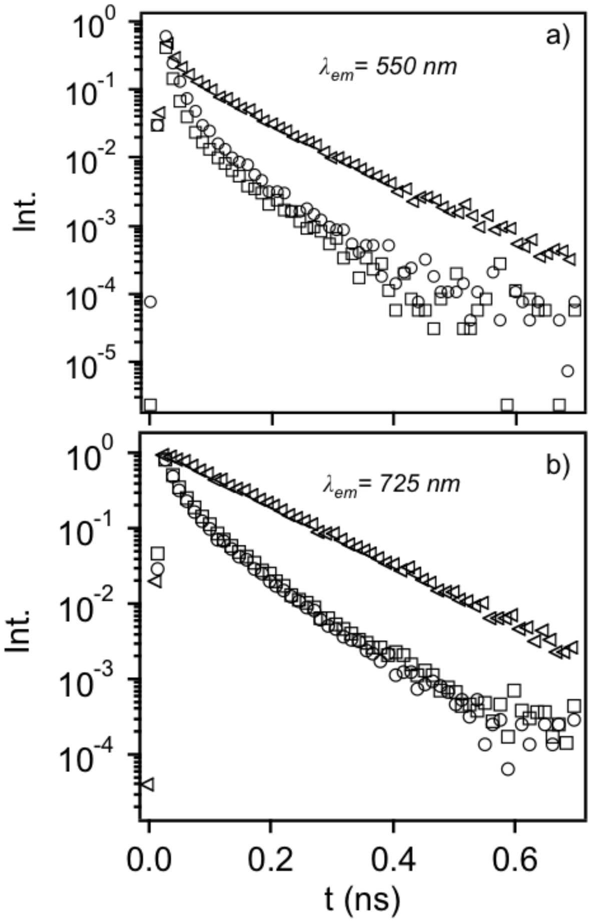

**Figure 4.2.1.2.** PL lifetimes of pristine MDMO-PPV thin films with variable annealing times: 0s, as-cast (□); 30s (O); 300s (◁) measured at the PL onset (a) and tail (b).

### 4.2.2 Photoluminesence Measurements

When fullerenes are added to conjugated polymers, the ability of polymers to close-pack is hindered and PL signatures deviate from the behavior shown in the figures above. Figure 4.2.2.3 shows the dependence of the PL 0-0 transition energy ($E_{0\text{-}0}$) for annealed MDMO-PPV (Fig. 5.2.2.3a) and MDMO-PPV/PCBM as-cast films with variable PCBM content (5.2.2.3b). $E_{0\text{-}0}$ values were determined by fitting a Gaussian function to this peak in the PL spectrum, which also reveals the effective range for which the PL transition can be tuned by altering chain conformation and packing. Upon addition of PCBM, $E_{0\text{-}0}$ values show considerable blue-shifts of up to ~600 $cm^{-1}$ and increases of the 0-0 relative intensity that approach values obtained from MDMO-PPV PL spectra in dilute chlorobenzene solution.

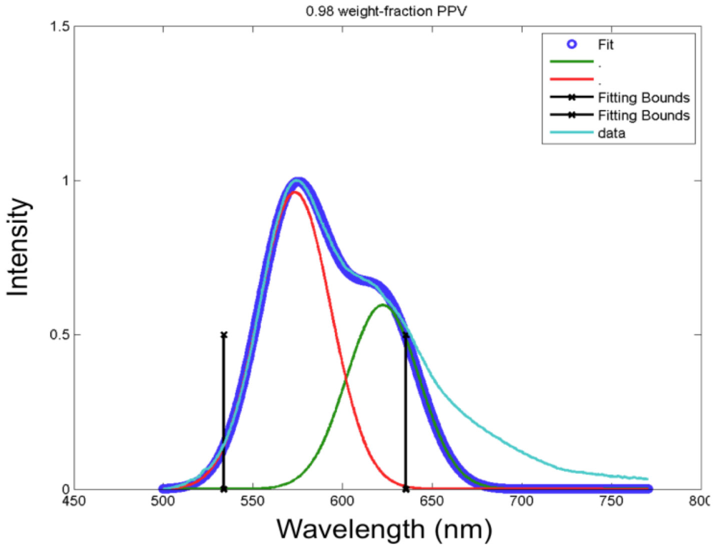

**Figure 4.2.2.1** Photoluminescence spectra and multi-Gaussian fit of a lightly doped (2% weight PCBM) MDMO-PPV film. No PCBM photoluminescence is seen, and the

Resonant Raman scattering is almost completely undetectable. The peak of the PL spectra is around 580nm, typical of a solid MDMO-PPV film.

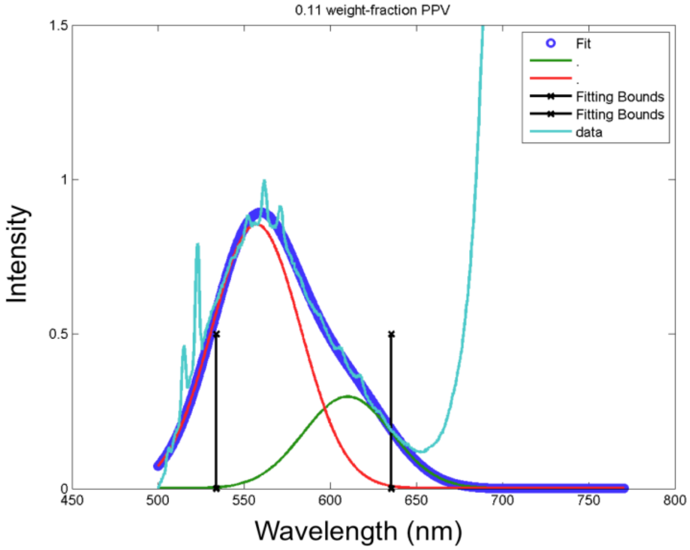

**Figure 4.2.2.2**: Photoluminescence spectrum and multi-Gaussian fit of a heavily doped (89% weight PCBM) MDMO-PPV blend film. PCBM photoluminescence dominates (off-scale trace centered at 750nm), and the Resonant Raman scattering is easily seen (sharp lines in cyan-colord data trace). The peak of the PL spectra is around 560nm, typical of MDMO-PPV dissolved in an organic solvent. The structure of the PL spectrum at high PCBM loadings is very poorly resolved.

These trends suggest that the average conjugation lengths become smaller and chain packing is disabled which is discussed in detail in the following. PCBM loadings higher than ~60% showed large reductions in signal-to-noise ratios and increased broadening that made the determination of lineshape parameters difficult. Fortunately, these limitations can be surpassed by resonance Raman spectroscopy that provides more reliable information about the polymer conformation characteristics with PCBM in addition to the specific nature of interaction between the polymer and fullerene molecules.

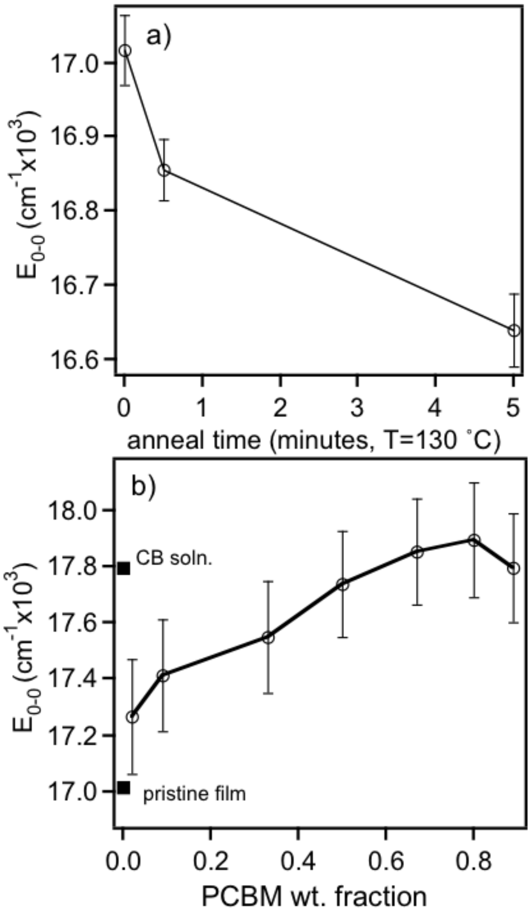

**Figure 4.2.2.3.** a) Photoluminescence $E_{0\text{-}0}$ as a function of annealing time for pristine MDMO-PPV films. b) Effect of PCBM weight fraction on $E_{0\text{-}0}$ of MDMO-PPV PL spectra. $E_{0\text{-}0}$ values ( ■ ) from chlorobenzene (CB) and pristine thin films are shown for comparison. Error bars correspond to ± one standard deviation of the mean values.

### 4.2.3 Resonant Raman Spectroscopy of Blend Films

Figure 4.2.3.1 shows Raman spectra for as-cast MDMO-PPV/PCBM thin films with variable PCBM content in the range of 50:1 up to 1:8 w/w with, a) 568 nm and b) 488 nm excitation wavelengths. These wavelengths were chosen to study the conformational and packing attributes of longer and shorter MDMO-PPV chain segments, respectively, and spectra were recorded in the range of ca. 900—1700 $cm^{-1}$ to monitor MDMO-PPV backbone vibrations with variable PCBM content. The Raman bands have been assigned previously for PPV derivatives[22, 68a] which correspond to the out-of-plane C-H wag of the vinylene group (~964 $cm^{-1}$); C-C stretching/C-H bending of the phenyl group (~1111 $cm^{-1}$); C-C inter-ring stretching (~1280 $cm^{-1}$); C=C stretching/C-H bending of the vinylene group (~1305 $cm^{-1}$); C-C stretching of the phenyl group (~1580 $cm^{-1}$); and C=C stretching of the vinylene group (~1625 $cm^{-1}$). All Raman spectra were normalized to the dominant ~1580 $cm^{-1}$ mode and changes in intensities and frequencies of Raman bands are determined by fitting each band to a single Lorentzian function. The most noteworthy feature of these spectra is the increase in relative intensities and red-shifts of the vinylene out-of-plane C-H mode (~964 $cm^{-1}$) with increasing PCBM loading which are highlighted in the insets of the figures below. Similar red-shifts (~4 $cm^{-1}$) and relative intensity increases were observed for the MDMO-PPV vinylene C=C symmetric stretch (~1625 $cm^{-1}$) when blends were excited with 488 nm light. However, 568 nm excitation showed no apparent changes in this band with increasing PCBM loading. Importantly, no apparent frequency shifts were observed for phenyl group vibrations with the choice of excitation wavelength or PCBM loading implying that refractive index dispersion effects can be ruled out as the origin for the

PCBM-dependent shifts of vinylene group modes. Raman transitions from the PCBM component are not observed except at very high loadings (>80%) where the C=C symmetric breathing vibration (~1460 cm$^{-1}$) becomes barely discernible in background shot noise. This feature further highlights the capability of resonance Raman spectroscopy to selectively interrogate polymer structure in blends with large acceptor loadings that is not otherwise possible using PL spectroscopy. To further understand the nature of MDMO-PPV structural distortions with varying PCBM content we turn our attention to the ~964 cm$^{-1}$ mode to establish how MDMO-PPV/PCBM interactions influence polymer conformations in blends.

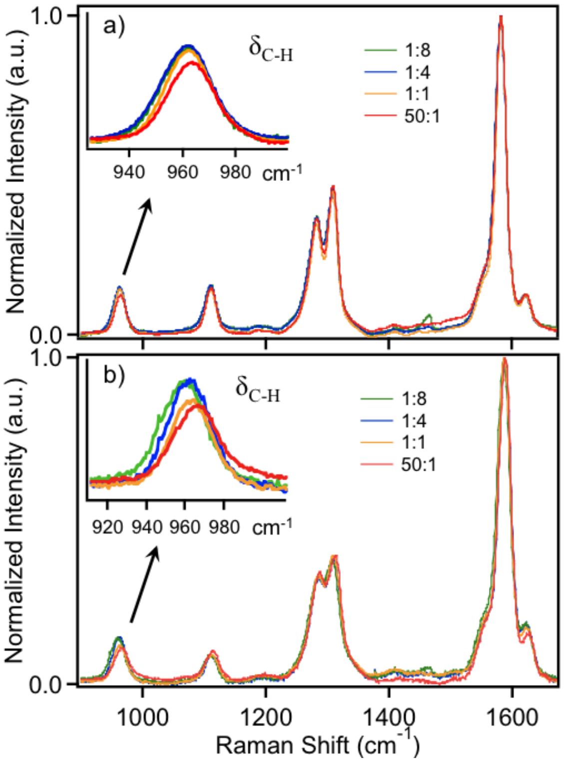

**Figure 4.2.3.1.** Representative Raman spectra of as-cast MDMO-PPV/PCBM thin films with variable PCBM weight fractions generated with a) 568 nm and b) 488 nm excitation

wavelengths. Insets show the out-of-plane vinylene C-H wag band of MDMO-PPV (~964 cm$^{-1}$).

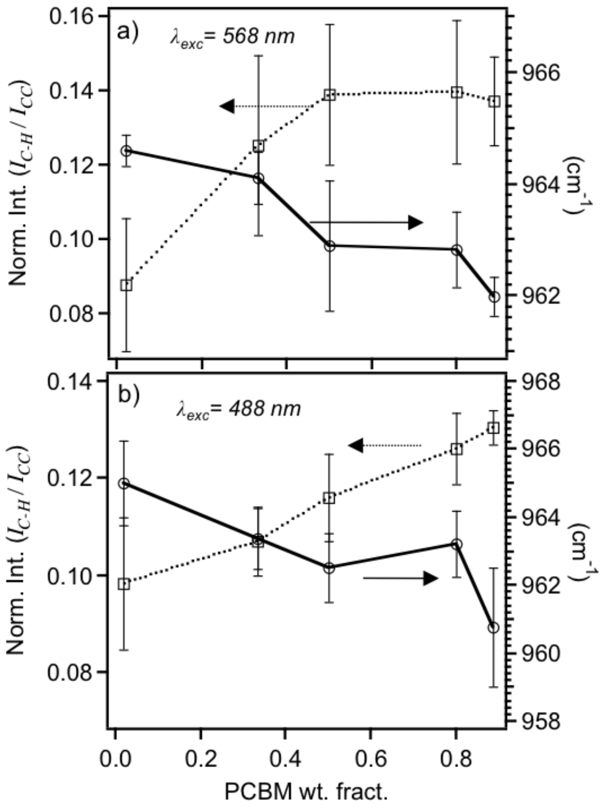

**Figure 4.2.3.2.** Effect of PCBM weight fraction on the frequency (-□-) and normalized intensity (···□···) of the out-of-plane vinylene C-H wag mode of the MDMO-PPV component for as-cast thin films generated from, a) 568 nm and b) 488 nm excitation wavelengths. Error bars represent ± one standard deviation of the mean values.

Figure 4.2.3.2 shows the effect of PCBM content on the relative intensities and frequencies of the MDMO-PPV ~964 cm$^{-1}$ mode. Both excitation wavelengths show similar trends with the same PCBM loading albeit spectra excited with 568 nm light show less pronounced red shifts (~3 $cm^{-1}$) compared to red shifts of up to 5 $cm^{-1}$ for spectra excited with 488 nm light. The relative intensities of this mode ($I_{C\text{-}H}/I_{CC}$) show increases ~30% between the lowest (50:1 w/w) to highest (1:8 w/w) PCBM loading for both excitation wavelengths. The overall similarity of the relative intensity increases and red-shifts of the ~964 $cm^{-1}$ mode for short and long wavelength excitation suggest that PCBM interactions for both short and long chain segments are likewise similar. We consider the origins for these changes in detail in the Discussion section.

Annealing treatments (130 °C, 5 min) were applied to MDMO-PPV/PCBM films to promote phase separation between both components and Raman spectra for various PCBM loadings are shown in Figure 4.2.3.3. Figure 4.2.3.3a shows Raman spectra for annealed MDMO-PPV/PCBM films excited at 488 nm and Figure 4.2.3.3b shows intensity and frequency changes with varying PCBM content. Importantly, the relative intensities of the ~964 $cm^{-1}$ mode were considerably smaller in annealed films compared to as-cast films of the same PCBM loading and also showed increases of only ~15% over the entire range of PCBM loadings studied. Frequency shifts of this mode are also diminished compared to as-cast films which only red-shift by ~2 $cm^{-1}$ between loadings of 50:1 to 1:8 w/w. Furthermore, linewidths of the ~964 $cm^{-1}$ mode were narrower indicating less overall disorder in the annealed film. On the other hand, red-shifts of up to 3 $cm^{-1}$ were observed in the ~1625 $cm^{-1}$ mode in annealed films which are comparable to the red-shifts found in as-cast films using 488 nm excitation. It was not possible to obtain reliable spectra for large PCBM loadings using 568 nm excitation due to large PL backgrounds resulting from greater phase separation between both components of the blend due to the comparatively longer annealing times used.

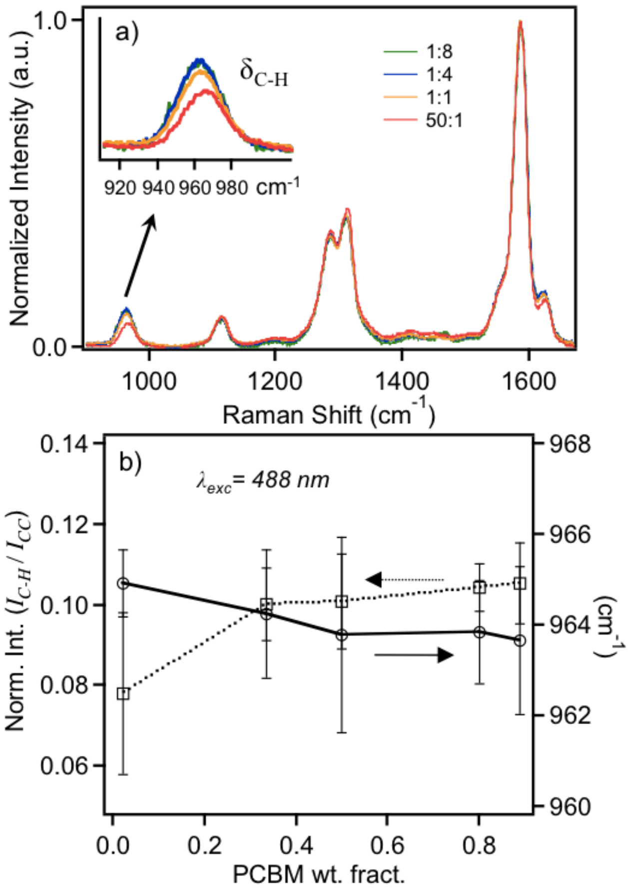

**Figure 4.2.3.3.** a) Raman spectra of annealed MDMO-PPV/PCBM thin films with variable PCBM weight fractions generated with 488 nm excitation. The inset shows the ~964 $\text{cm}^{-1}$ band of the out-of-plane C-H wag mode of the vinylene group of MDMO-PPV. b) Effect of PCBM weight fraction on the frequency (--o--) and intensity (···□···) of the out-of-plane vinylene C-H bending vibration of the MDMO-PPV component. Error bars represent ± one standard deviation of the mean values.

Polymer spectroscopic lineshapes and photophysics have long been known to be sensitive to chain conformations and interactions that are perturbed by annealing treatments (thermal or solvent vapor) as well as applied hydrostatic pressures. Spectroscopic manifestations of chain-chain interactions are diminished PL yields and 0-0 intensities in addition to prominent red-shifts as a result of a greater number of π-π stacked chains that comprise the bottom of excited state energy funnels. Intuitively, these interactions should be most favorable when individual polymer chain conformations are elongated and coplanarity exists between individual segments. Aggregation occurs either by the polymer chain folding back onto itself (intra-chain) or through interactions between neighboring polymer chains (inter-chain) but these structures can be difficult to distinguish solely from PL spectroscopy. Using scanned probe techniques, Janssen and co-workers showed that intra-chain aggregation occurs in MDMO-PPV films owing to the unsymmetric backbone substitution pattern and annealing of films did not change the type of aggregation as seen from both PL lineshapes and film topographies.[90] Schwartz and co-workers proposed that annealing of related alkoxy substituted PPV systems results in an unraveling of polymer chains that favors inter-chain aggregation.[89b, c]

Previous IR and Raman spectroscopic studies of unsubstituted PPV derivatives also show that chains planarize and close-pack as seen from significant decreases of the intensities of the out-of-plane C-H wag of the vinylene group (~963 $\text{cm}^{-1}$) in films.[22] Because of the relatively low molecular weight of the MDMO-PPV sample used, inter-chain aggregation is expected to dominate upon annealing that should enhance funneling to low energy emissive traps resulting in red-shifts and decreases in the 0-0 transition intensity. Indeed, the 300 $\text{cm}^{-1}$ red-shift of PL energies, linewidth broadening and apparent increase of the lineshape Huang-Rhys factor with longer annealing times are consistent with these structural changes. In addition, the PL vibronic intervals provide important insights into changes in chain conformation and packing that change depending on the sample processing conditions. For example, we previously showed that the MDMO-PPV PL vibronic progression interval does not match any ground state vibrational frequency and represents the coalescence of transitions from the backbone modes.[16] This phenomenon is known as the missing mode effect (MIME) and has also been reported for other PPV derivatives.[15] In MDMO-PPV PL spectra, the observed MIME intervals increase from ~1225 cm$^{-1}$ to ~1350 cm$^{-1}$ between dilute solutions and thin films, respectively. The chief factor for the increase of the MIME interval is the decreasing displacement of the ~964 cm$^{-1}$ mode as seen from corresponding Raman intensities. This feature indicates an increase in intra-chain order or, co-planarity between chain segments in thin films which was confirmed by applying annealing treatments resulting in further intensity decreases of the ~964 cm$^{-1}$ mode.

Application of hydrostatic pressures on conjugated polymers also give rise to similar changes in PL spectra as shown above. For example, conjugated organic molecules are known to planarize at higher pressures[94] which enables better inter-chain electronic communication. Pressure-dependent PL spectra of related PPV derivatives likewise exhibit significant reductions in the 0-0 transition intensity as well as overall red-shifts and broader linewidths.[95] The changes in MDMO-PPV PL lineshapes with different annealing times (i.e., decreasing 0-0 intensity) may be the result of H-aggregates which show non-Poissonian lineshapes similar to those shown above. This effect has been observed in polythiophenes and can be effectively modeled using the weakly coupled H-aggregate model developed by Spano and co-workers. However, the fact that MDMO-PPV PL spectra show stronger red-shifts and broadening with longer annealing times suggests that inter-chain coupling in this system does not fall in the same regime as seen in polythiophenes. To better understand the extent of inter-chain coupling and their implications on PL signatures, we turn to PL lifetime data which helps sort out ambiguities of PL lineshapes.

Comparison of PL decays measured at either the blue onset or red tail of the PL lineshape reveal similar characteristics albeit a ~20% larger contribution of the fast (instrument limited) component observed for decays measured on the PL onset (~550 nm). Because polymer chains cast from solution primarily exist in distorted conformations, inter-chain packing is not optimal and excitons migration is limited to hopping along the chain before decaying within their lifetime. Pristine (as-cast) and films annealed for short times (~30 s) more closely resemble solution-like chain conformations and PL decays are non-exponential indicating incomplete energy funneling. The short- and longer-lived components of these decays likely correspond to emission from partially aggregated chains and distorted chains, respectively. Annealing films for longer times results in better inter-chain interactions and stronger electronic coupling between neighboring segments which is promoted by increased intra-chain order. Correspondingly, lifetimes were nearly single exponential demonstrating complete energy funneling to inter-chain sites. The long decay times and broad, red-shifted spectra for MDMO-PPV films annealed >300s resemble excimer-like transitions that have been observed in other PPV derivatives.[96] These data suggest a two-emitter system comprised of both intra- and inter-chain species, the latter exhibiting a wide range of electronic coupling strength. As-cast films exhibit primarily intra-chain character which is evident from both PL lineshape and decay features. In contrast, longer annealing results in stronger inter-chain character (coupling) and all excitations migrate to these sites within their lifetime. Assuming exciton migration lengths of ~4-5 nm, as little as one of these sites within this range can dominate the PL spectral and decay features. Schwartz and co-workers observed similar trends in MEH-PPV films that were attributed to increased inter-chain interactions. Based on the changes in vibronic lineshape and decay features, we conclude that MDMO-PPV chains planarize upon annealing that results in a larger number of inter-chain contacts which are favored upon planarization of chain segments. We now use these trends in PL signatures as a basis for understanding changes in polymer conformations and packing upon addition of PCBM as well as the specific nature of interactions between polymer and fullerene molecules in blends.

When PCBM is added to MDMO-PPV, PL spectra show blue-shifts of the 0-0 transitions and apparent reductions in the lineshape Huang-Rhys factors. These results suggest that PCBM disables inter-chain interactions resulting in more disordered chain conformations with shorter conjugation lengths. However, as noted in the Results section, PL spectroscopy is rather limited in its ability to assess the specific nature of these PCBM-induced structural distortions due largely to lower signal-to-noise ratios. Instead we use the detailed information afforded from Raman spectroscopy that is capable of selectively investigating changes in the polymer structure over a wide range of PCBM loadings.

Comparison of Raman spectra excited with short and long excitation wavelengths reveal important changes MDMO-PPV structure upon addition of PCBM. Red-shifts and increasing relative intensities of the MDMO-PPV ~964 $cm^{-1}$ mode show that PCBM molecules interact preferentially with this backbone group which is also apparent from the invariance of other (phenyl) backbone modes to changing PCBM content. Previously, Bruevich et al. showed that addition of TNF to structurally similar MEH-PPV chains cause marked decreases of the out-of-plane vinylene C-H wag intensities along with blue-shifts of up to 7 $cm^{-1}$. These changes were also accompanied by red-shifted and broadened absorption transitions due to ground state charge transfer interactions between MEH-PPV and TNF molecules.[24, 88] These authors concluded that addition of TNF results in an increase of planarity of MEH-PPV segments arising from cofaacial interactions between MEH-PPV and TNF. Because of the forbidden nature of the out-of-plane C-H wag mode when polymer segments are planarized, it is clear that addition of PCBM causes a decrease in coplanarity between chain segments in MDMO-PPV/PCBM blends. This distortion also leads to shorter conjugation lengths consistent with blue-shifts and spectral broadening of PL spectra with increasing PCBM loading. Another, but less likely, explanation for the changes in the ~964 $cm^{-1}$ mode is a distortion from a trans to cis arrangement of the PPV backbone which would lower the effective idealized symmetry ($\sim C_{2h}$) and make this mode allowed in the new point group ($\sim C_{2v}$). However, this situation would result in drastically different Raman spectra due to more modes becoming allowed in the lower point group which is not observed.

McGehee and co-workers recently proposed that intercalation of acceptor molecules (i.e., PCBM) into MDMO-PPV alkoxy side groups causes a conformation change of the polymer that favors improved charge transport characteristics relative to pristine films. In particular, intercalation was believed to cause an elongation of the polymer conformation and increased intra-chain order (planarity) thus promoting greater inter-chain interactions. However, direct evidence for these conformation and packing changes were not available. Based on our Raman measurements, the sensitivity of the MDMO-PPV vinylene group vibrations are consistent with PCBM intercalation into the polymer side groups. This hypothesis can be further tested by applying annealing treatments to MDMO-PPV/PCBM blends and measuring Raman spectra. Because annealing promotes phase separation between polymer and fullerene components, we expect that removal of intercalated PCBM molecules from polymer side groups will partially restore intra-chain order and inter-chain packing. In this scheme, frequency and intensity changes in the ~964 cm$^{-1}$ should be suppressed in annealed films compared to those measured from as-cast films. Our measurements show that both red-shifts and intensity increases for the ~964 cm$^{-1}$ mode are substantially smaller than those observed in as-cast films excited with either 488 nm or 568 nm light. These trends suggest that while phase separation can partially restore intra-chain order and inter-chain packing in the polymer component, the overall similarity of the changes in the ~964 cm$^{-1}$ mode indicate that there is still a significant amount of a mixed phase. As shown by McGehee and co-workers, longer annealing treatments (~1 hr) should result in complete phase separation.

Although the Raman data suggest that PCBM molecules do intercalate into the polymer structure, the changes in the ~964 cm$^{-1}$ mode with PCBM loading instead demonstrate that chains are becoming more disordered and interchain interactions are suppressed. In particular, planarity between chain segments decreases as the PCBM molecules intercalate which also suppresses inter-chain interactions. The implications of these structural distortions are also apparent from the PL measurements, with blue-shifting and broadening PL spectra with increasing PCBM content. Overall, both PL and Raman trends indicate that the polymer structure in PCBM blends more closely resembles those found in dilute solutions rather than pristine films. Unfortunately, the present data do not allow us to conclude whether the polymer chains adopt elongated conformations as proposed by other groups but this would be consistent with solution-like conformations.

It is also interesting to compare changes in the C=C symmetric stretch (~1625 $cm^{-1}$) of the MDMO-PPV vinylene group with excitation wavelength. Raman spectra of both as-cast and annealed films generated with 488 nm light showed similar red-shifts and relative intensity increases for this mode while 568 nm excitation exhibited no change with varying PCBM content. One possible explanation for this effect is ground state charge transfer interactions between MDMO-PPV and PCBM that are enhanced when donors and acceptors are intimately mixed (i.e., intercalated). Bruevich et al. showed that charge transfer interactions in MEH-PPV/TNF blends result in red-shifts of the dominant ~1580 $cm^{-1}$ stretching mode of the MEH-PPV phenyl group due to face-to-face interactions between the MEH-PPV segments and TNF acceptors. Ground state charge transfer interactions manifest as weak, broadened and red-shifted optical transitions that appear on the red onset of the MEH-PPV absorption transition that can be interrogated by resonance Raman spectroscopy. In contrast, optical absorption spectra of MDMO-PPV/PCBM blend films showed no new transitions and spectra appear as linear superpositions of each component (data not shown). Despite the lack of direct evidence of these transitions in optical absorption spectra, it is possible that they may be masked by more strongly allowed π-π* transitions. In this case, we expect that Raman spectra generated with longer wavelength excitation (i.e, 568 nm) to exhibit a greater sensitivity to PCBM loading which is not observed. Alternatively, ground state charge transfer transitions may be shifted to higher energies due to the different nature of interactions between donor and acceptor. It is possible that the intensity increases and red-shifts of the C=C vinylene stretch when excited with higher energy photons reflect a ground state charge transfer interaction. However, further investigations are needed to help sort out whether ground state charge transfer interactions between PCBM and the vinylene linkage of MDMO-PPV are in fact the origins of these observed shifts.

Overall, the Raman data supports the view of an intimately mixed MDMO-PPV/PCBM phase in as-cast films where the PCBM molecules are mostly intercalated between MDMO-PPV side groups. Addition of PCBM caused blue-shifts of PL $E_{0\text{-}0}$ values and linewidth broadening that are indicative of a disruption of inter-chain interactions, shortening of conjugations lengths and increased intra-chain disorder. Raman spectra of blend films with varying PCBM loadings confirmed these trends where significant red-shifts and increasing intensities of the out-of-plane vinylene C-H mode at ~964 $cm^{-1}$ showed that intra-chain order decreases with increasing PCBM content. These PCBM-dependent changes in the polymer conformational attributes resemble conformations found in dilute solutions, namely, elongated conformations with larger intra-chain disorder. Previous Raman measurements of MDMO-PPV dilute solutions by our group in fact showed larger relative intensities and lower frequencies of the ~964 $cm^{-1}$ mode compared to spectra of thin films that are similar to the trends presented herein with varying PCBM content.[16] The origin of these structural changes is consistent with the intercalation of the PCBM molecules as proposed by McGehee and co-workers which is inferred from the sensitivity of the vinylene group vibrations with PCBM loading. Annealing of MDMO-PPV/PCBM films confirmed this hypothesis whereby removal of intercalated PCBM resulted in diminished spectral shifts of the ~964 $cm^{-1}$ mode. Using the spectroscopic results as a basis, we now consider the structural and electronic origins of charge mobility enhancements in MDMO-PPV/fullerene blends.

As noted previously, the currently accepted mechanism for improved transport is that polymer chains elongate and segments planarize that enables better inter-chain packing. In this scheme, both intra- and inter-chain charge transport would become operable, similar to charge transport characteristics of polythiophenes.[46] However, the decreasing intra-chain order and conjugation lengths determined from PL and Raman data effectively rule out planarization of segments as a source for charge mobility enhancements. Moreover, Gelinck et al. demonstrated that decreased conjugation lengths resulted in lower charge photoconductivities when polymers were subject to photo-oxidation.[97] Because inter-chain interactions are suppressed due to disorder between chain segments, π-π stacked chain-chain contacts cannot form thus making two-dimensional charge transport inoperable. Furthermore, annealing of MDMO-PPV/PCBM blend films caused reductions of charge mobility values to levels similar to those observed in pristine MDMO-PPV films.[80] Raman spectra of annealed MDMO-PPV/PCBM films showed that inter-chain interactions are partially restored (as seen from diminished red-shifts and intensity increases of the ~964 $cm^{-1}$ mode) which further rules out these structural interactions as a possible source of increased mobilities. Lastly, the proposed elongation of polymer chain conformations could not be directly confirmed by

PL and Raman spectra. However, it is reasonable that intercalation could cause an elongation of the overall conformation although intra-chain order between chain segments decreases. In this manner, the elongated chains could act as filaments that allow charges (i.e., holes) to migrate at larger distance scales before becoming trapped or recombining non-geminately.

Aside from structural considerations discussed above, charge transfer interactions may also play a role in mobility improvements upon intercalation of PCBM molecules. For example, ground state charge transfer interactions could result in improved charge mobilities owing to the intimately mixed nature of both components. Although no apparent changes in optical absorption spectra were observed it is possible that the low oscillator strengths of these transitions may cause them to be masked under more intense $\pi$-$\pi^*$ transitions. Furthermore, the sensitivity of the vinylene C=C stretch at ~1625 $cm^{-1}$ with excitation wavelengths may indicate charge transfer interactions between PCBM and this backbone group. On the other hand, it is possible that Franck-Condon factors for charge transfer along the polymer structure are more favorable upon intercalation of PCBM. Specifically, reductions in reorganization energies could result in higher mobilities but this is not possible to determine from our data.

## 4.3 Conclusions

The PL and Raman results presented here have important implications for understanding the mechanisms of charge transport in MDMO-PPV/fullerene blends. It is generally believed that fullerenes cause MDMO-PPV chains to elongate and planarize resulting in enhanced inter-chain interactions that should, intuitively, promote efficient charge transport owing to the delocalized nature of these π-π stacked structures. However, we have demonstrated that intercalation of PCBM into MDMO-PPV side groups causes a decrease in intra-chain order that inhibit inter-chain interactions as seen in intensity increases and red-shifts of the MDMO-PPV ~964 cm$^{-1}$ mode and blue-shifts of the PL $E_{0-0}$ values with increasing PCBM content. Because of the lack of both intra- and inter-chain order, only intercalation-induced elongation of the polymer chains are the only viable structural origin that could lead to increases of hole mobilities of MDMO-PPV/PCBM blend thin films. Unfortunately, this structural change could not be inferred directly from PL and Raman data. On the other hand, the excitation wavelenth-dependent red-shifts of the MDMO-PPV C=C vinylene stretch at ~1625 cm$^{-1}$ suggest that ground state charge transfer interactions may be masked under intense π-π* absorption features of the polymer and fullerene components.

# Chapter 5.

# Resonance Raman studies of excited state structural displacements of conjugated polymers in donor/acceptor charge transfer complexes

Reproduced by permission of the PCCP Owner Societies, from:

*Phys. Chem. Chem. Phys.* **2012**, 14, 11273-11276

## 5.1 Introduction

### 5.1.1 Charge Transfer Complexes

Charge transfer complexes, discussed in chapter 1 of this dissertation, are pairs of molecules weakly bound by the complete or partial transfer of an electron. If a complex is formed in the ground state, it can be described quantum mechanically as the mixture of

---

[*] This article has been edited and re-formatted to better fit into the dissertation, and some supplemental information has been added.

a neutral donor-acceptor state ($\Psi_{DA}$) and an ionized donor-acceptor state ($\Psi_{D^+ + A^-}$). This complex can be excited into a further-ionized state (with a greater amount of charge transferred) through the absorption of a photon. The transition from the charge transfer complex ground state to its excited state can be written as:

$$[c_1\Psi_{DA} + c_2\Psi_{D^+ + A^-}] \xrightarrow{h\nu} [c_2\Psi_{DA} + c_1\Psi_{D^+ + A^-}]$$

Where $\Psi_{DA}$ is the wavefunction of the donor and acceptor in the neutral state, $\Psi_{D^+ + A^-}$ is the wavefunction of the ionized donor-acceptor pair, and $c_1 > c_2$. In the ground state, the contribution of the ionized pair is small, but becomes greater in the excited state. .

As discussed above, rearrangement of electron density will change the equilibrium position of the nuclei in a molecule. If this rearrangement is caused by the emission or absorption of a photon, the identity and displacement of vibrational modes coupled to the electronic transition can be determined by analysis of resonant Raman scattering spectra. Charge transfer complex absorption corresponds to direct photo-induced injection of a partial hole/electron onto the donor/acceptor, and the resulting nuclear displacements are caused by distortion of the molecular structure to accommodate the charge. Large distortions will provide an energetic barrier to charge transfer, while small distortions will facilitate the easy movement of charge.

### 5.1.2 Conjugated Polymer/Small Molecule Charge Transfer Complexes

The study of charge transfer complexes may serve as a tool for better understanding the transport of charge within the donor and acceptor materials. As charge carriers move through highly-polarizeable materials like conjugated polymers, their associated electric field distorts the surrounding media, and the moving charge carrier must drag along a bulky polarization field.  This is somewhat like a bowling ball moving along a bed, where the heavy weight of the bowling ball distorts the soft mattress material and traps the ball within a sunken pocket.  To move the ball forward, the material in front must compress, and the material behind must relax, dissipating energy into the mattress as heat.  We know from experience that it's much easier to roll a bowling ball along a marble floor than along a feather bed, and so it is with organic electronic materials.  Quantifying the extent of this reorganization and understanding how to minimize it will be essential to engineering materials with higher charge mobility.

### 5.1.3 MDMO-PPV/Small Molecule Charge Transfer Complexes

The conjugated polymer MDMO-PPV will form ground state charge transfer complexes with a wide variety of small molecule electron acceptors.  MDMO-PPV and PCBM do not interact strongly in the ground state - the absorption spectrum of the blend is primarily a linear superposition of the spectra of the constituents.  The lack of significant charge transfer absorption might be due to poor spatial overlap between the frontier orbitals of spherical PCBM and mostly-linear conjugated polymers, and partly a result of the small offset between the HOMO of MDMO-PPV and the LUMO of PCBM.

On the other hand, the small molecule electron acceptors 2,7-Dinitro-9-fluorenone (DNF) and 2,3-Dichloro-5,6-dicyano-1,4-benzoquinone (DDQ)  show clear signs of ground-state interaction when mixed with the conjugated polymer MDMO-PPV.  In the previous chapter, studies the effect of TNF complexation on MDMO-PPV was discussed[88]. We chose DNF in this study, as TNF is classified as an explosive (cf., the popular compound TNT, or trinitrotoluene) and consequently more difficult to buy and transport.

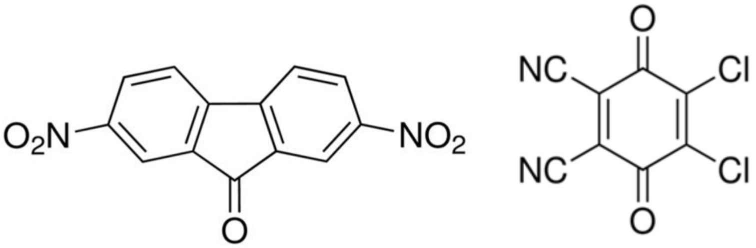

**Figure 5.1.3.1**: Left: structure of the small molecule electron acceptor 2,7-Dinitro-9-fluorenone (DNF). Right: structure of the small molecule electron acceptor 2,3-Dichloro-5,6-dicyano-1,4-benzoquinone (DDQ). The general strategy for designing these molecules seems to be "attach as many electrophilic functional groups as possible", thus the many nitro, carbonyl, cyano, and halogen additions.

The figure below shows the absorption spectrum of MDMO-PPV and an MDMO-PPV/DNF blend thin film. In an undoped MDMO-PPV film, the absorption spectrum peaks at approximately 500 nm. When 50% weight DNF is added, the absorption maximum moves to ~525nm. A 50% weight DNF/polystyrene film shows no significant absorption in this region, indicating that the new feature in the spectrum is a result of specific interactions between MDMO-PPV and DNF. However, the exact nature of the D/A interaction is not yet completely clear. In additional to the charge-transfer absorption discussed above, it may be that formation of the complex actually forces the MDMO-PPV into a more planar shape. Looking at the resonant Raman spectrum using the metric developed in chapter 4 (the relative displacement of the C-H out of plane mode) the stronger charge transfer complexes show increased donor planarity. However, there are several new vibrational modes in the spectrum so the interpretation may not be as simple. The relative contributions of planarization vs. charge transfer absorption is worth further study, as there has been much interest in using strong electron acceptors as minority doping agents to increase the efficiency of organic solar cells.

Formation of these complexes is reversible. Thermal annealing at 115°C for 30 minutes re-sets the absorption spectrum to that of the pure materials, indicating that phase segregation has occurred and the donor and acceptor have migrated away from each other to form relatively pure domains. There is no indication that MDMO-PPV and DNF complex in solution, meaning the strength of the interaction is too weak to resist the random buffeting of solvent molecules at room temperature.

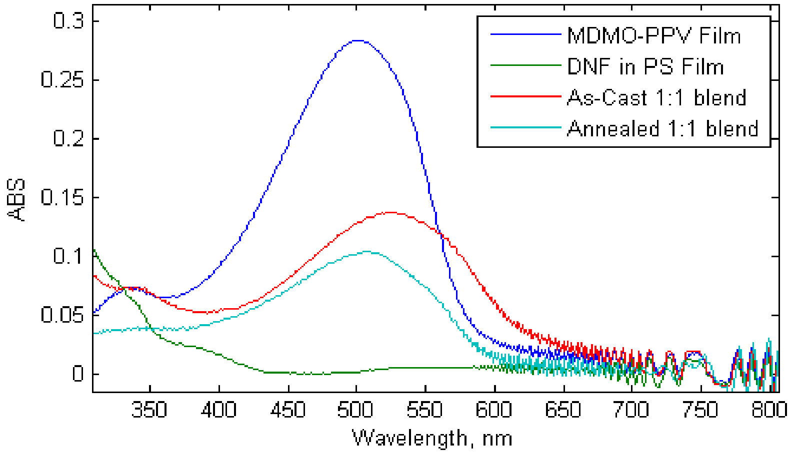

**Figure 5.1.3.2:** UV-VIS linear absorption spectra of a pure MDMO-PPV thin film on glass (dark blue), a DNF/polystyrene film (green), a 1:1 weight:weight MDMO-PPV film as cast (red) and a 1:1 weight:weight MDMO-PPV film after thermal annealing (cyan).

Charge transfer complexes at donor/acceptor heterojunction interfaces play a key role in determining the performance attributes of polymer-based solar cells,[98] including the open-circuit voltage ($V_{OC}$).[99] The magnitudes of charge transfer rate constants governing charge generation and transport processes are especially sensitive to displacements of nuclear coordinates in response to a charge transfer event at the donor/acceptor interface.[64b, 100] However, measurement of vibrational displacements by optical spectroscopy is difficult due to weak and unresolved optical lineshapes typically encountered in charge transfer systems.[101] Although recent electroluminescence, [102] NIR photoluminescence[6c] and photo-induced absorption[103] studies have shed light on CT state energies and dynamics, details of vibrational mode-specific displacements remain concealed beneath structureless lineshapes.

Resonance Raman spectroscopy can overcome these limitations in molecular D/A systems by providing a mode specific view of D/A interfacial excited state structural distortions.[104] We use this technique to study ground state CT complexes of the conjugated polymer, MDMO-PPV, and small molecule acceptor blends. These systems are excellent models for understanding how D/A structural and electronic interactions affect CT processes in solar cells, such as self-exchange reactions associated with ground state charge transport. Ground state CT complexes are obtained by blending MDMO-PPV blends with dinitrofluorenone (DNF) and dichloro-dicyano-benzoquinone (DDQ) acceptors in (~1:1 monomer/acceptor w/w). CT states appear as red-shifted (~2000 $cm^{-1}$) and broad absorption transitions and comparable in strength to the $S_0$-$S_1$ transition of pristine MDMO-PPV as shown in figure 6.2.1.1a. MDMO-PPV/DNF thin films exhibit weak CT character, consistent with previous studies of related MEH-PPV/trinitrofluorenone (TNF) blends (1:1 w/w) where the amount of charge transfer was estimated to be ~0.1$e^-$.[105] MDMO-PPV/DDQ spectra show much stronger and distinct CT character whereas blends of MDMO-PPV/[6,6]-phenyl-$C_{61}$-butyric acid methyl ester (PCBM), commonly used in solar cells, have no appreciable ground state CT transitions in absorption spectra.[106]

## 5.2 Results and Discussion

### 5.2.1 Absorption and Emission Spectra of Charge Transfer Complexes

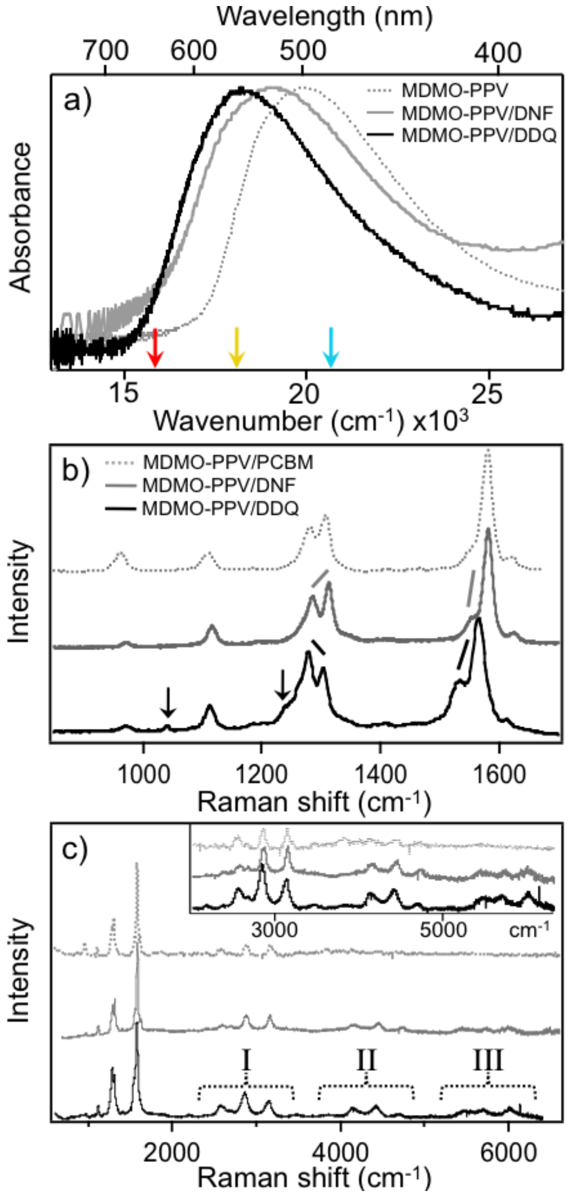

**Figure 5.2.1.1** a) UV-VIS absorption spectra of MDMO-PPV and MDMO-PPV/small molecule donor/acceptor thin films on glass. The colourful arrows indicate excitation wavelengths used (left to right: 647nm, 568m, and 488nm). b) Resonance Raman spectra of donor/acceptor thin films excited at 568mm. The black arrows indicate vibrational

modes not found in MDMO-PPV:PCBM blends. c) Raman spectra of donor/acceptor thin films excited at 488nm, showing Raman overtones to the third order.

Raman spectra generated on resonance with the CT absorption bands in Fig. 5.2.1.1a allow us to determine excited state structural distortions and the nature of D/A interactions. Figure 5.2.1.1b shows Raman spectra of MDMO-PPV/DNF and DDQ blend thin films excited with 568 nm light (17605 $cm^{-1}$). For comparison, we include Raman spectra of MDMO-PPV/PCBM blends excited under the same conditions that provide useful benchmarks for discerning CT effects in Raman spectra. Previously published normal coordinate assignments of PPV derivatives[22] and their nominal reported frequencies are used for comparing Raman spectra of CT complexes (see table below). MDMO-PPV/DNF spectra show features akin to weak CT complexes (i.e., MEH-PPV/TNF)[88] that appear, qualitatively, similar to MDMO-PPV/PCBM blends. MDMO-PPV/DDQ complexes show significant changes suggesting stronger donor/acceptor CT interactions. Both DNF and DDQ blends show marked intensity decreases and blue-shifts of the out-of-plane C-H wag of the MDMO-PPV vinylene group ($\nu_4$, ~972 $cm^{-1}$) that were previously attributed to planarization of chain segments due to face-to-face D/A interactions.[88] Conversely, MDMO-PPV/PCBM blends show larger intensities and red-shifts of this mode indicating significant torsional distortions of the polymer backbone.[11] Red-shifts of the MDMO-PPV phenyl ring symmetric stretching mode ($\nu_{14}$, ~1578 $cm^{-1}$) are also observed, the extent of which depending on the apparent CT interaction strength. For example, MDMO-PPV/DNF complexes show relatively small red-shifts (<3 $cm^{-1}$) compared to PCBM blends reflecting its weaker CT character. On the other hand, MDMO-PPV/DDQ exhibit substantial red-shifts of up to ~10 $cm^{-1}$ which are accompanied by increasing relative intensity of the ~1545 $cm^{-1}$ mode ($\nu_{13}$), red-shifts and changes in the intensity distributions of the ~1280 $cm^{-1}$ ($\nu_9$) and ~1310 $cm^{-1}$ ($\nu_{10}$) bands as well as increased intensities of the ~600 ($\nu_2$), 1044 ($\nu_5$) and 1245 ($\nu_8$) $cm^{-1}$ bands that also appear in IR spectra (see Supporting Information). Together with absorption spectra, trends in the Raman data are consistent with CT complex association in MDMO-PPV/DNF (weak) and DDQ (strong) blends.[107]

### 5.2.2 Quantifying Displacements

We now quantify the excited state structural displacements of CT complexes which are expected to vary depending on the interaction strength and D/A orientations. Figure 5.2.1.1c shows resonance Raman spectra excited with 488 nm (20492 $cm^{-1}$) light and the most noteworthy feature of these spectra is the appearance of long and detailed progressions of overtone and combination bands (labelled I-III). Similar features are observed in spectra excited with 568 nm and 647 nm light but the spectral range is limited by etaloning effects of the CCD detector at longer wavelengths (see Supporting Information). Intensity distributions within each cluster are in fact sensitive to the CT character that reveal intricate details of the D/A interface structure in addition to electronic interactions. The fact that overtone-combination bands appear in the Raman spectra of these polymer CT complexes is surprising and, to our knowledge, have never been reported before in PPV systems. C-H stretches of the MDMO-PPV alkoxy side groups ~2900-3000 $cm^{-1}$ are the only fundamentals in this region[12] as observed in IR spectra (see Supporting Information). However, these transitions are not discernible in the resonance Raman data of figures 6.2.1.1b and 6.2.1.1c demonstrating that only modes displaced in the CT transition are resonantly enhanced. By comparison, MDMO-PPV/PCBM blends have much lower overtone-combination intensities which is consistent with negligible ground state CT interactions.

## Table 5.2.2.1

Raman frequencies ($\hbar\omega_k$) and displacements ($\Delta_k$) of MDMO-PPV/DDQ and DNF complexes.

| | DDQ | | | DNF | | |
|---|---|---|---|---|---|---|
| mode (k) | $\hbar\omega_k$ | $I_k / I_{k'}$ | $\Delta_k{}^a$ | $\hbar\omega_k$ | $I_k / I_{k'}$ | $\Delta_k{}^a$ |
| $\nu_1$ | 508 | 0.25 | 0.65 | - | | |
| $\nu_2$ | 602 | 0.30 | 0.25 | 602 | 0.10 | 0.15 |
| $\nu_3$ | 800 | 0.08 | 0.15 | - | | |
| $\nu_4$ | 974 | 0.13 | 0.38 | 967 | 0.03 | 0.30 |
| $\nu_5$ | 1044 | 0.08 | 0.30 | - | | |
| $\nu_6$ | 1114 | 0.23 | 0.60 | 1110 | 0.22 | 0.40 |
| $\nu_7$ | 1210 | 0.11 | 0.15 | 1187 | 0.15 | 0.20 |
| $\nu_8$ | 1245 | 0.21 | 0.35 | - | | |
| $\nu_9$ | 1280 | 0.68 | 1.02 | 1281 | 0.54 | 0.65 |
| $\nu_{10}$ | 1306 | 0.58 | 0.90 | 1309 | 0.37 | 0.72 |
| $\nu_{11}$ | - | | | 1340 | 0.08 | 0.05 |
| $\nu_{12}$ | 1410 | 0.13 | 0.20 | 1406 | 0.04 | 0.25 |
| $\nu_{13}$ | 1535 | 0.45 | 0.45 | 1548 | 0.26 | 0.40 |
| $\nu_{14}$ | 1568 | 1.00 | 0.85 | 1575 | 1.00 | 0.87 |
| $\nu_{15}$ | 1620 | 0.22 | 0.30 | 1620 | 0.05 | 0.20 |

| | | | | |
|---|---|---|---|---|
| $2\nu_6$ | 2192 | (0.5) [b] | 2190 | |
| $\nu_6+\nu_{9,10}$ | 2405 | | 2400 | |
| $2\nu_{9,10}$ | 2582 | (1.0) [b] | 2575 | (0.6) [b] |
| $\nu_6+\nu_{14}$ | 2690 | | 2690 | |
| $\nu_{9,10}+\nu_{14}$ | 2852 | | 2860 | |
| $2\nu_{14}$ | 3136 | (0.8) [b] | 3160 | (0.8) [b] |
| $2\nu_6+\nu_{9,10}$ | 3475 | | - | |
| $3\nu_{9,10}$ | 3855 | | - | |
| $2\nu_{9,10}+\nu_{14}$ | 4138 | | 4145 | |
| $2\nu_{14}+\nu_{9,10}$ | 4409 | | 4450 | |
| $3\nu_{14}$ | 4687 | | 4730 | |
| $\Gamma$ ($cm^{-1}$) | | 400 | | 550 |
| $E_{0-0}$ ($cm^{-1}$) | | 16500 | | 16950 |

[a] Generated from equations. 1-5 & 7. [b] Estimated by comparing fundamental and overtone intensities, via equation 6.

The appearance of overtones and combination bands in resonance Raman spectra of the MDMO-PPV/acceptor CT complexes can be most readily explained using the time-dependent theory of Raman spectroscopy developed by Heller, Zink and co-workers.[20] Briefly, only modes with nonzero displacements (i.e., totally symmetric) will contribute to the resonance Raman spectrum and the relative intensities reveal the slope, or, displacement of the potential minima between the ground and excited (CT) states. Displacements along high frequency vibrations result in faster wavepacket motion on the excited (CT) state surface which produces stronger overtones and combination bands.[21] Consequently, the overtone-combination features are dominated by $\nu_{9,10}$ and $\nu_{14}$ modes as shown in the inset of figure 5.2.1.1c.

Although complete excitation profiles are not available from the data in Fig. 5.2.1.1c, it is still possible to obtain estimates of $\Delta_k$ by adjusting these values until a good fit with experimental intensities is obtained. Because of the large number of displaced modes, this procedure can be simplified considerably by using Savin's approximation (equation 7) to estimate relative displacements from pairwise comparison of Raman intensities. A similar approach was employed by Beaulac et al. who calculated vibrational displacements in ruthenium(II) complexes from resonance Raman spectra.[18]

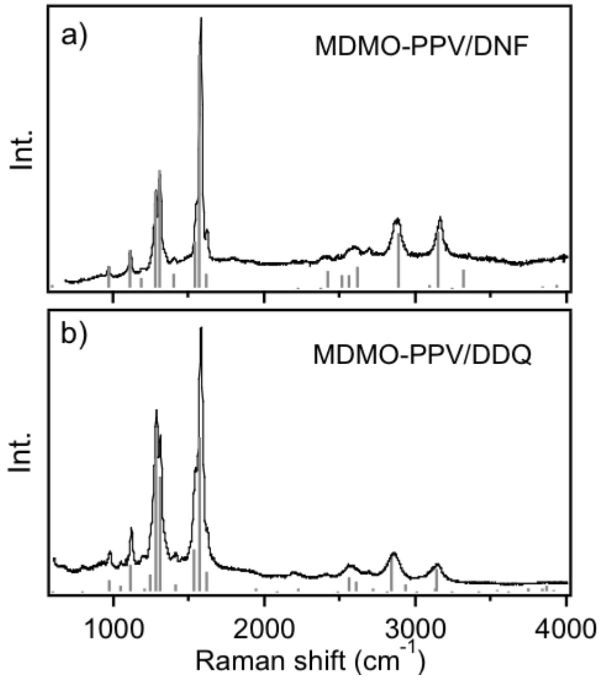

**Figure 6.2.2.1** Calculated Raman spectra of both MDMO-PPV/DNF (a) and DDQ (b) complexes

and $\Delta_k$ values are listed in the table above for each mode for the fundamental and first overtone regions. Overall, the fit spectra reproduce the experimental intensities well. As a check on the calculated $\Delta_k$ values, we use a simple procedure described in Ref. 15 that provides estimates of $\Delta_k$ from comparison of first overtone and fundamental intensities. These estimates are included in the table above (in parentheses) and are only reported for modes displaying resolved overtones. Both calculated $\Delta_k$ values and estimates are in good agreement which further supports the validity of our analysis. Although we presently cannot exclude interference effects from possible close-lying electronic states or vibrational mode mixing, which may become significant in CT complexes, we expect the impact of these effects to be small owing to the relatively small (<1) displacements. In the time-dependent picture, this means that the wavepacket would not venture far into anharmonic regions of the potential hypersurface.

Interestingly, calculated displacements are substantially larger for the $\nu_9$ mode in MDMO-PPV/DDQ complexes as seen from the larger relative intensities in both the fundamental and overtone regions. Because this mode corresponds to the inter-ring C-C phenyl stretch, we propose that preferential interactions exist between DDQ acceptors and the phenyl group of MDMO-PPV. We further speculate that the two species interact in a cofacial manner, similar to previously proposed D/A interactions in related MEH-PPV/TNF CT complexes, resulting in increased polymer backbone planarity. This proposed D/A interaction is supported by the smaller displacement in the $\nu_4$ mode observed compared to PCBM blends demonstrating greater backbone planarity in both DNF and DDQ complexes.

## 5.3 Conclusions

We have used resonance Raman spectroscopy to calculate vibrational mode-specific displacements of polymer D/A CT complexes. This analysis is facilitated by the appearance of well-resolved overtone-combination bands which are rare in this class of polymers.  Not only do these spectra allow for quantitative extraction of mode-specific displacements, they also provide a molecular view of the D/A interface structure and interactions. This aspect was most apparent from seemingly subtle, but substantial, changes in overtone-combination bands as well as fundamantal intensities.  Because CT states in conjugated polymer D/A systems[103, 108] have a large influence of the performance attributes of devices, it is especially advantageous for understanding the interdependence between D/A structural and electronic interactions.  Resonance Raman spectroscopy is therefore expected to play a bigger role in this endeavour owing to the rich information content and relative ease of experiment compared to more demanding ultrafast techniques.

# Chapter 6.

# MATLAB Code Used for Data Analysis

## 6.1 n.m

A simple but useful piece of code that serves as a good example for how to write a very basic Matlab function. I used this function constantly, as it's helpful to have an easily-accessible way to do custom normalization. This function (as you can see) is completely unintelligent and will not do any background subtracting. It just scales a vector to have 0 as its lowest value and 1 as its highest value, which is something I need to do constantly while working with data.

```
%%% A function called n found in a file called n.m



function [output] = n(input)


%%%Declare a function called 'n'.  It takes an input

%%%called 'input' and returns (outputs) a value called

%%% ...wait for it... 'output'.


input=input-min(input);

%%%subtract away the minimum value of input


input=input/max(input);

%%%divide by the maximum value of input


output=input;

%%% set output to the new value of input

%%% there's no reason I couldn't have just declared

%%% the function as 'function [input] = n(input)'

%%% but I thought that might be confusing if

%%% you're just starting out!
```

### 6.2 demonstrator.m , a simple script to demonstrate the function of n.m

```
%%% demonstrator.m, a test script to show
%%% the function of n.m and
%%% some other basic deeds in Matlab

x=-3:.01:3;
% Make a vector called x, that goes from -3 to 3
% in steps of 0.01

y=10*sin(x*3)-4;

%%make another vector y that is the sine of x

figure; %Make a new figure window
plot(x,y); %%plot x vs y
title('x vs y'); %the the graph 'x vx y';
xlabel('x'); %label the x axis 'x'
ylabel('y'); %label the y axis 'y'

figure; %Make a new figure window
plot(x,n(y)); %%plot x vs y
title('x vs y, normalized'); %the the graph 'x vx y';
```

```
xlabel('x'); %label the x axis 'x'

ylabel('y, a.u. normalized'); %label the y axis 'y'
```

Running demonstrator.m (n.m must be in the same directory, or in a director matlab knows about) produces the following output .

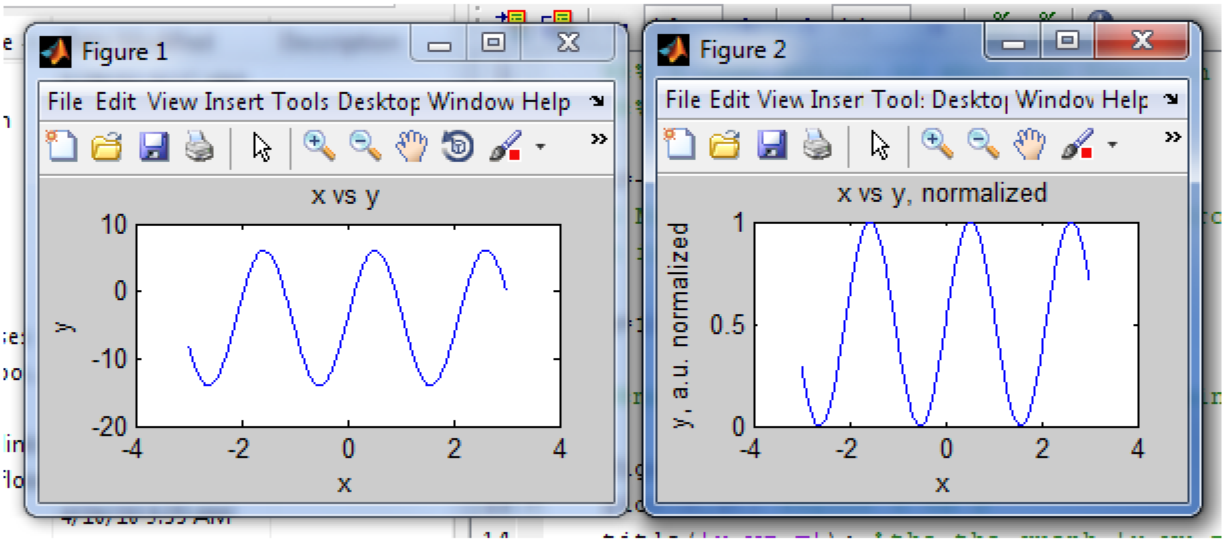

**Figure 6.2.1** Output of demonstrator.m

The output consists of two windows, the leftmost graphing the vector y as a function of the vector x. The y scale goes from -14 to +6. If y is normalized (ie n(y) rather than y), the output at right is obtained.

## 6.3 analyzer.m , a pseudo-GUI for tracking regions of interest in (2+1)D data matrices

We were interested in measuring the polarization anisotropy of single P3HT nanofibers, which requires rotating the polarization angle of the light source and watching how much the photoluminescence of the nanofibers changes as a result. This can be done in ‘wide field’ by taking a series of CCD images of a field of particles, and then tracking each particles brightness through the series of images.

To speed analysis of the data, I wrote a short matlab script that acts as a pseudo-gui for very basic analysis of the data. It allows the user to select many bounding boxes around regions of interest (i.e. regions that contain a single particle), and then follows that ROI through the stack of images. It then fits the integrated intensity as a function of polarization angle to a sine function using a least-squares optimization, and then extracts the fit parameters parameters.

```
%%% analyzer.m, a script written for analysis of

%%% polarization anisotropy data


%%%Clear variables just in case

clear swatch;  %% this is where I'll store the region of interest

clear I; %% temp variables for storing values

clear Q; %%


%%% this script presupposes an MxNxI matrix called
```

```
%%% 'Data'
%%% consisting of I images of resolution MxN.


%%% pull out the first image in the set to plot
firstimage=Data(:,:,1);



figure;  %% make a new figure window
imagesc(firstimage);  %% draw the first image
colorbar; %% add a colorbar
colormap(gray);  %% set the colormap to greyscale
caxis([2*min(firstimage(:)),10*min(firstimage(:))]);
%% set the color axis on the colorbar to low=2xbackground
%% anb high=10x background



gatherflag=1;  %% a state-machine flag to if
%%  whether you're still collecting particles
%% while collecting, =1.  When finished, =0;



particlecounter=0;  %% keeps track of how many
 %%% regions of interest you've collected
```

```
 %%% while you're selecting regions of interest,
 %%% keep adding the data to a stack
while gatherflag~=0
[x,y]=ginput(2); %% interactively pick an ROI
x=round(x); %% round the screen coords to integers
y=round(y); %% so they can be used to access the array
   if(x(1)==x(2))
      gatherflag=0;  %% if you click the same point twice, that means you're done!

   end;
   if(x(1)~=x(2))  %% if you don't, use those ROI coordinates to grab some data from the image
      particlecounter=particlecounter+1;
      rectangle('Position',[min(x),min(y),abs(x(1)-x(2)),abs(y(1)-y(2))],'EdgeColor','red')
      text(min(x),min(y),num2str(particlecounter),'Color',[1 0 0])
      swatch{particlecounter}=Data(min(y):max(y),min(x):max(x),:);  %% pull out a small sub-image

      print('-dtiff','reference.tiff')  %%save the reference image
   end;
end;
```

```
for i=1:(particlecounter); %% now loop through all othe subimges you've collected


  Q=swatch{i};

    for j=1:size(Q,3);

     Q(:,:,j)=Q(:,:,j)-min(min(Q(:,:,j)));%%subtract the min value from the subimage
(background)

      I{i}(j)=sum(sum(Q(:,:,j))); %%integrate the intesnity of the ith subimages and
store it to cell I

    end;


    %%Now to try to fit the integrated intensity as a function of

    %%polarization angle to a sine function with floating intensity,

    %%phase and frequency.


    %% the fitting function will be of the form Y=A*sin(2*CX+D)+B


    X=[0,20,40,60,80,100,120,140,160,180]; %%pre-selected polarization angles

    Y=I{i}; %% take the integrated intensity of the ith ROI and call it Y


    A=max(Y)-min(Y); %%use the range of the integrated intensity as a guess for the
amplitude of the fit function

    B=min(Y); %%use the min of the intensity as a guess for the offset of the fit
function
```

```
    C=1;  %%guess that the period is 2*PI/C, e.g. 2PI
    D=0;   %% guess the initial phase shift is 0

    fitparams(i,:)=lsqcurvefit(@sinemod,[A,B,C,D],X,Y);  %%do a least squares fit, and store the paramaters


    figure; %%open a new figure window
    plot(X,I{i},X,sinemod(fitparams(i,:),X));%% plot the fit against the data
    titlestring=horzcat('This is particle ',num2str(i),' Mod Depth: ',num2str(fitparams(i,1)/fitparams(i,2)));
    %% title the window with the name and the modulation depth
    title(titlestring);
    legend('data','fit');  %% add a legend
    print('-djpeg',horzcat('particle_',num2str(i),'.jpg'));  %%save the window as a JPEG
end;

save('fitparams.asc','fitparams','-ASCII');  %%save the fit parameters to a separate ASCII file
```

The fitting function, referred to with the function handle @sinemod, is very simple and shown below

```
function [data] = sinemod(x,xdata)


A=x(1);

B=x(2);

C=x(3);

D=x(4);

data=A*sind(C*2*xdata+D)+B
```

The data sets look like this:

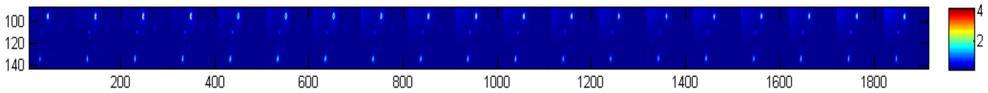

**Figure 6.3.1**.  A Stack of Polarization-Dependent Images

To process some sample data, I've chosen a sample of P3HT nanofibers formed in toluene and dispersed in polystyrene. The first 'frame' (0-degree excitation polarization) looks like this:

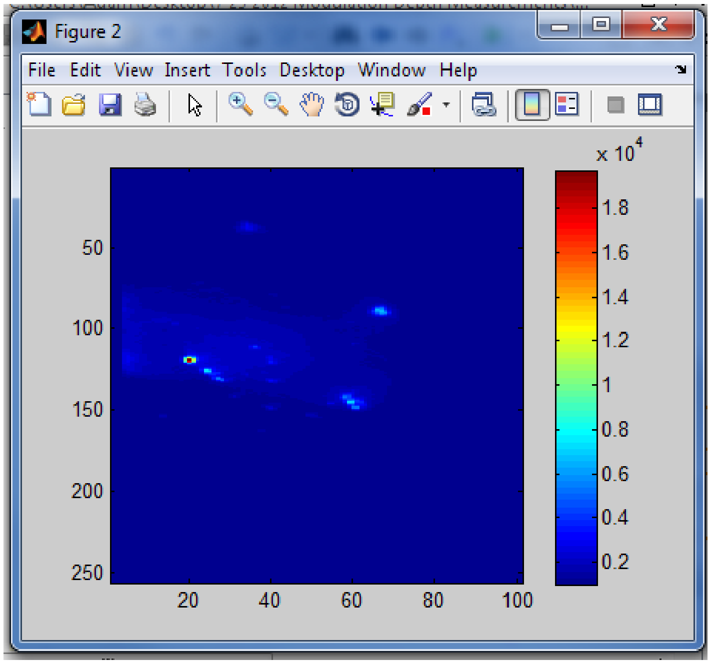

**Figure 6.3.2** The first frame of a stack of excitation polarization-dependent CCD images of P3HT nanofibers dispersed in polystyrene.

Running analyzer.m on the stack of images creates an interactive graph window that allows selection of unlimited regions of interest. Each ROI is shown by a red rectangle and small numeral that lets you keep track of the corresponding fit parameters.

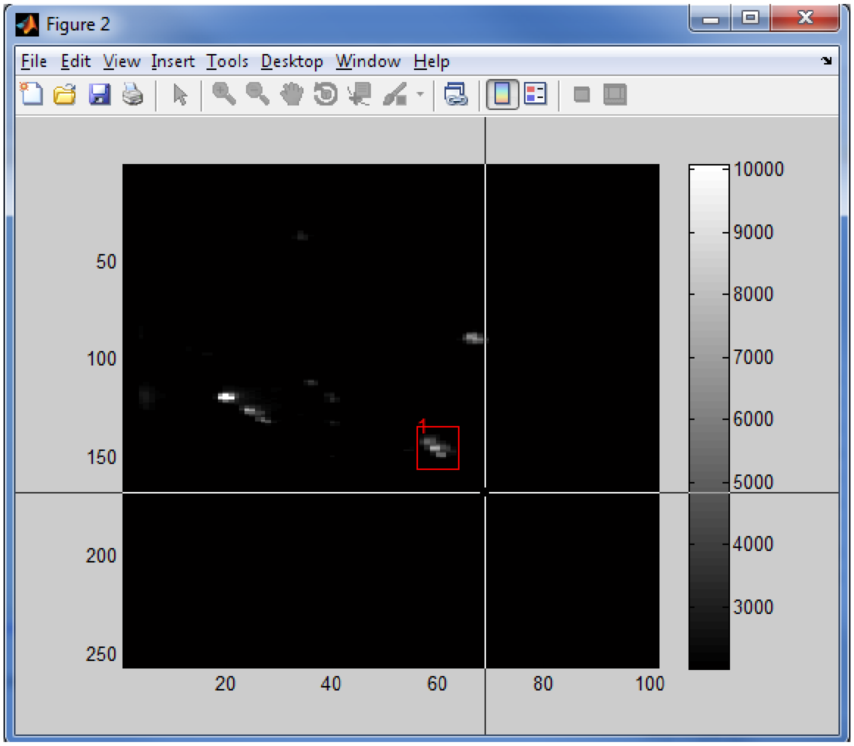

**Figure 6.3.3** The same data as Figure 3, thresholded to three times the background noise and shown in grayscale. One ROI is selected (red box).

By clicking twice, you can terminate the collection of data. The script then automatically proceeds to fitting the intensity of ROIs as a function of polarization angle. The data and automatic least-squares sine function fit are shown below.

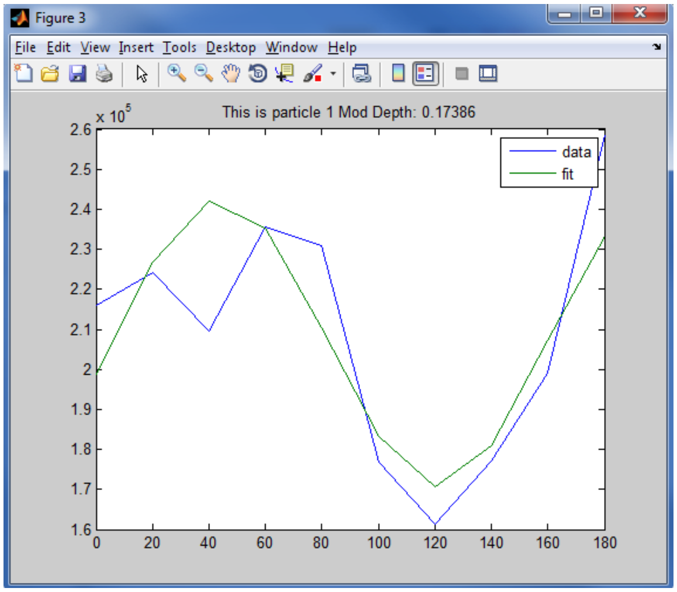

**Figure 6.3.4** least-squares sine function fit of the integrated intensity of the ROI in figure 4. Modulation depth (a measure of anisotropy of absorption with respect to the polarization of excitation light) is calculated and shown in the title, along with the index of the ROI (1).

## 6.4 RamanFit.m, a Script to Batch-Fit Multiple Modes in a Resonant Raman Spectrum

In chapter 5 of this dissertation, much is made of the frequency shift and changing relative displacement of the C-H out of plan wag mode in the resonant Raman spectrum of MDMO-PPV/PCBM blends. To quantify the effect of PCBM loading on the Raman spectra, I wrote a short script that batch-fits a stack of spectra from various blends of the two materials.

The regions around two modes of interest are selected interactively and the script steps through the stack of spectra (found in an Mx2xI matrix called ‘dataR’). A Gaussian function is fit to each mode, and the fit parameters extracted to plot trends (center frequency, integrated intensity, etc) vs. PCBM concentration. Why did I choose to fit Guassians rather than Lorentzians? Gaussians gave a very nice fit, probably because the line broadening is mostly due to chemical heterogeneity. I think a Voight function would be more correct, but the fit was pretty good so I avoided the added complexity.

```
 %% RamanFit.m , a script for batch-fitting multiple peaks

%%Set figures to default to pop-in. not really needed, but helps with

%%window clutter

set(0,'DefaultFigureWindowStyle','docked')




%% clear variables

clear err;

clear Mode;

clear Center;


%% set options to use with least squares fitting

O = optimset('tolX',10^-15,'TolFun',10^-20);
```

```
%% Load data to process; the script will operate on the contents of dataR

dataR=AC_RAMAN_488;


H=figure;  %%make a new figure window and plot the first spectrum in it

plot(AC_RAMAN_488(:,2,1));


%% interactively get the bounds of the two modes to fit

[X,Y]=ginput(4);


close(H); %% close this figure, it's not needed.


%%Loop through the contents of dataR and do the fits

for i=1:(size(dataR,3))

z(:,1)=dataR(:,1,i);

z(:,2)=dataR(:,2,i);


z(:,2)=z(:,2)-min(z(:,2));

Zmax=max(z(:,2));

z(:,2)=z(:,2)/Zmax;


% Below are specified range (in pixels) over which to fit particular modes
```

```
%%B is the C-H out of plane mode
b=X(1):X(2);
b=round(b);

%%E is the sym. carbon stretch
e=X(3):X(4);
e=round(e);
%%Do the actual least squares fitting.

fitz2=lsqcurvefit(@G,[.083,30,length(b)/2,.069,.0004],1:length(b),(z(b,2))',[0.02,20,0,0.0
1,-.01],[1,40,length(b),1,.01],O);
fitz5=lsqcurvefit(@G,[1,30,length(e)/2,.1,fitz2(5)],1:length(e),(z(e,2))',[0.02,20,0,0.01,-
.01],[1.5,40,length(e),1,.01],O);

%%Plot the results
figure;
plot(1:1600,(z(:,2)),(b(1)-100):(b(length(b))+100),G(fitz2,-
100:(length(b)+99)),1:1600,(z(:,2)),(e(1)-100):(e(length(e))+100),G(fitz5,-
100:(length(e)+99)),'x-');
err(:,i)=( sum( abs((z(e,2))-G(fitz5,1:length(e))') )) / ( sum( abs((z(e,2)))));
%%ratio=fitz(1)./fitz2(1)
```

```
%%set the linear offset background to 0, so it won't affect the

%%integration


fitz2(4)=0;

fitz2(5)=0;


fitz5(4)=0;

fitz5(5)=0;


%%Sum the fits to get a total integrated area


%Mode(i,1)=sum(G(fitz,1:1600));

Mode(i,2)=sum(G(fitz2,1:1600));

%Mode(i,3)=sum(G(fitz3,1:1600));

%Mode(i,4)=sum(G(fitz4,1:1600));

Mode(i,5)=sum(G(fitz5,1:1600));

%Center(i,1)=(10^7/488)-(10^7/(z((floor(fitz(3))+a(1)),1)+0.8));

Center(i,2)=(10^7/488.0)-(10^7/(interp1(1:1600,dataR(:,1),fitz2(3)+b(1))+.8));

%Center(i,3)=(10^7/488)-(10^7/(z((floor(fitz3(3))+c(1)),1)+0.8));

%Center(i,4)=(10^7/488)-(10^7/(z((floor(fitz4(3))+d(1)),1)+0.8));

Center(i,5)=(10^7/488.0)-(10^7/(interp1(1:1600,dataR(:,1),fitz5(3)+e(1))+.8));

%%center=z((floor(fitz(3))+a(1)),1)

i
```

```
end;

clear x;

%%Define PCBM concentration for plotting
x=[0.89,0.80,0.67,0.5,0.33,0.09,0.02];

%%Plot figures of interest

figure;plot(x,Center(:,2),'LineWidth',2,'Color','Black');
title('C-H Center Frequency (cm-1)');
xlabel('Frequency cm-1')

figure;plot(x,Mode(:,2)./Mode(:,5),'LineWidth',2,'Color','Black');
title('C-H/C-C Intensity Ratio');
xlabel('Weight Fraction PCBM');
```

The fitting function, called above by the handle @G, is found below:

```
%%%% G.m, a Gaussian esque fitting function

function G = G(x,xdata)
```

```
a=x(1); %% amplitude
g=x(2); %% width
Xo=x(3); %% center of distribution
offset=x(4); %% DC-offset
slope=x(5); %% slope of linear background

G = (g)./(3.14*(xdata-Xo).^2+g^2); %% make a Gaussian-esque function
G=G/max(G); %% cheat and normalize it
G=G*a; %% scale by the peak height I want
G=G+(slope.*xdata)+offset; %% add the background terms
```

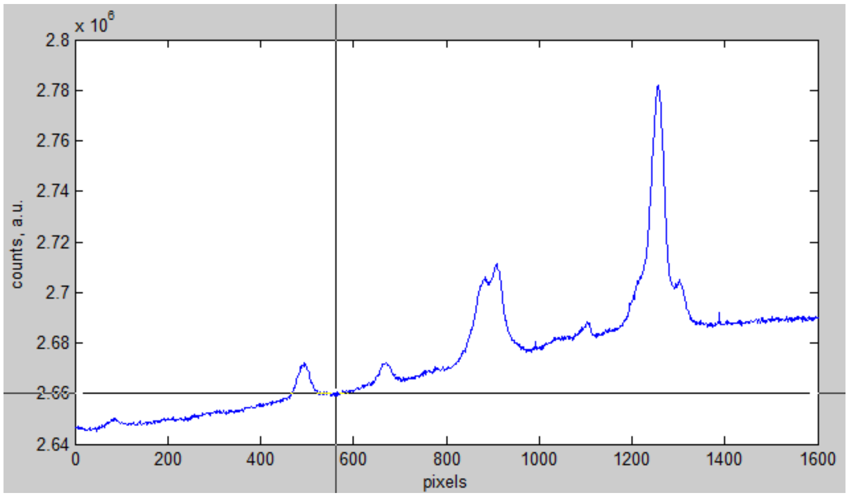

**Figure 6.4.1** Interactively selecting fitting bounds.

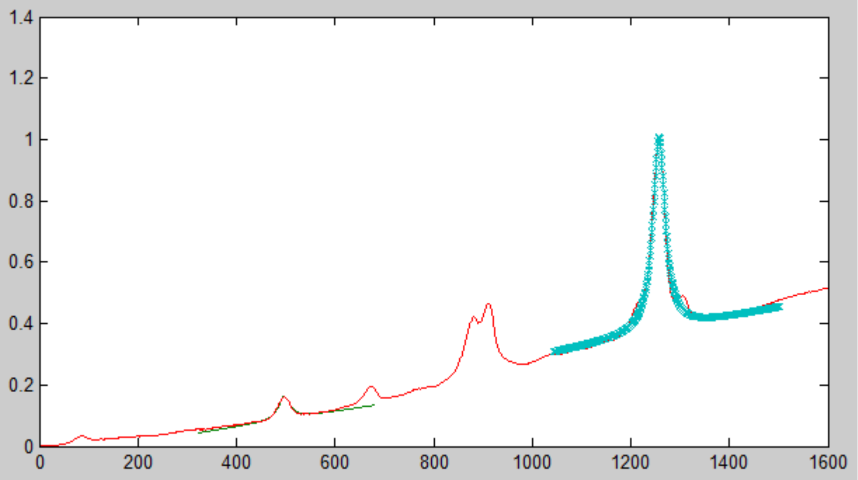

**Figure 6.4.2** Output of RamanFit.m, showing the results of least squares fitting of Gaussian functions.

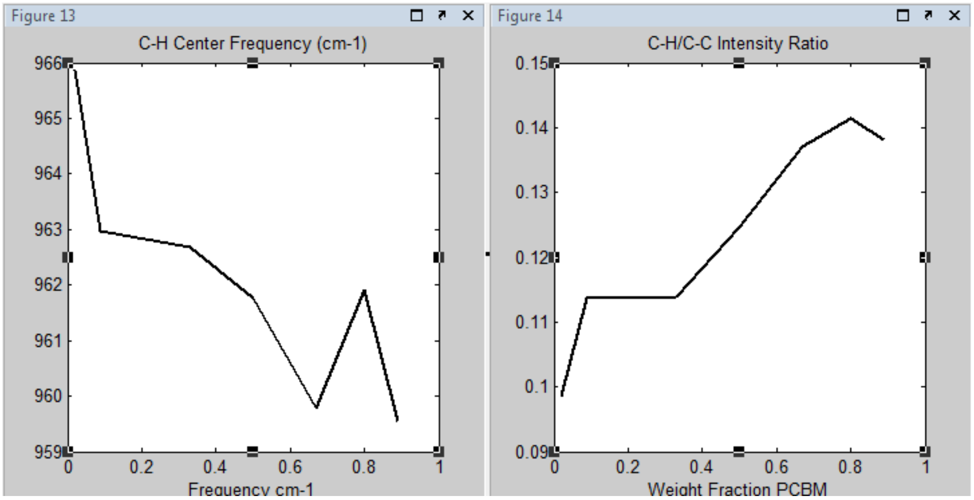

**Figure 6.4.3** Output of RamanFit.m, showing the effect of PCBM loading on the parameters generated by least squares fitting of Gaussian functions.

## 6.5 Fitting Photoluminescence Transients

TCSPC measurements can give you PL transients that are difficult to directly interpret, as there are potentially several emitters with similar lifetimes, stretched decays, etc. I have written a short and not-at-all optimized script that can fit a PL transient with a multi-exponential decay. More intense techniques are needed for situations where simple exponentials cannot accurately describe the photo-physics involved. For example, in P3HT, it seems that excited state relaxation effects the structure of the molecules in such a way as to change the electronic coupling within molecular aggregates as a function of time. This means that the radiative rate changes over the course of the relaxtion, which will be difficult to fit with a small number of exponentials, i.e. the two or three used below. However, this methods is sufficient most of the time and could be adapted by changing the fitting function to something else if need be.

First, I have written a short script to describe the core of the program, a method for convoluting two signals using a Fourier transforms, i.e. doing the convolution in the frequency domain. The reason we need to do fancy fitting here is that the TCSPC instrumentation distorts the true signal (which we can't measure) and gives us some altered signal (which we can measure). This distortion is called the 'Instrument Response Function', and is defined by the signal you would get out of the system if you could reliably put a delta function in. We can approximate a delta function input by looking at the Rayleigh-scattered light from the pulse laser, which has a pulse-width <1 picosecond. What we get out looks nothing like a delta function, but is a good approximation of the instrument's IRF. The method of convolution is shown in a short script below, and may explain what I mean more succinctly.

### 6.5.1 click_test.m

```
%%%    click_test.m , a demonstration of how to do FFT convolution
%%%
%%%make a variable to hold a progression of
%%%delta functions.  I know they're not *real*
%%%delta functions but they're as close as I can get
click=zeros(4096,1);

%%%now step through and populate it with 'clicks'
%%%of various heights
for i=1:200:4096
    click(i)=i;
end;

%%%make an x-axis, not necessary but saves time
x=1:4096;

%%rotate it to be the same size as 'click'
x=x';
```

```
%%now make a vector that's an exponential decay

y=exp(-0.05*x);




%%%First, plot the exponential decay

figure;

plot(x,y);

title('decay');




%%%second, plot the 'clicks'

figure;

plot(x,click);

title('delta functions')


%%%third, plot the convolution of the clicks and

%%%the decay.

figure;

plot(ifft(fft(click).*fft(y)),'x-');

title('convolution of delta functions and decay')
```

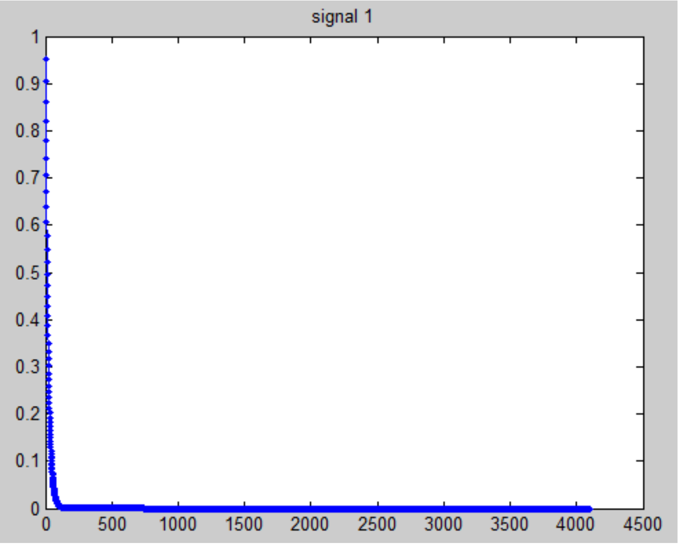

**Figure 7.5.1.1** Signal 1, an exponential decay

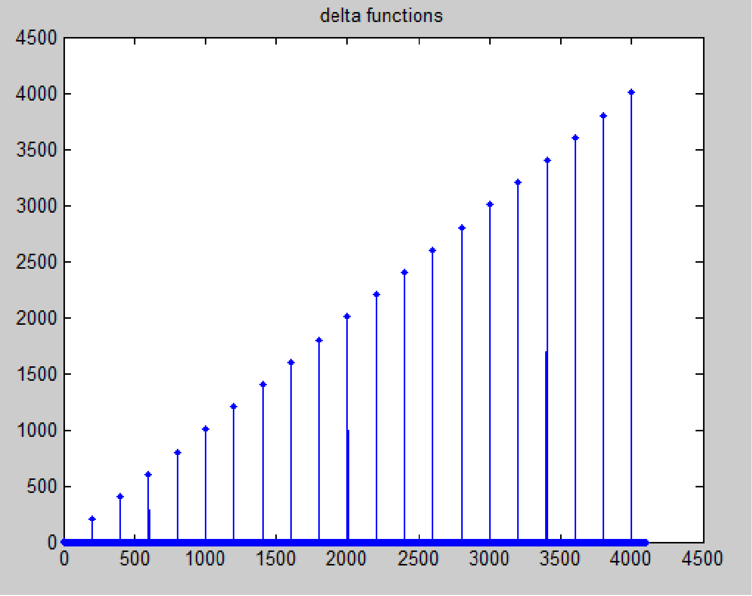

**Figure 6.5.1.2**: Signal 2, a series of pseudo-delta functions

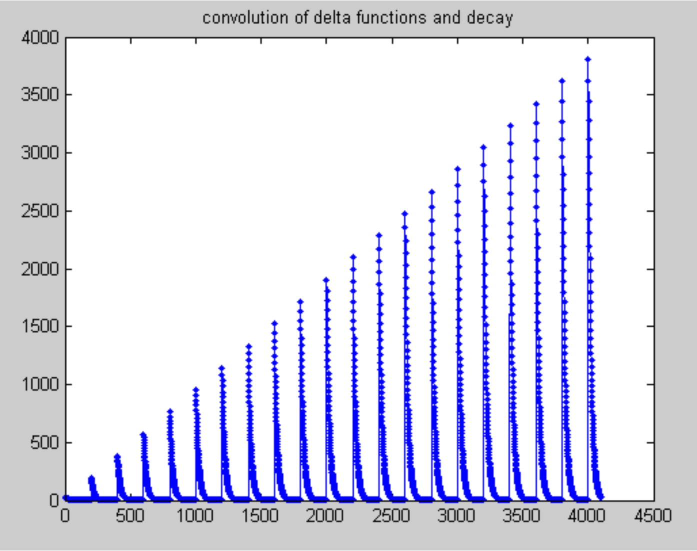

**Figure 6.5.1.2**: The frequency-domain convolution of the two signals.

The essence of this fitting routine is 1) make a sum of several exponential decays, 2) convolute the sum of exponentials with the measured IRF, 3) evaluate the fit and then 4) iterate the parameters until the error is minimized or the number of iterations exceeds some pre-set value.

### 6.5.2 deconvolution_script.m , a script for fitting TCSPC lifetime data

The actual fitting script is shown below.

```
%%%deconvolution_script.m , a script for fitting

%%%TCSPC lifetime data




clear s a IRF DATA;

%%clear old variables just in case
```

```
time=25;
numbins=4096;
bintime=time/numbins;
%%variable to define time per bin of measurement

global IRF;
global DATA;
%%make IRF and DATA global variables so sub-functions within this script can access
%%it.  Otherwise, they won't know what the IRF is and will crash.

%%%%%%%% open dialogue box to get IRF
[FileName,PathName] = uigetfile('*.asc','Select IRF');

%%%%%%%% import the data from the IRF
%%%% importdata rather than load must be used because
%%%% the asc files generated by the TCSPC software
%%%% have headers with a bunch of text

IRF=importdata(cat(2,PathName,FileName),' ',10);
IRF=IRF.data;
IRF=IRF-min(IRF);
IRF=IRF/max(IRF);
```

```
%%%%%%%% Likewise with the TCSPC data file
[FileName, PathName, filterindex] = uigetfile( ...
{  '*.asc','ASCII (*.asc)'; ...
   '*.*',  'All Files (*.*)'}, ...
  'Select data file(s)', ...
  'MultiSelect', 'on');

%%determine whether one or several spectra have been selected
for Q=1:length(FileName)

if(iscell(FileName)==1)
DATA=importdata(horzcat(PathName,FileName{Q}),' ',10);
end

%%load selected file into DATA

if(iscell(FileName)==0)
DATA=importdata(horzcat(PathName,FileName),' ',10);
Q=length(FileName);
end

%%normalize loaded data
DATA=DATA.data;
```

```
DATA=DATA-min(DATA);
DATA=DATA/max(DATA);

%%%%%%Open a new figure to plot into
figure;

%%%%%Generate a time axis from starting variables
t=linspace(0,time,numbins)';




%%%%%% Set fitting options
O = optimset('tolX',10^-24,'TolFun',10^-20,'MaxFunEvals',10^8,'MaxIter',10^3);



%%%%set bounds for fitting parameters
%%%%amplitudes

%%% the format is MINimum, INITial guess,and MAXimum
%%% the intensity is also scaled, so amplitudes
%%% are relative to each other
```

```
a1min=1;
a1init=2;
a1max=10;

a2min=1;
a2init=2;
a2max=10;

a3min=0;
a3init=10^-5;
a3max=10^-4;

%%%%%
%%%%%Lifetimes, in bins
%%%%%the lifetime in time is bins*bintime

t1min=7.99;
t1init=8;
t1max=8.01;

t2min=81.99;
t2init=82;
t2max=82.01;
```

```
t3min=8;
t3init=162;
t3max=163;

%%%%%%  Do the actual least squares fitting
fits=lsqcurvefit(@convdecay,[a1init,a2init,a3init,t1init,t2init,t3init],1:4096,DATA,[a1min,a2min,a3min,t1min,t2min,t3min],[a1max,a2max,a3max,t1max,t2max,t3max],O);
%%%%%%%%



%%%%%Makes some sub-plots to display data and
%%%%% fit in the figure the figure
position_rectangle2 = [.035, .035, .9, .4];
axes('Position',position_rectangle2);
semilogy(t,(convdecay(fits,1:4096))/max((convdecay(fits,1:4096))),'.',t,DATA,t,IRF);
xlim([-5,10]);
ylim([10^-4,1.2]);
title('FIT log plot');
legend('FIT','DATA','IRF')

position_rectangle2 = [.035, .5, .9, .4];
```

```
axes('Position',position_rectangle2);

plot(t,(convdecay(fits,1:4096))/max((convdecay(fits,1:4096))),'x',t,DATA,t,IRF);

xlim([-5,10]);

ylim([10^-4,1.2]);

title('linear data/fit plot')

legend('FIT','DATA','IRF')



%%%%%%print out the fitting parameters

ret=sprintf('\n');

space='    ';



htb = annotation('textbox', [.05 .035 .4 .4]);

s=100/(fits(1)*fits(4)+fits(2)*fits(5)+fits(3)*fits(6));

set(htb,'String',cat(2,FileName{Q},ret,'FIT PARAMETERS',ret,'COUNTS:

',ret,num2str(s*fits(1)*fits(4)),ret,num2str(s*fits(2)*fits(5)),ret,num2str(s*fits(3)*fits(6)),

ret,'Lifetime (ns):

',ret,num2str(fits(4)*bintime),ret,num2str(fits(5)*bintime),ret,num2str(fits(6)*bintime)));

print(horzcat(FileName{Q},'.tiff'),'-dtiff')

end
```

### 6.5.3 convol.m , a function for FFT convolution of signals

Convol.m, an FFT convolution function analogous to the one shown in 6.5.1, is shown below.

```
%%% convol.m, an fft convolution function


function [ data ] = convol( IRF,data )


size(IRF);

size(data);

data=ifft(fft(IRF).*fft(data));

data=data/max(data);


end
```

### 6.5.4 decay3.m, a 3-exponential decay function

Decay3.m is called in the above script, and is the actual fitting function called for the least-squares routine. It can accept parameters for up to three exponential decays, although this can be effectively reduced by setting the amplitude of unwanted exponentials low compared to the useful exponential amplitudes. E.g., set the first amplitude min to 1, while the unwanted decays can be set to $10^{-4}$ or similar. These particular scripts could use a lot of optimization but my initial goal was to get it done quickly with transparent results I could be confident in.  It would also benefit by adding a GUIDE gui.

```
%decay3, a 3-exponential decay function


function [ data ] = decay3( xdata,x )


% x(1)-> amplitude of first decay
% x(2)-> amplitude of second decay
% x(3)-> amplitude of third decay
% x(4)-> lifetime of first decay
% x(5)-> lifetime of second decay
% x(6)-> lifetime of third decay
data= (x(1)*exp(-xdata/x(4))) + (x(2)*exp(-xdata/x(5))) + (x(3)*exp(-xdata/x(6)));


data=data';


end
```

# References

1. Gregg, B. A., Excitonic Solar Cells. *J. Phys. Chem. B* **2003,** *107* (20), 4688-4698.

2. Park, S. H.; Roy, A.; Beaupre, S.; Cho, S.; Coates, N.; Moon, J. S.; Moses, D.; Leclerc, M.; Lee, K.; Heeger, A. J., Bulk heterojunction solar cells with internal quantum efficiency approaching 100%. *Nat Photon* **2009,** *3* (5), 297-302.

3. Coakley, K. M.; McGehee, M. D., Conjugated Polymer Photovoltaic Cells. *Chem. Mater.* **2004,** *16* (23), 4533-4542.

4. Greenham, N. C.; Moratti, S. C.; Bradley, D. D. C.; Friend, R. H.; Holmes, A. B., Efficient light-emitting diodes based on polymers with high electron affinities. *Nature* **1993,** *365* (6447), 628-630.

5. Friend, R. H.; Gymer, R. W.; Holmes, A. B.; Burroughes, J. H.; Marks, R. N.; Taliani, C.; Bradley, D. D. C.; Santos, D. A. D.; Bredas, J. L.; Logdlund, M.; Salaneck, W. R., Electroluminescence in conjugated polymers. *Nature* **1999,** *397* (6715), 121-128.

6. (a) Chen, D.; Nakahara, A.; Wei, D.; Nordlund, D.; Russell, T. P., P3HT/PCBM Bulk Heterojunction Organic Photovoltaics: Correlating Efficiency and Morphology. *Nano Letters 11* (2), 561-567; (b) Gao, Y.; Grey, J. K., Resonance Chemical Imaging of Polythiophene/Fullerene Photovoltaic Thin Films: Mapping Morphology-Dependent Aggregated and Unaggregated C=C Species. *Journal of the American Chemical Society* **2009,** *131* (28), 9654-9662; (c) Hallermann, M.; Kriegel, I.; Da Como, E.; Berger, J. M.; von Hauff, E.; Feldmann, J., Charge Transfer Excitons in Polymer/Fullerene Blends: The Role of Morphology and Polymer Chain Conformation. *Advanced Functional Materials* **2009,** *19* (22), 3662-3668; (d) Yang, X.; Loos, J., Toward High-Performance Polymer Solar Cells: The Importance of Morphology Control. *Macromolecules* **2007,** *40* (5), 1353-1362.

7. Gao, Y.; Martin, T. P.; Niles, E. T.; Wise, A. J.; Thomas, A. K.; Grey, J. K., Understanding Morphology-Dependent Polymer Aggregation Properties and Photocurrent Generation in Polythiophene/Fullerene Solar Cells of Variable Compositions. *The Journal of Physical Chemistry C* **2010,** *114* (35), 15121-15128.

8. Gruhn, N. E.; da Silva Filho, D. A.; Bill, T. G.; Malagoli, M.; Coropceanu, V.; Kahn, A.; Brédas, J.-L., The Vibrational Reorganization Energy in Pentacene: Molecular Influences on Charge Transport. *Journal of the American Chemical Society* **2002,** *124* (27), 7918-7919.

9. Kelley, A. M., Resonance Raman Intensity Analysis of Vibrational and Solvent Reorganization in Photoinduced Charge Transfer. *The Journal of Physical Chemistry A* **1999,** *103* (35), 6891-6903.

10. Hagler, T. W.; Pakbaz, K.; Voss, K. F.; Heeger, A. J., Enhanced order and electronic delocalization in conjugated polymers oriented by gel processing in polyethylene. *Physical Review B: Condensed Matter and Materials Physics* **1991,** *44* (16), 8652-66.

11. Barbara, P. F.; Gesquiere, A. J.; Park, S.-J.; Lee, Y. J., Single-molecule spectroscopy of conjugated polymers. *Accounts of Chemical Research* **2005,** *38* (7), 602-610.

12. Yu, Z.; Barbara, P. F., Low-Temperature Single-Molecule Spectroscopy of MEH-PPV Conjugated Polymer Molecules. *The Journal of Physical Chemistry B* **2004,** *108* (31), 11321-11326.

13. Gierschner, J.; Mack, H.-G.; Luer, L.; Oelkrug, D., Fluorescence and absorption spectra of oligophenylenevinylenes: Vibronic coupling, band shapes, and solvatochromism. *Journal of Chemical Physics* **2002,** *116* (19), 8596-8609.

14. Tutt, L.; Zink, J. I., Calculation of the electronic spectra and excited-state distortions of W(CO)5(N-donor) from preresonance Raman intensities. *Journal of the American Chemical Society* **1986,** *108* (19), 5830-5836.

15. Wu, C. C.; Ehrenfreund, E.; Gutierrez, J. J.; Ferraris, J. P.; Vardeny, Z. V., Apparent vibrational side bands in pi-conjugated systems: The case of distyrylbenzene. *Physical Review B: Condensed Matter and Materials Physics* **2005,** *71* (8), 081201/1-081201/4.

16. Wise, A. J.; Martin, T. P.; Gao, J.; Van Der Geest, K.; Grey, J. K., Observation of the missing mode effect in a poly-phenylenevinylene derivative: Effect of solvent, chain packing, and composition. *Journal of Chemical Physics* **2010,** *133,* 174901-174910.

17. Heller, E. J., The semiclassical way to molecular spectroscopy. *Accounts of Chemical Research* **1981,** *14* (12), 368-375.

18. Wise, A. J.; Grey, J. K., Resonance Raman studies of excited state structural displacements of conjugated polymers in donor/acceptor charge transfer complexes. *Physical Chemistry Chemical Physics* **2012,** *14* (32), 11273-11276.

19. Heller, E. J.; Sundberg, R.; Tannor, D., Simple aspects of Raman scattering. *The Journal of Physical Chemistry* **1982,** *86* (10), 1822-1833.

20. Tannor, D. J.; Heller, E. J., Polyatomic Raman scattering for general harmonic potentials. *J. Chem. Phys.* **1982,** *77* (1), 202-18.

21. Zink, J. I.; Shin, K. S. K., Molecular distortions in excited electronic states determined from electronic and resonance Raman spectroscopy. *Advances in Photochemistry* **1991,** *16*, 119-214.

22. Sakamoto, A.; Furukawa, Y.; Tasumi, M., Infrared and Raman studies of poly(p-phenylenevinylene) and its model compounds. *J. Phys. Chem.* **1992,** *96* (3), 1490-4.

23. Grozema, F. C.; van Duijnen, P. T.; Berlin, Y. A.; Ratner, M. A.; Siebbeles, L. D. A., Intramolecular Charge Transport along Isolated Chains of Conjugated Polymers: Effect of Torsional Disorder and Polymerization Defects. *The Journal of Physical Chemistry B* **2002,** *106* (32), 7791-7795.

24. Bruevich, V. V.; Makhmutov, T. S.; Elizarov, S. G.; Nechvolodova, E. M.; Paraschuk, D. Y., Ground state of pi-conjugated polymer chains forming an intermolecular charge-transfer

complex as probed by Raman spectroscopy. *Journal of Experimental and Theoretical Physics* **2007,** *105* (3), 469-478.

25. Wise, A. J.; Precit, M. R.; Papp, A. M.; Grey, J. K., Effect of Fullerene Intercalation on the Conformation and Packing of Poly-(2-methoxy-5-(3′-7′-dimethyloctyloxy)-1,4-phenylenevinylene). *ACS Applied Materials & Interfaces* **2011,** *3* (8), 3011-3019.

26. Myers, A. B., Resonance Raman Intensities and Charge-Transfer Reorganization Energies. *Chemical reviews* **1996,** *96* (3), 911-926.

27. Deschler, F.; Da Como, E.; Limmer, T.; Tautz, R.; Godde, T.; Bayer, M.; von Hauff, E.; Yilmaz, S.; Allard, S.; Scherf, U.; Feldmann, J., Reduced Charge Transfer Exciton Recombination in Organic Semiconductor Heterojunctions by Molecular Doping. *Physical Review Letters* **2011,** *107* (12), 127402.

28. Veysel Tunc, A.; De Sio, A.; Riedel, D.; Deschler, F.; Da Como, E.; Parisi, J.; von Hauff, E., Molecular doping of low-bandgap-polymer:fullerene solar cells: Effects on transport and solar cells. *Organic Electronics* **2012,** *13* (2), 290-296.

29. Beaulac, R.; Lever, A. B. P.; Reber, C., Resonance Raman Spectroscopy with Overtones Involving Metal-Ligand and Ligand-Centered Modes in (o-Benzoquinonediimine)ruthenium(II) Complexes. *European Journal of Inorganic Chemistry* **2007,** *2007* (1), 48-52.

30. Bredas, J.-L.; Norton, J.; Cornil, J.; Coropceanu, V., Molecular Understanding of Organic Solar Cells: The Challenges. *Accounts of Chemical Research* **2009,** *42* (11), 1691-1699.

31. Geng, H.; Niu, Y.; Peng, Q.; Shuai, Z.; Coropceanu, V.; Bredas, J.-L., Theoretical study of substitution effects on molecular reorganization energy in organic semiconductors. *The Journal of Chemical Physics* **2011,** *135* (10), 104703-7.

32. Anctil, A.; Babbitt, C.; Landi, B.; Raffaelle, R. P. In *Life-cycle assessment of organic solar cell technologies*, Photovoltaic Specialists Conference (PVSC), 2010 35th IEEE, 20-25 June 2010; 2010; pp 000742-000747.

33. Shockley, W.; Queisser, H. J., Detailed balance limit of efficiency of p--n junction solar cells. *Journal Name: J. Appl. Phys.; Journal Volume: 32:3* **1961**, Medium: X; Size: Pages: 510-19.

34. Volmer, M., Die verschiedenen lichtelektrischen am Anthracen, ihre Beziehungen zueinander, zur Fluoreszenz und Dianthracenbildung. *Annalen der Physik* **1913,** *345* (5).

35. D. Kearns, M. J. C., Photovoltaic effect and photoconductivity in laminated organic systems. *Journal of Chemical Physics* **1958,** *29*.

36. Spanggaard, H.; Krebs, F. C., A brief history of the development of organic and polymeric photovoltaics. *Solar Energy Materials and Solar Cells* **2004,** *83* (2–3), 125-146.

37. Tang, C., Two-layer organic photovoltaic cell. *Applied Physics Letters* **1986,** *48* (2).

38. Halls, J. J. M.; Walsh, C. A.; Greenham, N. C.; Marseglia, E. A.; Friend, R. H.; Moratti, S. C.; Holmes, A. B., Efficient photodiodes from interpenetrating polymer networks. *Nature* **1995,** *376* (6540), 498-500.

39. G. Yu, C. Z., A.J. Heeger, Semiconducting polymer diodes: Large size, low cost photodetectors with excellent visible-ultraviolet sensitivity. *Applied Physics Letters* **1994,** *64* (25).

40. Winder, C.; Sariciftci, N. S., Low bandgap polymers for photon harvesting in bulk heterojunction solar cells. *Journal of Materials Chemistry* **2004,** *14* (7), 1077-1086.

41. Colladet, K.; Fourier, S.; Cleij, T. J.; Lutsen, L.; Gelan, J.; Vanderzande, D.; Huong Nguyen, L.; Neugebauer, H.; Sariciftci, S.; Aguirre, A.; Janssen, G.; Goovaerts, E., Low Band Gap Donor−Acceptor Conjugated Polymers toward Organic Solar Cells Applications. *Macromolecules* **2006,** *40* (1), 65-72.

42. Hadipour, A.; de Boer, B.; Blom, P. W. M., Organic Tandem and Multi-Junction Solar Cells. *Advanced Functional Materials* **2008,** *18* (2), 169-181.

43. Hertel, D.; Scherf, U.; Bässler, H., Charge Carrier Mobility in a Ladder-Type Conjugated Polymer. *Advanced Materials* **1998,** *10* (14), 1119-1122.

44. Zhou, E.; Tan, Z. a.; Yang, Y.; Huo, L.; Zou, Y.; Yang, C.; Li, Y., Synthesis, Hole Mobility, and Photovoltaic Properties of Cross-Linked Polythiophenes with Vinylene−Terthiophene−Vinylene as Conjugated Bridge. *Macromolecules* **2007,** *40* (6), 1831-1837.

45. van de Craats, A. M.; Stutzmann, N.; Bunk, O.; Nielsen, M. M.; Watson, M.; Müllen, K.; Chanzy, H. D.; Sirringhaus, H.; Friend, R. H., Meso-Epitaxial Solution-Growth of Self-Organizing Discotic Liquid-Crystalline Semiconductors. *Advanced Materials* **2003,** *15* (6), 495-499.

46. Sirringhaus, H.; Brown, P. J.; Friend, R. H.; Nielsen, M. M.; Bechgaard, K.; Langeveld-Voss, B. M. W.; Spiering, A. J. H.; Janssen, R. A. J.; Meijer, E. W.; Herwig, P.; De Leeuw, D. M., Two-dimensional charge transport in self-organized, high-mobility conjugated polymers. *Nature (London)* **1999,** *401* (6754), 685-688.

47. Tisdale, W. A.; Williams, K. J.; Timp, B. A.; Norris, D. J.; Aydil, E. S.; Zhu, X.-Y., Hot-Electron Transfer from Semiconductor Nanocrystals. *Science* **2010,** *328* (5985), 1543-1547.

48. Chen, H.-Y.; Hou, J.; Zhang, S.; Liang, Y.; Yang, G.; Yang, Y.; Yu, L.; Wu, Y.; Li, G., Polymer solar cells with enhanced open-circuit voltage and efficiency. *Nat Photon* **2009,** *3* (11), 649-653.

49. Karg, S.; Riess, W.; Dyakonov, V.; Schwoerer, M., Electrical and optical characterization of poly(phenylene-vinylene) light emitting diodes. *Synthetic Metals* **1993,** *54* (1–3), 427-433.

50. Moses, D., High quantum efficiency luminescence from a conducting polymer in solution: A novel polymer laser dye. *Applied Physics Letters*

**1992**.

51. Roehling, J. D.; Arslan, I.; Moule, A. J., Controlling microstructure in poly(3-hexylthiophene) nanofibers. *Journal of Materials Chemistry* **2012,** *22* (6), 2498-2506.

52. Niles, E. T.; Roehling, J. D.; Yamagata, H.; Wise, A. J.; Spano, F. C.; Moulé, A. J.; Grey, J. K., J-Aggregate Behavior in Poly-3-hexylthiophene Nanofibers. *The Journal of Physical Chemistry Letters* **2012,** *3* (2), 259-263.

53. Grancini, G.; Polli, D.; Fazzi, D.; Cabanillas-Gonzalez, J.; Cerullo, G.; Lanzani, G., Transient Absorption Imaging of P3HT:PCBM Photovoltaic Blend: Evidence For Interfacial Charge Transfer State. *The Journal of Physical Chemistry Letters* **2011,** *2* (9), 1099-1105.

54. Heller, E. J., The semiclassical way to molecular spectroscopy. *Acc. Chem. Res.* **1981,** *14* (12), 368-75.

55. Franck, J.; Dymond, E. G., Elementary processes of photochemical reactions. *Transactions of the Faraday Society* **1926,** *21* (February), 536-542.

56. Condon, E., A Theory of Intensity Distribution in Band Systems. *Physical Review* **1926,** *28* (6), 1182-1201.

57. Grey, J. K.; Kim, D. Y.; Norris, B. C.; Miller, W. L.; Barbara, P. F., Size dependent spectroscopic properties of conjugated polymer nanoparticles. *J. Phys. Chem. B* **2006,** *110*, 25568-25572.

58. Shriver, D. F.; Dunn, J. B. R., Backscattering geometry for Raman spectroscopy of colored materials. *Applied Spectroscopy* **1974,** *28* (4), 319-23.

59. Guenes, S.; Neugebauer, H.; Sariciftci, N. S., Conjugated Polymer-Based Organic Solar Cells. *Chem. Rev.* **2007,** *107* (4), 1324-1338.

60. Yao, Y.; Hou, J.; Xu, Z.; Li, G.; Yang, Y., Effects of solvent mixtures on the nanoscale phase separation in polymer solar cells. *Adv. Funct. Mater.* **2008,** *18* (12), 1783-1789.

61. Lee, J. K.; Ma, W. L.; Brabec, C. J.; Yuen, J.; Moon, J. S.; Kim, J. Y.; Lee, K.; Bazan, G. C.; Heeger, A. J., Processing Additives for Improved Efficiency from Bulk Heterojunction Solar Cells. *J. Am. Chem. Soc.* **2008,** *130* (11), 3619-3623.

62. Sariciftci, N. S.; Smilowitz, L.; Heeger, A. J.; Wudl, F., Photoinduced electron transfer from a conducting polymer to buckminsterfullerene. *Science (Washington, D. C., 1883-)* **1992,** *258* (5087), 1474-6.

63. (a) Huynh, W. U.; Peng, X. G.; Alivisatos, A. P., CdSe nanocrystal rods/poly(3-hexylthiophene) composite photovoltaic devices. *Advanced Materials* **1999,** *11* (11), 923-+; (b) Huynh, W. U.; Dittmer, J. J.; Alivisatos, A. P., Hybrid nanorod-polymer solar cells. *Science (Washington, D. C., 1883-)* **2002,** *295* (5564), 2425-2427.

64. (a) Schwartz, B. J., Conjugated polymers as molecular materials: How chain conformation and film morphology influence energy transfer and interchain interactions. *Annu. Rev. Phys. Chem.* **2003,** *54,* 141-172; (b) Bredas, J.-L.; Beljonne, D.; Coropceanu, V.; Cornil, J., Charge-Transfer and Energy-Transfer Processes in pi-Conjugated Oligomers and Polymers: A Molecular Picture. *Chem. Rev.* **2004,** *104* (11), 4971-5003.

65. Lupton, J. M., Single-Molecule Spectroscopy for Plastic Electronics: Materials Analysis from the Bottom-Up. *Advanced Materials (Weinheim, Germany) 22* (15), 1689-1721.

66. Baessler, H.; Schweitzer, B., Site-Selective Fluorescence Spectroscopy of Conjugated Polymers and Oligomers. *Acc. Chem. Res.* **1999,** *32* (2), 173-182.

67. Kim, D. Y.; Grey, J. K.; Barbara, P. F., A detailed single molecule spectroscopy study of the vibronic states and energy transfer pathways of the conjugated polymer MEH-PPV. *Synth. Met.* **2006,** *156* (2-4), 336-345.

68. (a) da Silva, M. A. T.; Dias, I. F. L.; Duarte, J. L.; Laureto, E.; Silvestre, I.; Cury, L. A.; Guimaraes, P. S. S., Identification of the optically active vibrational modes in the photoluminescence of MEH-PPV films. *Journal of Chemical Physics* **2008,** *128* (9), 094902/1-094902/7; (b) Cury, L. A.; Guimaraes, P. S. S., Dependence of the vibronic emission on self-absorption and reemission processes in conjugated polymers. *Journal of Applied Physics* **2006,** *100* (9), 093105/1-093105/5.

69. Tutt, L.; Tannor, D.; Heller, E. J.; Zink, J. I., The MIME effect: absence of normal modes corresponding to vibronic spacings. *Inorganic Chemistry* **1982,** *21* (10), 3858-9.

70. (a) Tutt, L.; Zink, J. I., Calculation of the electronic spectra and excited-state distortions of W(CO)5(N-donor) from preresonance Raman intensities. *Journal of the American Chemical Society* **1986,** *108* (19), 5830-6; (b) Preston, D. M.; Guentner, W.; Lechner, A.; Gliemann, G.; Zink, J. I., Unusual spectroscopic features in the emission and absorption spectra of single-crystal potassium tetrachloroplatinate(II) (K2[PtCl4]) caused by multiple-mode excited-state distortions. *Journal of the American Chemical Society* **1988,** *110* (17), 5628-33; (c) Preston, D. M.; Shin, K. S.; Hollingsworth, G.; Zink, J. I., Excited state distortions and their spectroscopic consequences in transition metal compounds. *Journal of Molecular Structure* **1988,** *173*, 185-200.

71. (a) Zhao, Z.; Spano, F. C., Multiple Mode Exciton-Phonon Coupling: Applications to Photoluminescence in Oligothiophene Thin Films. *Journal of Physical Chemistry C* **2007,** *111* (16), 6113-6123; (b) Hayes, S. C.; Silva, C., Analysis of the excited-state absorption spectral bandshape of oligofluorenes. *Journal of Chemical Physics* **2010,** *132* (21), 214510/1-214510/10.

72. Tannor, D. J.; Heller, E. J., Polyatomic Raman scattering for general harmonic potentials. *Journal of Chemical Physics* **1982,** *77* (1), 202-18.

73. The solvent polarity index refers to an relative measure of the degree of interaction between the solvent and a specific polar molecule solute.

74. Heller, E. J.; Sundberg, R.; Tannor, D., Simple aspects of Raman scattering. *J. Phys. Chem.* **1982,** *86* (10), 1822-33.

75. Huser, T.; Yan, M.; Rothberg, L. J., Single chain spectroscopy of conformational dependence of conjugated polymer photophysics. *Proceedings of the National Academy of Sciences of the United States of America* **2000,** *97* (21), 11187-11191.

76. Yu, J.; Hu, D.; Barbara, P. F., Unmasking electronic energy transfer of conjugated polymers by suppression of O2 quenching. *Science (Washington, D. C.)* **2000,** *289* (5483), 1327-1330.

77. (a) Collison, C. J.; Treemaneekarn, V.; Oldham, W. J.; Hsu, J. H.; Rothberg, L. J., Aggregation effects on the structure and optical properties of model PPV oligomer. *Synth. Met.* **2001,** *119* (1-3), 515-518; (b) Jakubiak, R.; Rothberg, L. J.; Wan, W.; Hsieh, B. R., Reduction of photoluminescence quantum yield by interchain interactions in conjugated polymer films. *Synth. Met.* **1999,** *101* (1-3), 230-233; (c) Wang, P.; Collison, C. J.; Rothberg, L. J., Origins of aggregation quenching in luminescent phenylenevinylene polymers. *Journal of Photochemistry and Photobiology, A: Chemistry* **2001,** *144* (1), 63-68.

78. (a) Kawano, K.; Pacios, R.; Poplavskyy, D.; Nelson, J.; Bradley, D. D. C.; Durrant, J. R., Degradation of organic solar cells due to air exposure. *Sol. Energy Mater. Sol. Cells* **2006,** *90* (20), 3520-3530; (b) Pacios, R.; Chatten, A. J.; Kawano, K.; Durrant, J. R.; Bradley, D. D. C.; Nelson, J., Effects of photo-oxidation on the performance of poly[2-methoxy-5-(3',7'-dimethyloctyloxy)-1,4-phenylene vinylene]:[6,6]-phenyl C61-butyric acid methyl ester solar cells. *Adv. Funct. Mater.* **2006,** *16* (16), 2117-2126.

79. Hoppe, H.; Glatzel, T.; Niggemann, M.; Schwinger, W.; Schaeffler, F.; Hinsch, A.; Lux-Steiner, M. C.; Sariciftci, N. S., Efficiency limiting morphological factors of MDMO-PPV:PCBM plastic solar cells. *Thin Solid Films* **2006,** *511-512*, 587-592.

80. Cates, N. C.; Gysel, R.; Dahl, J. E. P.; Sellinger, A.; McGehee, M. D., Effects of Intercalation on the Hole Mobility of Amorphous Semiconducting Polymer Blends. *Chemistry of Materials* **2010,** *22* (11), 3543-3548.

81. (a) Sims, M.; Tuladhar, S. M.; Nelson, J.; Maher, R. C.; Campoy-Quiles, M.; Choulis, S. A.; Mairy, M.; Bradley, D. D. C.; Etchegoin, P. G.; Tregidgo, C.; Suhling, K.; Richards, D. R.; Massiot, P.; Nielsen, C. B.; Steinke, J. H. G., Correlation between microstructure and charge transport in poly(2,5-dimethoxy-p-phenylenevinylene) thin films. *Physical Review B: Condensed Matter and Materials Physics* **2007,** *76* (19), 195206/1-195206/12; (b) Gao, Y.; Martin, T. P.; Niles, E. T.; Wise, A. J.; Thomas, A. K.; Grey, J. K., Understanding Morphology-Dependent

Polymer Aggregation Properties and Photocurrent Generation in Polythiophene/Fullerene Solar Cells of Variable Compositions. *Journal of Physical Chemistry C* **2010,** *114*, 15121-15128.

82. (a) Mayer, A. C.; Toney, M. F.; Scully, S. R.; Rivnay, J.; Brabec, C. J.; Scharber, M.; Koppe, M.; Heeney, M.; McCulloch, I.; McGehee, M. D., Bimolecular crystals of fullerenes in conjugated polymers and the implications of molecular mixing for solar cells. *Adv. Funct. Mater.* **2009,** *19* (8), 1173-1179; (b) Cates, N. C.; Gysel, R.; Beiley, Z.; Miller, C. E.; Toney, M. F.; Heeney, M.; McCulloch, I.; McGehee, M. D., Tuning the Properties of Polymer Bulk Heterojunction Solar Cells by Adjusting Fullerene Size to Control Intercalation. *Nano Letters* **2009,** *9* (12), 4153-4157.

83. (a) Tremblay, N. J.; Gorodetsky, A. A.; Cox, M. P.; Schiros, T.; Kim, B.; Steiner, R.; Bullard, Z.; Sattler, A.; So, W.-Y.; Itoh, Y.; Toney, M. F.; Ogasawara, H.; Ramirez, A. P.; Kymissis, I.; Steigerwald, M. L.; Nuckolls, C., Photovoltaic Universal Joints: Ball-and-Socket Interfaces in Molecular Photovoltaic Cells. *ChemPhysChem 11* (4), 799-803; (b) Szarko, J. M.; Guo, J.-C.; Liang, Y.-Y.; Lee, B.-D.; Rolczynski, B. S.; Strzalka, J.; Xu, T.; Loser, S.; Marks, T. J.; Yu, L.-P.; Chen, L.-X., When Function Follows Form: Effects of Donor Copolymer Side Chains on Film Morphology and BHJ Solar Cell Performance. *Advanced Materials (Weinheim, Germany) 22* (48), 5468-5472; (c) Collins, B. A.; Gann, E.; Guignard, L.; He, X.; McNeill, C. R.; Ade, H., Molecular Miscibility of Polymer-Fullerene Blends. *Journal of Physical Chemistry Letters 1* (21), 3160-3166.

84. (a) Melzer, C.; Koop, E. J.; Mihailetchi, V. D.; Blom, P. W. M., Hole transport in poly(phenylenevinylene)/methanofullerene bulk-heterojunction solar cells. *Adv. Funct. Mater.* **2004,** *14* (9), 865-870; (b) Tuladhar, S. M.; Poplavskyy, D.; Choulis, S. A.; Durrant, J. R.; Bradley, D. D. C.; Nelson, J., Ambipolar charge transport in films of methanofullerene and poly(phenylenevinylene)/methanofullerene blends. *Advanced Functional Materials* **2005,** *15* (7), 1171-1182.

85. Myers, A. B., Resonance Raman intensities: the roundabout way to Franck-Condon analysis. *Advances in Multi-Photon Processes and Spectroscopy* **1998,** *11*, 3-50.

86. (a) Heimel, G.; Somitsch, D.; Knoll, P.; Bredas, J.-L.; Zojer, E., Effective conjugation and Raman intensities in oligo(para-phenylene) s: a microscopic view from first-principles calculations. *J. Chem. Phys.* **2005,** *122* (11), 114511/1-114511/9; (b) Furukawa, Y.; Sakamoto, A.; Ohta, H.; Tasumi, M., Raman characterization of polarons, bipolarons and solitons in conducting polymers. *Synth. Met. FIELD Full Journal Title:Synthetic Metals* **1992,** *49* (1-3), 335-40; (c) Furukawa, Y., Electronic Absorption and Vibrational Spectroscopies of Conjugated Conducting Polymers. *Journal of Physical Chemistry* **1996,** *100* (39), 15644-15653.

87. Tuladhar, S. M.; Sims, M.; Kirkpatrick, J.; Maher, R. C.; Chatten, A. J.; Bradley, D. D. C.; Nelson, J.; Etchegoin, P. G.; Nielsen, C. B.; Massiot, P.; George, W. N.; Steinke, J. H. G., Influence of alkyl chain length on charge transport in symmetrically substituted poly(2,5-dialkoxy-p-phenylenevinylene) polymers. *Physical Review B: Condensed Matter and Materials Physics* **2009,** *79* (3), 035201/1-035201/10.

88. Bruevich, V. V.; Makhmutov, T. S.; Elizarov, S. G.; Nechvolodova, E. M.; Paraschuk, D. Y., Raman spectroscopy of intermolecular charge transfer complex between a conjugated polymer and an organic acceptor molecule. *J. Chem. Phys.* **2007,** *127* (10), 104905/1-104905/9.

89. (a) Yan, M.; Rothberg, L. J.; Kwock, E. W.; Miller, T. M., Interchain excitations in conjugated polymers. *Phys Rev Lett* **1995,** *75* (10), 1992-5; (b) Nguyen, T.-Q.; Doan, V.; Schwartz, B. J., Conjugated polymer aggregates in solution: Control of interchain interactions. *J. Chem. Phys.* **1999,** *110* (8), 4068-4078; (c) Nguyen, T.-Q.; Martini, I. B.; Liu, J.; Schwartz, B. J., Controlling Interchain Interactions in Conjugated Polymers: The Effects of Chain Morphology on Exciton-Exciton Annihilation and Aggregation in MEH-PPV Films. *J. Phys. Chem. B* **2000,** *104* (2), 237-255; (d) Collison, C. J.; Rothberg, L. J.; Treemaneekarn, V.; Li, Y., Conformational Effects on the Photophysics of Conjugated Polymers: A Two Species Model for MEH-PPV Spectroscopy and Dynamics. *Macromolecules* **2001,** *34* (7), 2346-2352.

90. (a) Kemerink, M.; van Duren, J. K. J.; Jonkheijm, P.; Pasveer, W. F.; Koenraad, P. M.; Janssen, R. A. J.; Salemink, H. W. M.; Wolter, J. H., Relating Substitution to Single-Chain Conformation and Aggregation in Poly(p-phenylene Vinylene) Films. *Nano Letters* **2003,** *3* (9), 1191-1196; (b) Kemerink, M.; van Duren, J. K. J.; van Breemen, A. J. J. M.; Wildeman, J.; Wienk, M. M.; Blom, P. W. M.; Schoo, H. F. M.; Janssen, R. A. J., Substitution and Preparation Effects on the Molecular-Scale Morphology of PPV Films. *Macromolecules* **2005,** *38* (18), 7784-7792.

91. Bittner, E. R.; Karabunarliev, S.; Herz, L. M., Theory of non-Condon emission from the interchain exciton in conjugated polymer aggregates. *J. Chem. Phys. FIELD Full Journal Title:Journal of Chemical Physics* **2007,** *126* (19), 191102/1-191102/4.

92. Yang, G.; Li, Y.; White, J. O.; Drickamer, H. G., Effect of Pressure on the Fluorescence of Poly[2-methoxy-5-(2'-ethylhexoxy)-p-Phenylenevinylene]. *J. Phys. Chem. B* **1999,** *103* (25), 5181-5186.

93. Tutt, L.; Tannor, D.; Schindler, J.; Heller, E. J.; Zink, J. I., Calculation of the missing mode effect frequencies from Raman intensities. *Journal of Physical Chemistry* **1983,** *87* (16), 3017-19.

94. (a) Guha, S.; Graupner, W.; Resel, R.; Chandrasekhar, M.; Chandrasekhar, H. R.; Glaser, R.; Leising, G., High pressure studies on the planarity of para-hexaphenyl. *Synthetic Metals* **1999,** *101* (1-3), 180-181; (b) Guha, S.; Graupner, W.; Resel, R.; Chandrasekhar, M.; Chandrasekhar, H. R.; Glaser, R.; Leising, G., Tuning Intermolecular Interactions: A Study of the Structural and Vibrational Properties of p-Hexaphenyl under Pressure. *J. Phys. Chem. A* **2001,** *105* (25), 6203-6211.

95. (a) Tikhoplav, R. K.; Hess, B. C., Effect of pressure on photoluminescence and optical absorption in MEH-PPV. *Synthetic Metals* **1999,** *101* (1-3), 236-237; (b) Zeng, Q. G.; Ding, Z. J.; Ju, X.; Zhang, Z. M., The influence of PPV chain aggregated structure on optical properties. *European Polymer Journal* **2005,** *41* (4), 743-746; (c) Paudel, K.; Chandrasekhar, M.; Guha, S.,

Tuning intermolecular interactions in di-octyl substituted polyfluorene via hydrostatic pressure. *arXiv.org, e-Print Archive, Condensed Matter* **2009**, 1-22, arXiv:0905 1736v1 [cond-mat soft].

96. (a) Jakubiak, R.; Collison, C. J.; Wan, W. C.; Rothberg, L. J.; Hsieh, B. R., Aggregation Quenching of Luminescence in Electroluminescent Conjugated Polymers. *J. Phys. Chem. A* **1999,** *103* (14), 2394-2398; (b) Chen, S. H.; Su, A. C.; Han, S. R.; Chen, S. A.; Lee, Y. Z., Molecular Aggregation and Luminescence Properties of Bulk Poly(2,5-di-n-octyloxy-1,4-phenylenevinylene). *Macromolecules* **2004,** *37* (1), 181-186.

97. Gelinck, G. H.; Warman, J. M., The effect of photo-oxidation on the photo-conductivity of isolated polyphenylenevinylene chains. *Chem. Phys. Lett.* **1997,** *277* (4), 361-366.

98. Deibel, C.; Strobel, T.; Dyakonov, V., Role of the Charge Transfer State in Organic Donor–Acceptor Solar Cells. *Advanced Materials* **2010,** *22* (37), 4097-4111.

99. Vandewal, K.; Tvingstedt, K.; Gadisa, A.; Inganas, O.; Manca, J. V., On the origin of the open-circuit voltage of polymer-fullerene solar cells. *Nat Mater* **2009,** *8* (11), 904-909.

100. (a) Barbara, P. F.; Meyer, T. J.; Ratner, M. A., Contemporary Issues in Electron Transfer Research. *J. Phys. Chem.* **1996,** *100* (31), 13148-13168; (b) Hutchison, G. R.; Ratner, M. A.; Marks, T. J., Intermolecular Charge Transfer between Heterocyclic Oligomers. Effects of Heteroatom and Molecular Packing on Hopping Transport in Organic Semiconductors. *J. Am. Chem. Soc. FIELD Full Journal Title:Journal of the American Chemical Society* **2005,** *127* (48), 16866-16881.

101. Benson-Smith, J. J.; Goris, L.; Vandewal, K.; Haenen, K.; Manca, J. V.; Vanderzande, D.; Bradley, D. D. C.; Nelson, J., Formation of a Ground-State Charge-Transfer Complex in Polyfluorene//[6,6]-Phenyl-C61 Butyric Acid Methyl Ester (PCBM) Blend Films and Its Role in the Function of Polymer/PCBM Solar Cells. *Advanced Functional Materials* **2007,** *17* (3), 451-457.

102. Tvingstedt, K.; Vandewal, K.; Gadisa, A.; Zhang, F.; Manca, J.; Inganäs, O., Electroluminescence from Charge Transfer States in Polymer Solar Cells. *Journal of the American Chemical Society* **2009,** *131* (33), 11819-11824.

103. Drori, T.; Sheng, C. X.; Ndobe, A.; Singh, S.; Holt, J.; Vardeny, Z. V., Below-gap excitation of pi-conjugated polymer-fullerene blends: implications for bulk organic heterojunction solar cells. *Physical Review Letters* **2008,** *101* (3), 037401/1-037401/4.

104. Myers, A. B., Resonance Raman Intensities and Charge-Transfer Reorganization Energies. *Chemical Reviews (Washington, D. C.)* **1996,** *96* (3), 911-26.

105. (a) Bruevich, V. V.; Makhmutov, T. S.; Elizarov, S. G.; Nechvolodova, E. M.; Paraschuk, D. Y., Raman spectroscopy of intermolecular charge transfer complex between a conjugated polymer and an organic acceptor molecule. *Journal of Chemical Physics* **2007,** *127* (10), 104905/1-104905/9; (b) Parashchuk, O. D.; Bruevich, V. V.; Paraschuk, D. Y., Association function of conjugated polymer charge-transfer complex. *Phys. Chem. Chem. Phys.* **2010,** *12* (23), 6021-6026.

106. (a) Wise, A. J.; Precit, M. R.; Papp, A. M.; Grey, J. K., Effect of Fullerene Intercalation on the Conformation and Packing of Poly(2-methoxy-5-(3'-7'-dimethyloctyloxy)-1,4-phenylenevinylene). *ACS Applied Materials & Interfaces 3* (8), 3011-3019; (b) Bakulin, A. A.; Martyanov, D. S.; Paraschuk, D. Y.; Pshenichnikov, M. S.; van Loosdrecht, P. H. M., Ultrafast Charge Photogeneration Dynamics in Ground-State Charge-Transfer Complexes Based on Conjugated Polymers. *J. Phys. Chem. B* **2008,** *112* (44), 13730-13737.

107. McGlynn, S. P., Molecular Complexes. *Annu. Rev. Phys. Chem.*

108. (a) Bakulin, A. A.; Martyanov, D.; Paraschuk, D. Y.; van Loosdrecht, P. H. M.; Pshenichnikov, M. S., Charge-transfer complexes of conjugated polymers as intermediates in charge photogeneration for organic photovoltaics. *Chem. Phys. Lett.* **2009,** *482* (1-3), 99-104; (b) Drori, T.; Holt, J.; Vardeny, Z. V., Optical studies of the charge transfer complex in

polythiophene/fullerene blends for organic photovoltaic applications. *Physical Review B: Condensed Matter and Materials Physics 82* (7), 075207/1-075207/8.